



**DEVELOPMENT OF HIGH-PERFORMANCE
MULTIDIMENSIONAL BISMUTH TELLURIDE-
BASED THERMOELECTRIC MATERIALS**

A Thesis submitted by

Yuan Wang, B. Eng. (Hons)

For the award of

Doctor of Philosophy

2020

Abstract

Thermoelectric materials enable the direct conversion between heat and electricity through the Seebeck effect. The efficiency of energy conversion is governed by a dimensionless figure of merit (zT) as: $zT = S_2\sigma T/\kappa$, where S , σ , κ , and T is the Seebeck coefficient, electrical conductivity, thermal conductivity, and operating temperature, respectively. By fabricating thermoelectric materials into pellets or thin films, they can be facilely integrated with wearable electronics to harvest human body heat at the low temperature, acting as the energy-autonomous, maintenance-free and emission-free power sources. To this end, developing high-performance multi-dimensional low-temperature thermoelectric materials is of vital significance.

So far, the best low-temperature (200-400 K) thermoelectric materials are bismuth telluride (Bi_2Te_3) and its compounds, where promising zT can be achieved from enhanced power factor ($S_2\sigma$) and suppressed lattice thermal conductivity (κ_l). With the combination of several strategies including point defect, texture and nanostructure engineering, zT of Bi_2Te_3 -based thermoelectric pellet has been improved up to 1.5. On the other hand, studies on Bi_2Te_3 -based thermoelectric thin films mainly focus on the optimizations of inorganic film crystallinity and defects, and interface engineering in inorganic/organic hybrids, showing record zT up to 0.89. In order to further boost zT of Bi_2Te_3 -based thermoelectric pellets and thin films, there are at least four issues deserving to be further explored. (1) Carrier concentration (n) of Bi_2Te_3 pellets still deviates from the predicted optimal value, leading relatively low $S_2\sigma$. (2) Further κ reduction of Bi_2Te_3 pellets is desired, considering current studies have pushed κ close to predicted amorphous limit. (3) Interfacial carrier transports between Bi_2Te_3 -based inorganic fillers and conductive polymers are impeded by high interfacial contact resistances, leading poor σ in Bi_2Te_3 -based inorganic/organic thermoelectric films. (4) Low crystallinity of conductive polymers and poor interfacial carrier transports lead poor carrier mobility (μ) in Bi_2Te_3 -based inorganic/organic thermoelectric films. Given aforementioned four issues, corresponding studies have been conducted in this PhD project, which are summarized in the following.

- i. Nanostructured n -type Bi_2Te_3 pellet was fabricated through solvothermal synthesis followed by spark plasma sintering (SPS), where n was modulated by non-equilibrium fast reaction to approach the optimal value calculated by single parabolic band (SPB) model. Te vacancies were found to be effectively suppressed, leading reduced n from pristinely $\sim 1 \times 10^{20}$ to $\sim 6 \times 10^{19}$ cm^{-3} and generating a decent $S_2\sigma$ of $12.84 \mu\text{W cm}^{-1} \text{K}$.

- 2 at 320 K. Meanwhile, the decreased electronic thermal conductivity (κ_e) due to deteriorated σ enabled a very low κ of $0.48 \text{ W m}^{-1} \text{ K}^{-1}$, which ultimately secured a promising zT of ~ 1.1 at 420 K and an outstanding average zT of ~ 1 from 320 to 470 K. (*Chemical Engineering Journal*, 2019, 391: 123513)
- ii. Nanostructured *n*-type Bi_2Te_3 pellet with porous structure was fabricated using solvothermal synthesis and SPS technique. Homogeneously distributed pores and dense grain boundaries were successfully introduced into the Bi_2Te_3 matrix, causing strong phonon scatterings. As a result, an ultralow κ_l of $< 0.1 \text{ W m}^{-1} \text{ K}^{-1}$ was achieved. With the well-maintained decent $S_2\sigma$ of $10.57 \mu\text{W cm}^{-1} \text{ K}^{-2}$, a promising zT value of 0.97 was secured at 420 K. (*ACS Applied Materials & Interfaces*, 2019, 11: 31237-31244)
- iii. Interfacial carrier transports in $\text{Bi}_{0.5}\text{Sb}_{1.5}\text{Te}_3/\text{PEDOT:PSS}$ flexible thermoelectric films were optimized by coating $\text{Bi}_{0.5}\text{Sb}_{1.5}\text{Te}_3$ fillers with highly conductive CuTe layer, using facile electroless plating method. Highly conductive CuTe layer can render carriers to travel within CuTe layers or through $\text{Bi}_{0.5}\text{Sb}_{1.5}\text{Te}_3$ fillers, rather than being scattered. Consequently, interfacial contact resistances were significantly reduced. Meanwhile, highly crystallized conductive polymer PEDOT:PSS with microstructure of lamella stacking was prepared by DMSO- H_2SO_4 double treatments, where insulating PSS was effectively depleted. Optimized interfacial carrier transports and highly crystallized PEDOT:PSS synergistically contributed to significant boost of μ from pristinely ~ 0.77 to $\sim 18.82 \text{ cm}^2 \text{ V}^{-1} \text{ s}^{-1}$, resulting in outstanding σ of $\sim 2300 \text{ S cm}^{-1}$ and record-high room-temperature $S_2\sigma$ of $312 \mu\text{W m}^{-1} \text{ K}^{-2}$ in $\text{Bi}_{0.5}\text{Sb}_{1.5}\text{Te}_3/\text{PEDOT:PSS}$ flexible thermoelectric films. Accordingly, a home-made flexible thermoelectric device was fabricated using as-prepared composites, generating a promising open-circuit thermovoltage of $\sim 7.7 \text{ mV}$ with the human wrist as the thermal source. (*Chemical Engineering Journal*, 2020, 397: 125360)

Certification of Thesis

This Thesis is the work of Yuan Wang except where otherwise acknowledged, with the majority of the authorship of the papers presented as a Thesis by Publication undertaken by the Student. The work is original and has not previously been submitted for any other award, except where acknowledged.

Principal Supervisor: **Professor Zhi-Gang Chen**

Associate Supervisor: **Professor Hao Wang**

Associate Supervisor: **Professor Jin Zou**

Student and supervisors signatures of endorsement are held at the University.

Statement of Contribution

The following details are the agreed share of contribution for candidate and co-authors in the presented publications in this thesis.

1. **Wang, Y.**; Yang, L.; Shi, X.-L.; Shi, X.; Chen, L.; Dargusch, M. S.; Zou, J.; Chen, Z.-G. Flexible Thermoelectric Materials and Generators: Challenges and Innovations. *Adv. Mater.* **2019**, *31*, 1807916. (2020 IF=27.40)

Contributor	Statement of contribution
Yuan Wang (Candidate)	Wrote and edited paper (50%) Carried out reference summary (70%)
Lei Yang	Wrote and edited paper (20%)
Xiaolei Shi	Carried out reference summary (15%)
Xun Shi	Carried out reference summary (5%)
Lidong Chen	Wrote and edited paper (5%)
Matthew Dargusch	Wrote and edited paper (5%)
Jin Zou	Supervised the project (40%) Wrote and edited paper (10%)
Zhi-Gang Chen	Supervised the project (60%) Wrote and edited paper (10%) Carried out reference summary (10%)

2. **Wang, Y.**; Liu, W.-D.; Shi, X.-L.; Hong, M.; Wang, L.-J.; Li, M.; Wang, H.; Zou, J.; Chen, Z.-G. Enhanced Thermoelectric Properties of Nanostructured *n*-Type Bi₂Te₃ by Suppressing Te Vacancy through Non-Equilibrium Fast Reaction. *Chem. Eng. J.* **2019**, *391*, 123513. (2020 IF=10.65)

Contributor	Statement of contribution
Yuan Wang (Candidate)	Carried out sample synthesis (75 %) Designed experiments (80 %) Wrote and edited paper (60 %) Carried out characterization (60 %) Carried out data analysis (65 %)
Weidi Liu	Wrote and edited paper (10 %) Carried out characterization (20 %) Carried out data analysis (10 %)
Han Gao	Carried out characterization (20 %)
Lijun Wang	Carried out sample synthesis (10%)
Meng Li	Carried out data analysis (10%)
Xiaolei Shi	Carried out sample synthesis (5%)
Min Hong	Carried out data analysis (5 %)
Hao Wang	Supervised the project (10 %)
Jin Zou	Supervised the project (30 %) Wrote and edited paper (10 %)
Zhi-Gang Chen	Wrote and edited paper (20 %) Supervised the project (40 %) Carried out data analysis (10 %) Designed experiments (20%)

3. **Wang, Y.**; Liu, W. D.; Gao, H.; Wang, L. J.; Li, M.; Shi, X. L.; Hong, M.; Wang, H.; Zou, J.; Chen, Z.-G. High Porosity in Nanostructured *n*-Type Bi₂Te₃ Obtaining Ultralow Lattice Thermal Conductivity. *ACS Appl. Mater. Interfaces* **2019**, *11*, 31237-31244. (2020 IF=8.76)

Contributor	Statement of contribution
Yuan Wang (Candidate)	Carried out sample synthesis (90 %) Designed experiments (80 %) Wrote and edited paper (60 %) Carried out characterization (70 %) Carried out data analysis (75 %)
Weidi Liu	Carried out characterization (20 %) Wrote and edited paper (20%) Carried out data analysis (10%)
Xiaolei Shi	Carried out data analysis (10 %)
Min Hong	Carried out characterization (10%)
Lijun Wang	Carried out sample synthesis (10%)
Meng Li	Carried out data analysis (5 %)
Hao Wang	Supervised the project (10 %)
Jin Zou	Supervised the project (30 %) Wrote and edited paper (10 %)
Zhi-Gang Chen	Supervised the project (60 %) Wrote and edited paper (10 %) Designed experiments (20 %) Carried out data analysis (5%)

4. **Wang, Y.**; Hong, M.; Liu, W. D.; Shi, X.-L.; Xu, S.-D.; Sun, Q.; Gao H.; Zou, J.; Chen, Z.-G. Bi_{0.5}Sb_{1.5}Te₃/PEDOT:PSS-Based Flexible Thermoelectric Film and Device. *Chem. Eng. J.* **2020**, 397, 125360. (2020 IF=10.65)

Contributor	Statement of contribution
Yuan Wang (Candidate)	Carried out sample synthesis (90 %) Designed experiments (80 %) Wrote and edited paper (60 %) Carried out characterization (70 %) Carried out data analysis (75 %)
Weidi Liu	Carried out characterization (20 %) Wrote and edited paper (20%) Carried out data analysis (10%)
Xiaolei Shi	Carried out data analysis (10 %)
Min Hong	Carried out characterization (10%)
Lijun Wang	Carried out sample synthesis (10%)
Meng Li	Carried out data analysis (5 %)
Hao Wang	Supervised the project (10 %)
Jin Zou	Supervised the project (30 %) Wrote and edited paper (10 %)
Zhi-Gang Chen	Supervised the project (60 %) Wrote and edited paper (10 %) Designed experiments (20 %) Carried out data analysis (5%)

Acknowledgement

I would like to acknowledge University of Southern Queensland International Fees Research Scholarship and Australian Research Council PhD Scholarship for their financial supports during my candidature.

Looking back my three-year PhD period, I would like to firstly appreciate my supervisors Professor Zhi-Gang Chen, Professor Jin Zou and Professor Hao Wang for their tremendous and selfless supports and mentoring. They have solid professional knowledge and strong execution abilities, from which I gradually learnt to be an independent researcher. Their serious and strict attitudes reshaped my impressions to be a researcher and developed me with critical thinking and strong problem-solving abilities, which I believe will benefit me a lot throughout my life. I am proud to be their students and have the opportunity to contribute to thermoelectric community. I wish all the best to my supervisors and their research careers.

I would also like to acknowledge my colleagues in The University of Queensland and University of Southern Queensland, including Dr. Lei Yang, Dr. Min Hong, Dr. Xiaolei Shi, Dr. Weidi Liu, Dr. Han Gao, Dr. Raza Moshwan, Dr. Lijun Wang, Dr. Liqing Huang, Mr. Youichirou Kawami, Mr. Meng Li, Mr. Qiang Sun, Mr. Shengduo Xu, Miss Wanyu Lv, Miss Yuzhe Yang, Miss Xiaomei Yao, Mr. Van Nguyen, Mr. Qizhen Li, Mr. Junjie Li, Mr. Ting Liu and Mr. Zijie Lin, for their discussions and assistances. You guys make my life easier and the time we debate was always an enjoyment.

Above all, I would like to express my deep appreciations to my father and mother. Life goes up and down, you are always the backbones I can rely on. I am proud to be your son and will continue fighting to be your pride. Lastly, I would send my special gratefulness to my girlfriend Miss Mengyuan Kong (hopefully Dr. Mengyuan Kong within 2 years). You walked into my life in my darkest time and warm me up with your love, tolerance and devotions without saying a word. I know you are the one I can embrace whenever I am lost and I hope so am I.

Table of Contents

Abstract.....	II
Certification of Thesis.....	IV
Statement of Contribution	V
Acknowledgement	IX
List of Figures.....	XII
List of Abbreviations	XIV
Chapter 1 Introduction.....	1
1.1 Background	1
1.2 Aims and Objectives	1
1.3 Thesis Outline	2
Chapter 2: Literature Review	4
2.1 Mechanisms of thermoelectric energy conversions and devices	4
2.1.1 Thermoelectric effects	4
2.1.2 Figure of merit zT	5
2.1.3 Thermoelectric power generation and refrigeration.....	6
2.2 Chief characteristics of Bi ₂ Te ₃ -based thermoelectric materials.....	7
2.2.1 Crystal and electronic band structures	7
2.2.2 Strong anisotropy	9
2.2.3 Intrinsic point defects	10
2.3 Progresses and optimization strategies of Bi ₂ Te ₃ -based thermoelectric pellets	11
2.3.1 Point defect engineering.....	11
2.3.2 Texture engineering.....	13
2.3.3 Phonon scattering strengthening	15
2.4 Progresses and optimization strategies of Bi ₂ Te ₃ family thermoelectric films.....	16
2.4.1 Energy-filtering effect	17
2.4.2 Filler surface modification	18
2.4.3 Carbon-nanotube scaffolds.....	19
2.4.4 Physical vapour deposition.....	21
2.4.5 Other potential strategies.....	22
2.5 Challenges and opportunities	23

Chapter 3: Methodologies	24
3.1 Synthesis methods of Bi ₂ Te ₃ family powders	24
3.1.1 Solvo-thermal synthesis	24
3.1.2 Solid-solution synthesis.....	25
3.1.3 Electroless plating synthesis.....	26
3.2 Fabrication methods of Bi ₂ Te ₃ family films	26
3.2.1 Plasma treatment towards glass substrates.....	26
3.2.2 Spin coating.....	27
3.3 Characterization methods.....	28
3.3.1 X-Ray Diffraction (XRD)	28
3.3.2 Scanning Electron Microscopy (SEM)	29
3.4 Properties measurements	31
3.4.1 Electrical properties.....	31
3.4.2 Thermal Properties	33
Chapter 4 Enhanced Thermoelectric Properties of Nanostructured <i>n</i>-Type Bi₂Te₃ by Suppressing Te Vacancy through Non-equilibrium Fast Reaction.....	36
4.1 Overview.....	36
4.2 Journal publication.....	37
Chapter 5 High Porosity in Nanostructured <i>n</i>-Type Bi₂Te₃ Obtaining Ultralow Lattice Thermal Conductivity	56
5.1 Overview.....	56
5.2 Journal publication.....	57
Chapter 6 Outstanding Bi_{0.5}Sb_{1.5}Te₃/PEDOT:PSS Flexible Thermoelectric Film and Device <i>via</i> Boosted Interfacial Carrier Transport	76
6.1 Overview.....	76
6.2 Submitted publication	77
Chapter 7: Conclusions and Perspectives.....	94
7.1 Conclusions.....	94
7.2 Perspectives.....	95
Reference	97
Appendix:.....	116

List of Figures

Figure 2.1 Schematic demonstrations of (a) Seebeck, (b) Peltier and (c) Thomson effects.

Figure 2.2 (a) Typical structure of the thermoelectric device composing of the substrate, TE legs, connecting electrodes and bonding interfaces. (b) Power generating efficiency (η_p) of thermoelectric devices as a function of average figure of merit (zT), zT_{ave} of materials.

Figure 2.3 (a) Front view, (b) top view and (c) side view of Bi_2Te_3 crystal structure, with the quintuple layer highlighted containing five monatomic layers stacking along c -axis in the sequence of -Te(1)-Bi-Te(2)-Bi-Te(1)-.

Figure 2.4 Typical electronic band structure of Bi_2Te_3 .

Figure 2.5 Isoelectron extrinsic doping of p -type Bi_2Te_3 to manipulate point defects formation, with (a) Sb to form p -type $\text{Bi}_{2-x}\text{Sb}_x\text{Te}_3$ and (b) Se or S to transform into n -type $\text{Bi}_2\text{Te}_{3-x}(\text{Se},\text{S})_x$.

Figure 2.6 Donor-like effect of Bi_2Te_3 to generate extra n_e , induced by (a) balling milling and (b) hot deformations.

Figure 2.7 Texture engineering towards Bi_2Te_3 family with improved zT , where (a) texture of p -type $\text{Bi}_{0.5}\text{Sb}_{1.5}\text{Te}_3$ is weakened (b) after hot forging, texture of n -type $\text{Bi}_2\text{Te}_{2.7}\text{Se}_{0.3}$ is weakened (b) after sample repressing.

Figure 2.8 Significant decreased (a) κ and (b) κ_l of nanostructured Bi_2Te_3 family compared with the ingot counterpart.

Figure 2.9. Schematic illustration of the energy-filtering effect at the interface between the conductive polymer and the filler.

Figure 2.10. Effects of filler surface status in conductive polymer composites. (a) SEM image of cross section of $\text{Bi}_2\text{Te}_3/\text{PEDOT:PSS}$ thin films, where high contact resistivity between Bi_2Te_3 filler and PEDOT:PSS is emphasised by the red solid line. (b) Significant enhancement of the power factor ($S_2\sigma$) after the removal of the oxidation layer on the filler surface through acid rinsing. Reproduced with permission.

Figure 2.11. Fabrication of free-standing FTE thin films by applying carbon-nanotube scaffold. (a) Schematic of the fabrication of a free-standing highly ordered Bi_2Te_3 -SWCNT FTE thin film. (b) A bright-field TEM image of the interface between Bi_2Te_3 nanocrystals and the SWCNT bundle. Inset: corresponding fast Fourier transform (FFT) pattern of the Bi_2Te_3 . (c) Schematic of the generation of nanopores during Bi_2Te_3 nanocrystal growth. (d) Cross-sectional SEM image of free-standing Bi_2Te_3 -SWCNT FTE thin film.

Figure 3.1 Apparatus and oven for solvo-thermal synthesis. (a) Autoclave with its section structure. (b) Laboratory oven used for the hydro- or solvo-thermal synthesis.

Figure 3.2 Quartz tube and furnace for solid-solution synthesis. (a) Quartz tube with pre-weighted precursors inside. (b) Laboratory furnace used for solid solution synthesis. (c) As-ground $\text{Bi}_{0.5}\text{Sb}_{1.5}\text{Te}_3$ powders.

Figure 3.3 Principles and experimental photos of plasma treatment. (a) Laboratory equipment for plasma treatment. (b) Schematics of plasma treatment mechanism. (c) As-prepared PEDOT:PSS films on glass substrates without plasma treatment (d) As-prepared PEDOT:PSS films on glass substrates with plasma treatment.

Figure 3.4 Principles and experimental photos of spin coating. (a) Schematics of spin coating process. (b) Laboratory spin coater. (c) As-prepared PEDOT:PSS films with different spinning parameters.

Figure 3.5 Schematic diagrams of (a) XRD mechanisms, (b) working principles and typical framework.

Figure 3.6 Introduction of SEM including schematics diagrams of (a) working mechanism, (b) typical framework, (c) generations of secondary electrons and (d) backscattered secondary electrons.

Figure 3.7 Schematic illustration of SBA458 working mechanism and photos of laboratory equipment. (a) Schematic of working mechanism in SBA 458. (b) Non-loaded SBA 458 in the laboratory. (c) Loaded SBA 458 in the laboratory.

Figure 3.8 Schematic illustration of LFA 457 working mechanism and photos of laboratory equipment. (a) Schematic of working mechanism in SBA 458. (b) LFA 457 in the laboratory.

Figure 3.9 Sample preparation for the in-plane thermal diffusivity measurement by the laser flash method. (a) The thin sample was first cut into many small pieces and then stacked and bonded using epoxy resin. It was then put into melted wax and solidified. Both sides of the sample were polished using a sand paper. The wax was removed by heating and then washing in ethyl ether. (b) Thermal diffusivity of the prepared sample was measured by a standard laser flash analysis equipment.

List of Abbreviations

- XRD**: X-ray diffraction
XPS: X-ray spectroscopy
SEM: scanning electron microscopy
SE: secondary electrons
BSE: backscattered electrons
TEM: transmission electron microscopy
EPMA: electron probe micro-analyzer
EDS: energy dispersive X-ray spectrometry
SAED: selected area electron diffraction
FTIR: Fourier transform infrared spectroscopy
DOS: density of states
S: Seebeck coefficient
 σ : electrical conductivity
S₂ σ : power factor
zT: Figure of Merit
zT_{avg}: average Figure of Merit
 κ : thermal conductivity
 κ_e : electronic thermal conductivity
 κ_l : lattice thermal conductivity
k_B: Boltzmann constant
h: Planck constant
m^{*}: density of states effective mass
T: absolute temperature
T_c: cold side temperature
T_h: hot side temperature
 η_p : power generating efficiency
 η_c : refrigeration efficiency
Bi'_{Te}: anti-site defects of Bi at Te sites
V_{Te}: Te vacancies
Bi^x_{Bi}: original Bi atoms without the point defects
Te^x_{Te}: original Te atoms without the point defects

$E_{\text{Bi}'_{\text{Te}}}$: formation energy of anti-site defects of Bi at Te sites

T_m : melting point

$n_{\text{Bi}'_{\text{Te}}}$: number of Bi'_{Te} per cm^3 ,

N_{Te} : number of available Te sites per cm^3

n : Hall carrier concentration

μ : Hall carrier mobility

e : electron charge

R : Hall coefficient

L : Lorenz number

ρ : mass density

v_s : sound velocity

SPS: spark plasma sintering

HP: hot pressing

HD: hot deformation

BM: ball milling

MS: melt spinning

ZM: zone melting

PVP: polyvinylpyrrolidone

ΔE_g : energy barrier

MLD: molecular layer deposition

ALD: atomic layer deposition

LFA: laser flash

EG: ethylene glycol

τ : phonon relaxation time

C_s : spectral heat capacity

v_g : phonon group velocity

SPB: single parabolic mod

Chapter 1 Introduction

In this chapter, the background of implantable and wearable electronics, as well as brief introductions of thermoelectric materials are demonstrated, where the advantages of Bi₂Te₃-based thermoelectric materials as the power sources are highlighted. The aims and objectives of this thesis are then presented, followed by the description of the thesis outline.

1.1 Background

Advances in miniaturization and integration of electronics have recently stimulated the dramatic progress in the development of implantable and wearable electronics. In response to the increasing practical needs, the worldwide market value of implantable and wearable electronics has been predicted to grow up to US\$115.8 billion in 2020 and US\$51 billion in 2022, respectively.^{1,2} Conventional batteries have limited applications in wearable and/or implantable electronics due to their requirements for frequent replacement/recharge and extra-maintenance,³ therefore, developing maintenance-free and energy-autonomous power sources could have a profound impact on the expansion of the number of applications for the wearable and/or implantable electronics.⁴ As an emission-free power source, thermoelectric materials can meet the above requirements by stably and directly converting body heat into electricity through the Seebeck effect,^{5,6} and acting as solid-state power sources without any vibration.^{4,7,8} Especially, Bi₂Te₃-based thermoelectric materials have been widely reported to present outstanding thermoelectric performances in the low-temperature range.⁹⁻¹¹ Therefore, developing high-performance Bi₂Te₃-based thermoelectric materials is of vital significance.

Bi₂Te₃-based thermoelectric materials can be fabricated into either pellets or thin films according to the practical applications. Among which, pellets possess the advantages such as decent thermoelectric performances and stability, while thin films are favoured by flexibility, light weights, and conformal contact with curved heat sources in order to maximize heat harvesting. Both dimensions could be appealing for thermoelectric devices considering various working environments, and therefore deserve further studies.

1.2 Aims and Objectives

In this project, we aim to develop high-performance Bi₂Te₃-based thermoelectric materials with multi-dimensions for efficient low-temperature energy harvesting and generation. For Bi₂Te₃-based thermoelectric pellets, texture, nanostructure, and point defect engineering guided by the single parabolic band model will be utilized to synergistically optimize the power factor by modulating the carrier concentration, and suppress the thermal conductivity *via*

inducing intense phonon scatterings. For Bi₂Te₃-based thermoelectric thin films. Interface engineering will be employed to boost the interfacial carrier transports between inorganic Bi₂Te₃-based fillers and conductive polymers. With highly conductive polymers prepared, outstanding power factor is anticipated to be realized in the inorganic/organic hybrid system. The objectives of this project can be summarized as below:

- iv. To fabricate nanostructured Bi₂Te₃ pellet with porous structure through facile solvothermal synthesis, in order to induce strong phonon scatterings at pores and dense grain boundaries, leading effectively reduced lattice thermal conductivity and improved zT .
- v. To fabricate nanostructured Bi₂Te₃ pellet with optimized carrier concentration, approaching the calculated optimal value, by manipulating the intrinsic point defects (i.e. Te vacancies for n-type Bi₂Te₃ pellets). Boosted power factor is expected, which could contribute to high zT .
- vi. To fabricate Bi₂Te₃-based filler/conductive polymer hybrid thermoelectric thin film with optimized interfacial carrier transports, by applying surface engineering to inorganic fillers, which aims to lower the interfacial contact resistance. Meanwhile, to develop highly crystallized conductive polymer with decent electrical conductivity, leading outstanding power factor in the hybrid system.

1.3 Thesis Outline

This thesis is carefully organized following the below outline:

Chapter 1 is the introduction of this project, where research background and objectives are clarified.

Chapter 2 reviews the literatures of Bi₂Te₃-based thermoelectric pellets and thin films, including the fundamentals of thermoelectric effects, research progresses and optimization strategies of Bi₂Te₃-based thermoelectric pellets and thin films, respectively. The literature review aims to establish a comprehensive understanding of Bi₂Te₃-based multi-dimensional thermoelectric materials, which may guide studies of this project.

Chapter 3 summaries the methods and techniques involved in this project, in terms of the sample synthesis, fabrication, characterizations and property measurements. Synthesis mechanisms and working principles are introduced in detail.

Chapter 4 presents the achievement of nanostructured n-type Bi₂Te₃ pellet with porous structure. In this chapter, one published journal paper is included, with the title of “High Porosity in Nanostructured n-Type Bi₂Te₃ Obtaining Ultralow Lattice Thermal Conductivity

(*ACS Applied Materials & Interfaces*, 2019, 11: 31237-31244)”. This study provides the insight of realizing ultralow lattice thermal conductivity by synergistic phonon scatterings of pores and nanostructure in the *n*-type Bi₂Te₃-based thermoelectric materials.

Chapter 5 describes the modulation of carrier concentration in *n*-type nanostructured Bi₂Te₃ pellet by effectively suppressing the Te vacancies. In this chapter, one published journal paper is included, namely “Extraordinary Thermoelectric Properties of Nanostructured *n*-Type Bi₂Te₃ by Suppressing Te Vacancy through Non-equilibrium Fast Reaction (*Chemical Engineering Journal*, 2019: 123513)”. This study provides a new insight into manipulating intrinsic point defects in nanostructured Bi₂Te₃ thermoelectric materials for achieving higher *zT*.

Chapter 6 presents the realization of superhigh-performance Bi_{0.5}Sb_{1.5}Te₃/PEDOT:PSS flexible thermoelectric film *via* boosting interfacial carrier transports, as well as the home-made flexible thermoelectric device. In this chapter, one submitted manuscript is included, namely “Superhigh-Performance Bi_{0.5}Sb_{1.5}Te₃/PEDOT:PSS Flexible Thermoelectric Film and Device *via* Boosted Interfacial Carrier Transports (Submitted, 2020)”. This study addresses the significance of interfacial carrier transport, hinting the bright prospects of Bi₂Te₃-based thermoelectric thin films as the effective power source of wearable electronics.

Chapter 7 provides the thesis conclusion and perspectives of Bi₂Te₃-based thermoelectric pellets and thin films.

Chapter 2: Literature Review

In this chapter, we overview the mechanisms of thermoelectric energy conversions and the principles of thermoelectric devices from the fundamental point of view, followed by the introduction of Bi₂Te₃-based thermoelectric materials, including their crystal structure, thermoelectric parameters, and primary characteristics affecting their thermoelectric performances. Then, research progresses and corresponding optimization strategies of Bi₂Te₃-based thermoelectric pellet and thin films are summarized, respectively. Finally, challenges and opportunities to further improve the thermoelectric performances of Bi₂Te₃-based thermoelectric pellets and thin films are provided.

2.1 Mechanisms of thermoelectric energy conversions and devices

2.1.1 Thermoelectric effects

During more than two hundred years of developments, thermoelectric materials have been known for their direct conversions between thermal energy and electricity, which can be covered by three fundamental thermoelectric effects, namely, Seebeck effect, Peltier effect and Thomson effect. In 1821, German physicist Thomas Johann Seebeck discovered Seebeck effect that when two wires of different metal were twisted together with different temperatures presented at the two ends, a tiny current could be induced within the wire.¹² The discovery of Seebeck effect indicates the ability of thermoelectric materials to generate electric energy from thermal energy, and its mechanism is explained by **Figure 2.1(a)**. When no temperature gradients exist at the two ends of thermoelectric materials, the charge carriers (i.e. electrons for *n*-type and holes for *p*-type thermoelectric materials) move randomly. With the temperature gradients presented, charge carriers tend to be driven to diffuse towards low-temperature end, forming high electric potentials at high-temperature and low-temperature ends of *n*-type and *p*-type thermoelectric materials, respectively. In this way, if one close circuit is provided, as-generated potential differences can drive carriers to form currents, which may power external electronics. Peltier effect is the reverse effect of Seebeck effect, which was firstly discovered by French watchmaker J. Peltier and describes the ability of thermoelectric materials to generate temperature differences at the two ends, with the presence of external currents.¹² The mechanism of Peltier effect is similar to Seebeck effect but reversed, as shown in **Figure 2.1(b)**. Thomson effect can be understood as the combination of Seebeck effect and Peltier effect, which was discovered by W. Thomson in 1855.¹² Its phenomenon is depicted in **Figure 2.1(c)**, showing that reversible Seebeck and Peltier effects (i.e. heating and cooling) can be induced in

one homogenous semiconductor with the simultaneous presences of temperature gradients and external currents.

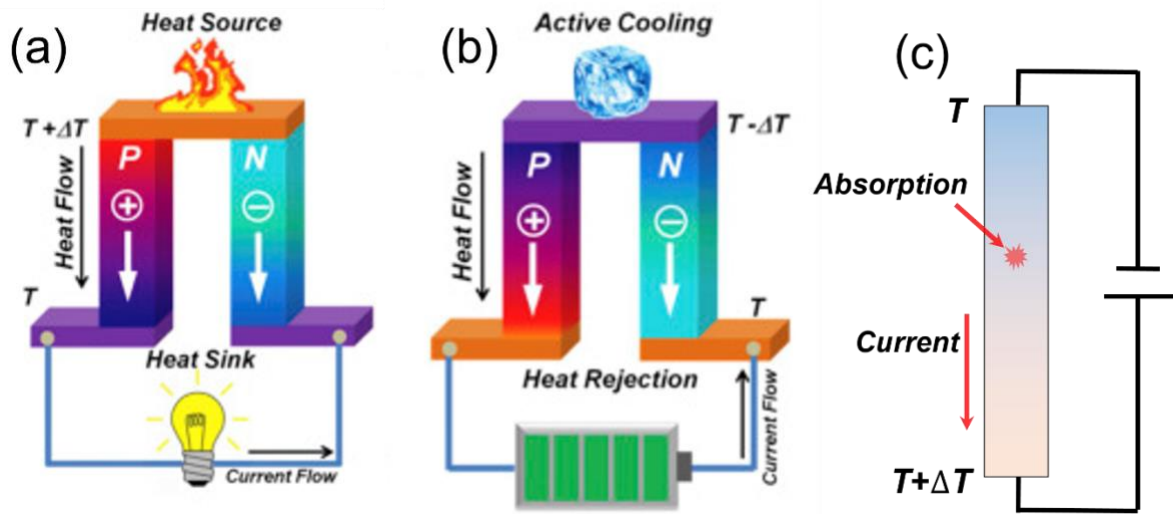


Figure 2.1 Schematic demonstrations of (a) Seebeck,¹³ (b) Peltier¹³ and (c) Thomson effects.

2.1.2 Figure of merit zT

The performance of a given thermoelectric material is governed by the dimensionless figure of merit zT , which is expressed as:^{14,15}

$$zT = \frac{S^2 \sigma T}{\kappa}, \quad (2-1)$$

where S , σ , κ and T are the Seebeck coefficient, electrical conductivity ($\sigma = n\mu e$, where n , μ and e are the carrier concentration, carrier mobility, and electron charge, respectively), total thermal conductivity and absolute temperature, respectively.¹⁶ $S^2\sigma$ is the power factor and κ is principally constituted by the electronic conductivity ($\kappa_e = L\sigma T$, where L is the Lorenz number) and lattice thermal conductivity (κ_l), i.e. $\kappa = \kappa_l + \kappa_e$. S can be illustrated by the Pisarenko relation:⁶

$$S = \frac{8\pi^2 k_B^2}{3eh^2} m^* T \left(\frac{\pi}{3n}\right)^{2/3}, \quad (2-2)$$

where k_B , h and m^* are the Boltzmann constant, the Planck constant, and the density of states (DOS) effective mass, respectively.¹⁷ In order to achieve high zT , materials should possess high σ , high S and low κ . However, these three key parameters are strongly interrelated and are conflicted with each other.¹⁸ As introduced above, increasing n can lead to an increase in σ and κ_e , along with a decrease in S . This could eventually be detrimental to zT . It is still a significant challenge to decouple and optimize these parameters^{5,19,20} in order to secure high zT , making thermoelectric materials competitive in the market.

2.1.3 Thermoelectric power generation and refrigeration

Based on thermoelectric effects, thermoelectric devices can realize the effective power generation and refrigeration.²¹ **Figure 2.2(a)** illustrates the structure of one typical thermoelectric device, composed of the substrate, TE legs, connecting electrodes, and bonding interfaces.²² Among which, substrates are insulating in order to guarantee interference-free carrier transport within the TE legs; The TE legs can be in the form of either pellets or thin films, which can be adapted based on practical usages; electrodes are applied to connect *n*- and *p*-type TE legs in series; and the bonding interfaces stabilize the TE legs and electrodes.²² Moreover, the Seebeck effect²³ is the primary enabling physical phenomenon which facilitates the function of thermoelectric devices as potential body-temperature monitors by transferring body temperature changes into output voltage signal.²⁴ By using the Peltier Effect¹³, thermoelectric devices can also be applied in temperature control systems, which can be used in microclimate system that maintains the body-temperature in extreme conditions,²⁵ medical devices such as cooling blankets,²⁶ and emerging portable electronic devices, which require cooling for portable electronic devices.^{27,28} Although their applications as power implantable devices are still controversial with concerns about their toxicity, there is clearly a bright future therein.

The Seebeck and Peltier effects provide the underlying physics which enables both power generation and refrigeration function of thermoelectric devices, and their efficiency can be expressed as:^{5,29}

$$\eta_p = \frac{T_h - T_c}{T_h} \left[\frac{\sqrt{1 + zT_{ave}} - 1}{\sqrt{1 + zT_{ave} + T_c/T_h}} \right], \text{ and} \quad (2-3)$$

$$\eta_c = \frac{T_c}{T_h - T_c} \left[\frac{\sqrt{1 + zT_{ave}} - T_h/T_c}{\sqrt{1 + zT_{ave} + 1}} \right], \quad (2-4)$$

where η_p , η_c , T_h and T_c are the power generating efficiency, refrigeration efficiency, temperature at the hot and cold ends, respectively; and zT_{ave} is the average dimensionless figure of merit (zT) of both the *n*- and *p*-type legs, which is calculated by integrating and averaging the zT curve between T_h and T_c :^{30,31}

$$zT_{ave} = \frac{1}{T_h - T_c} \int_{T_c}^{T_h} zT dT. \quad (2-5)$$

Therefore, highly efficient thermoelectric power generation and cooling rely on thermoelectric materials that exhibit high zT_{ave} . Typically, as shown in **Figure 2.2(b)**, for thermoelectric materials with zT_{ave} of 1, $\eta_p \approx 4\%$ can be expected under $\Delta T = 70$ K.³² Although each thermoelectric unit provides relatively low η_p , output power can be enhanced by connecting a larger number of units.^{33,34} As a result, microwatt even milliwatt-scale output power can be

achieved with ΔT of 10 K³⁴ or 20 K³⁵ (such a ΔT value can be provided between human body and environment), which satisfies the power requirement of many wearable electronics, such as wrist watches or hearing aids.³⁶

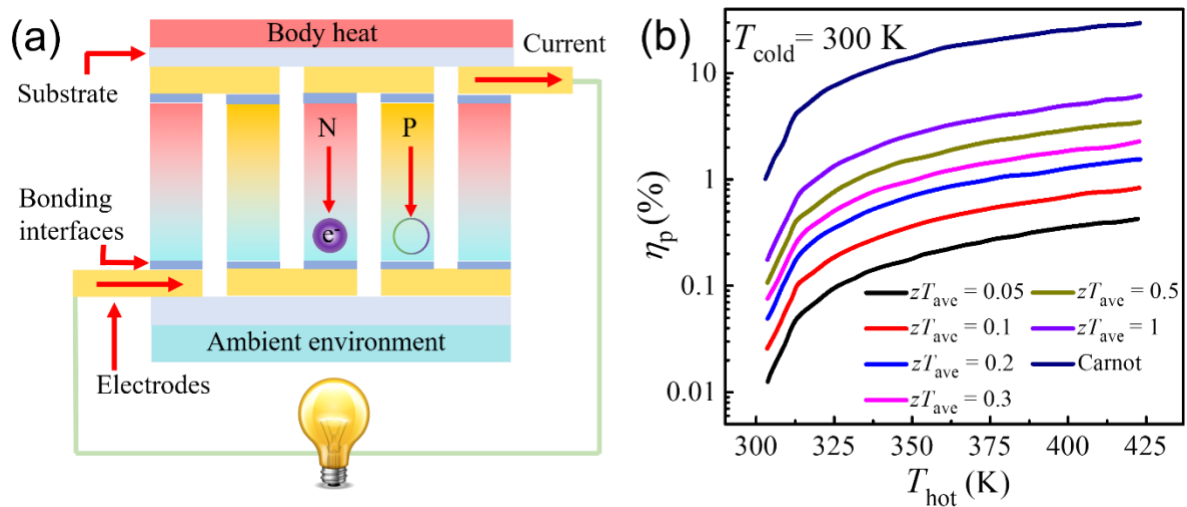


Figure 2.2 (a) Typical structure of the thermoelectric device composing of the substrate, TE legs, connecting electrodes and bonding interfaces. (b) Power generating efficiency (η_p) of thermoelectric devices as a function of average figure of merit (zT), zT_{ave} of materials.

2.2 Chief characteristics of Bi₂Te₃-based thermoelectric materials

2.2.1 Crystal and electronic band structures

Bi₂Te₃ has attracted intense attentions as one of the best low-temperature thermoelectric materials.^{31,37-40} The crystal structure of Bi₂Te₃ belongs to rhombohedral tetradymite, with the space group of $R\bar{3}m$.⁴¹ The crystal structure of Bi₂Te₃ is schematically depicted in **Figure 2.3**, where the unit cell is composed of five monatomic layers stacking along c -axis in the sequence of -Te(1)-Bi-Te(2)-Bi-Te(1)-Te(1)-Bi-Te(2)-Bi-Te(1)-. These layers are also known as quintuple layers and different numbers have been used to denote anions (Te), which are based on their bonding environments. Specifically, the bonding effects between adjacent Te(1) layers are weak van der Waals forces, while Bi and Te(2) layers are primarily connected by covalent bonding, with a tiny ionic contribution.⁴² Due to such a crystal structure, Bi₂Te₃ typically possess layered structure with heavy atoms, which is potentially beneficial for low κ .

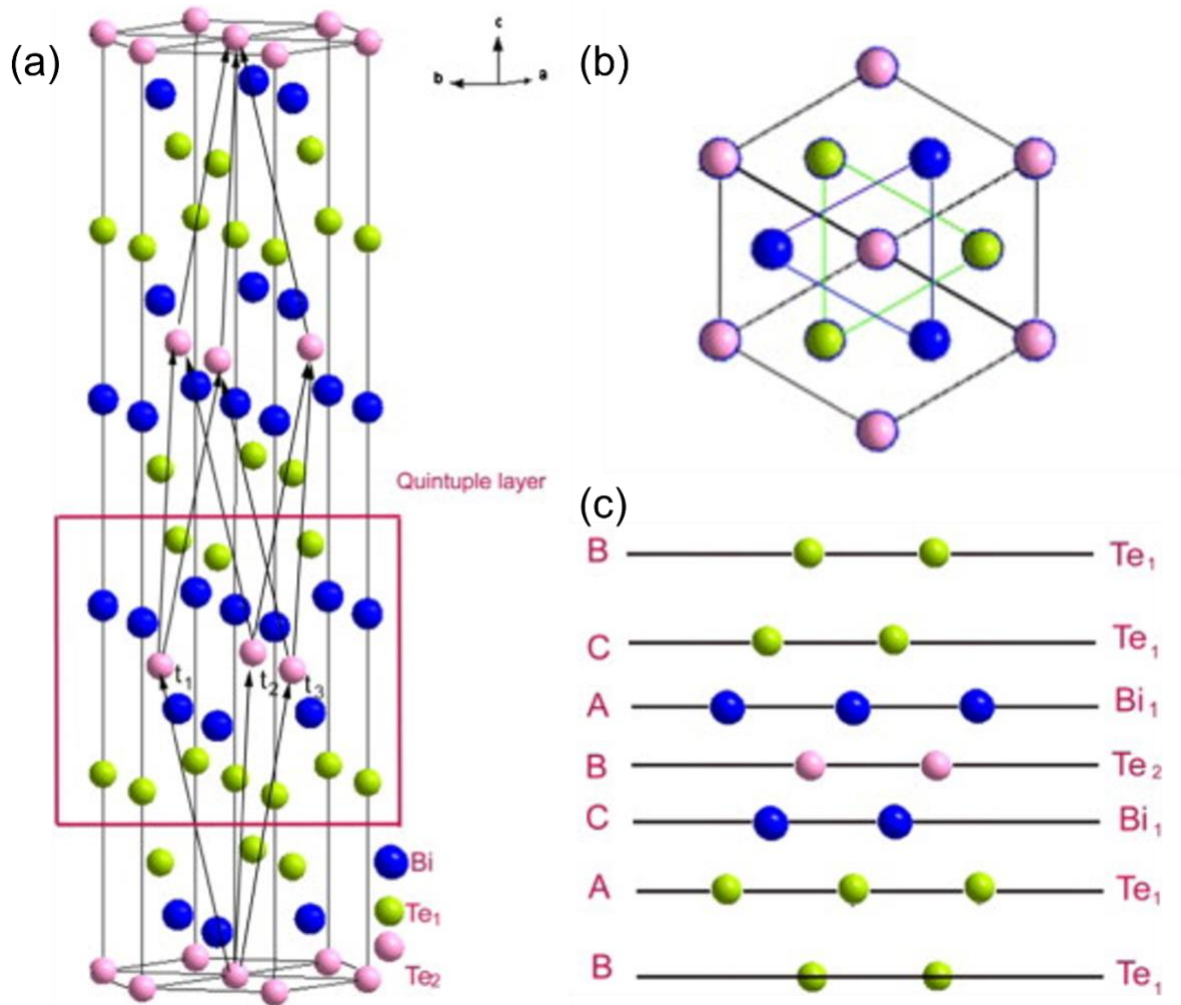


Figure 2.3 (a) Front view, (b) top view and (c) side view of Bi_2Te_3 crystal structure, with the quintuple layer highlighted containing five monatomic layers stacking along c -axis in the sequence of $-\text{Te}(1)\text{-Bi-Te}(2)\text{-Bi-Te}(1)-$.

In terms of the electronic band structure, Bi_2Te_3 shows narrow band gaps (~ 0.15 eV) and relatively high band degeneracy,⁴³ as shown in **Figure 2.4**. Six valleys are calculated by pseudo potential model to exist at both the highest valance band and lowest conduction bands, the energy separations of the second conduction and valance band are 30 meV and 20 meV, respectively.⁴⁴ Since narrow band gaps may contribute to decent σ , while high band degeneracy can lead high $S_{2\sigma}$, Bi_2Te_3 is anticipated to exhibit intrinsically splendid electrical properties.

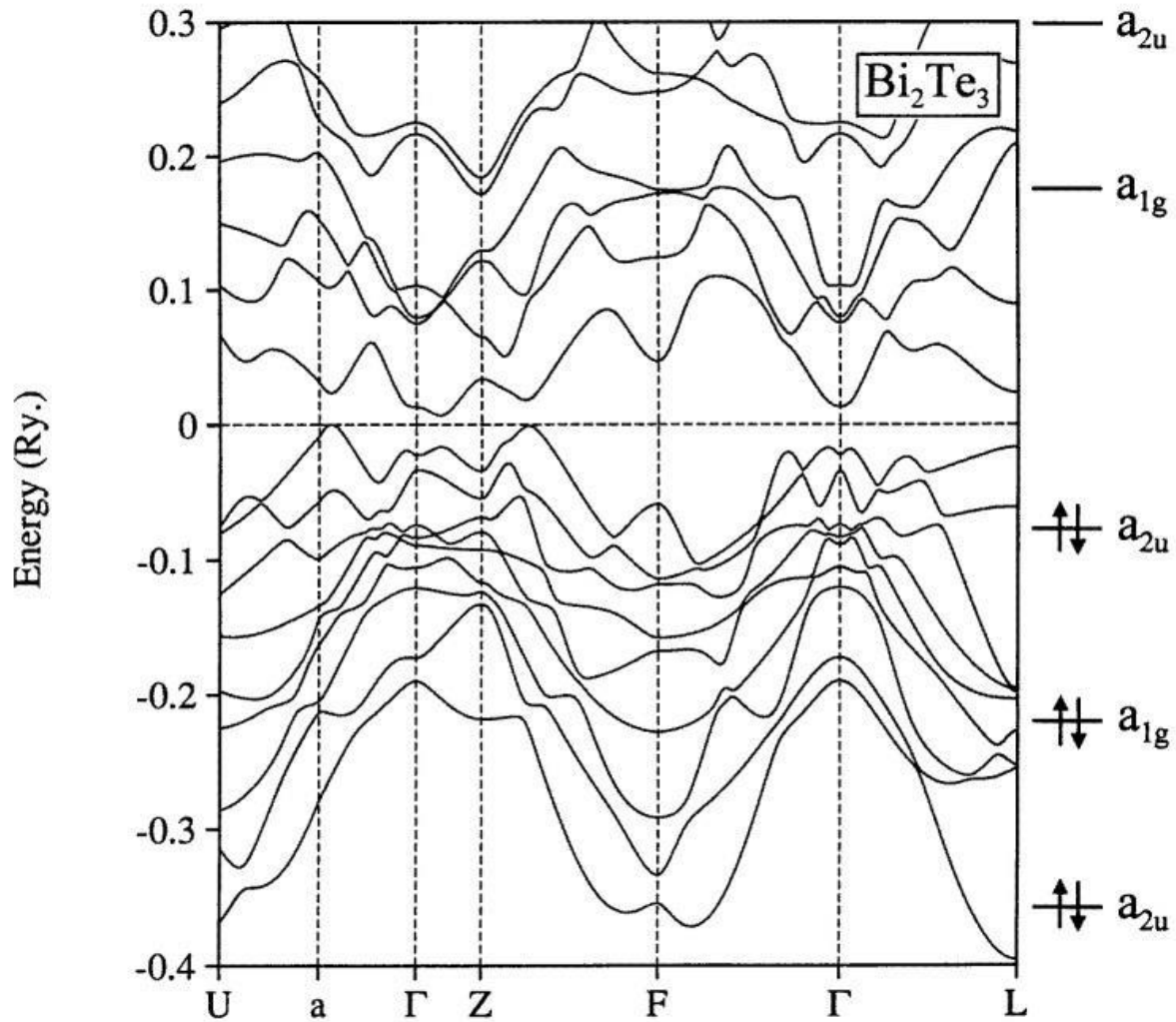


Figure 2.4 Typical electronic band structure of Bi_2Te_3 .⁴⁴

2.2.2 Strong anisotropy

Due to the layered crystal structure of Bi_2Te_3 , the lattice parameter along the c -axis (~ 3.045 nm) is much larger than that along the a, b -axis (~ 0.438 nm),⁴² which act as the essential reason to result in the strong anisotropic behaviours of Bi_2Te_3 . Specifically, σ and κ in the a - b plane, which is the plane perpendicular to c -axis, can be roughly four and two times larger than that in the c plane.⁴⁵ With modified synthesis and fabrication technique, such anisotropy ratios may be even higher.^{46,47} On the other hand, S doesn't show obvious anisotropic behaviours, showing similar values in both a - b plane and c plane. The strong anisotropy of Bi_2Te_3 can be mitigated by nanostructure engineering,^{31,37} where nanosized grains are expected to distribute randomly in the pellet. However, this meanwhile may deteriorate $S_{2\sigma}$.

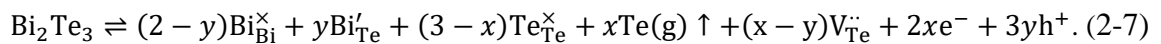
2.2.3 Intrinsic point defects

Intrinsic point defects including anti-site defects and vacancies widely exist in Bi₂Te₃-based thermoelectric materials, which are on a par with extrinsic point defects to impact n .⁴⁸⁻⁵⁰ As discussed above, thermoelectric parameters σ , S and κ_e are strongly correlated with each other by n . Therefore, considerations on intrinsic point is necessary and might play a pronounced role in boosting thermoelectric performances. For Bi₂Te₃-based thermoelectric materials, the stoichiometry is barely retained during the fabrication, due to the facile evaporation or precipitation of Te, leading Bi excess.^{51,52} To this end, anti-site defects of Bi at Te sites (Bi'_{Te}) and Te vacancies ($V_{Te}^{\cdot\cdot}$) are two predominant intrinsic point defects of Bi₂Te₃-based thermoelectric materials, which correspond to the generations of p - and n -conduction types, respectively. The mechanism of x mol $V_{Te}^{\cdot\cdot}$ to generate n -type semiconductors is shown below:



where Bi_{Bi}[×] and Te_{Te}[×] stand for original Bi and Te atoms without the point defects, Te(g) represents the evaporation of Te. It can be found that x mol $V_{Te}^{\cdot\cdot}$ can produce $2x$ mol extra electrons.

On the basis of this, y mol Bi'_{Te} tend to generate y mol extra holes and transform semiconductors towards p -type, whose mechanism can be revealed by the following equation:



It should be noted that Bi'_{Te} dominates in Bi₂Te₃ single crystal or ingots with coarse grain sizes, therefore they are intrinsically p -type. For nanostructured or polycrystalline Bi₂Te₃ with fine grains, small grains lead increased number of dangling bonding at the grain boundaries due to Te deficiency, which can be considered as $V_{Te}^{\cdot\cdot}$ contributing extra electrons. Hence, nanostructured Bi₂Te₃ or polycrystalline Bi₂Te₃ with fine grains are typically n -type.

The formations of intrinsic point defects can be motivated by the electronegativity and covalent radius of cations and anions.^{53,54} Specifically, the closer electronegativity and covalent radius are, the easier anti-site defects tend to be formed; the more different electronegativity and covalent radius are, the more vacancies tend to be generated. Specially, the formation energy of Bi'_{Te} in cation-rich Bi₂Te₃ can be estimated using below equation deriving from statistical thermodynamics:⁵⁵

$$E_{\text{Bi}'_{\text{Te}}} = -k_b T_m \left(\ln \frac{n_{\text{Bi}'_{\text{Te}}}}{N_{\text{Te}}} + 1 \right), \quad (2-8)$$

where k_b is the Boltzmann constant, T_m the melting point, $n_{\text{Bi}'_{\text{Te}}}$ is the number of Bi'_{Te} per cm³, and N_{Te} is the number of available Te sites per cm³, respectively. Typically, the formation energy of anti-site defects in Bi₂Te₃ is 0.5 eV.^{55,56}

Apart from the impacts on n , point defects may also reduce κ by scattering high-frequency phonons.^{57,58} With point defect engineering, properly designed point defects hold full potential to optimize zT of Bi₂Te₃-based thermoelectric materials. In spite of these advantages, the generation and manipulation of point defects are still challenging to be qualitatively controlled, which may potentially cause the irreproducibility.

Besides aforementioned characteristics, Bi₂Te₃-based thermoelectric materials also possess bipolar effect at relatively high temperatures, where minor carriers tend to be thermally excited to neutralize major carries and in turn effect S and κ .⁵⁹ Since this project aims to develop high-performance Bi₂Te₃-based thermoelectric materials for energy harvesting and generations at the low temperature, bipolar effect is not elaborated. Relevant studies are recommended here.^{60,61}

2.3 Progresses and optimization strategies of Bi₂Te₃-based thermoelectric pellets

In this section, progresses and optimization strategies of Bi₂Te₃-based thermoelectric pellets are summarized, which include point defect and texture engineering, as well as phonon scattering strengthening.

2.3.1 Point defect engineering

Since point defects prevalently exist in Bi₂Te₃-based thermoelectric pellets and may significantly affect their thermoelectric performances, manipulating point defects, namely point defect engineering, is of vital significance, which can be implemented during pre-synthesis, in-synthesis and post-synthesis periods.

During the pre-synthesis period, compositional controls using isoelectron extrinsic dopants or heteroelectron extrinsic dopants have been evidenced to be effective strategies to effect the formations of point defects. Specifically, for isoelectron extrinsic dopants, the general principle is that substitutions of cations and anions with more electronegative or smaller atoms tend to promote the formations of anti-site defects and vacancies, respectively. Since anti-site Bi'_{Te} can contribute extra holes and V_{Te}^{••} can provide extra electrons, isoelectron extrinsic doping can transform semiconductors towards p -type or n -type conduction.^{62,63} Two typical examples are p -type Bi_{2-x}Sb_xTe₃⁶⁴ and n -type Bi₂Te_{3-x}Se_x,⁶⁵ which currently serve as two best commercial low-temperature thermoelectric materials. As shown in **Figure 2.5(a)** and **(b)**, substituting Bi with increasing Sb in Bi_{2-x}Sb_xTe₃ can effectively improve n_h from initial $\sim 1 \times 10^{19}$ to $\sim 9 \times 10^{19}$ cm⁻³,^{64,66,67} while substituting Te with smaller Se or S can realize the transformation of Bi₂Te₃ from p -type to n -type, obtaining growing n_e with increasing Se or S.⁶⁷⁻⁶⁹ In terms of

heteroelectron extrinsic dopants such as Cu,⁷⁰ Ag,⁷¹ Pb,⁷² I⁷³ and Mn,⁷⁴ the doping has been found to alter the formation energy of point defect, therefore changing n and possibly shifting the peak-performance temperature of the material.⁴⁵ One typical example is Cu doped n -type Bi₂Te_{2.7}Se_{0.3}, where tiny amount of Cu can increase the formation energy of V_{Te}^{••} and in turn prevent Te escaping, which ultimately boost peak zT from 0.85 to 1.1.⁷⁵

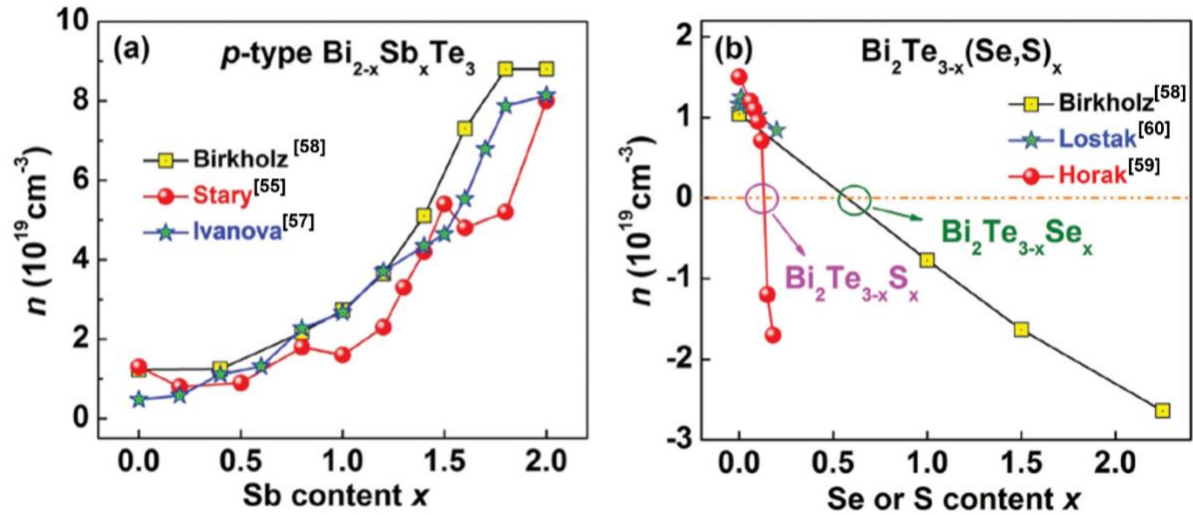


Figure 2.5 Isoelectron extrinsic doping of p -type Bi₂Te₃ to manipulate point defects formation, with (a) Sb to form p -type Bi_{2-x}Sb_xTe₃^{55,57,58} and (b) Se or S to transform into n -type Bi₂Te_{3-x}(Se,S)_x.⁵⁸⁻⁶⁰

Point defects can be also manipulated during the synthesis by controlling the synthesis environment. For zone-melted (ZM) p -type Bi_{0.5}Sb_{1.5}Te₃, it is found that excess Te can increase the formation energy of anti-site defects, and in turn suppress the generation of anti-site defects.⁵¹ On the other hand, excess Bi can boost the formation of Bi_i'_{Te} in ZM p -type Bi₂Te₃ ingot, which consequently lead increased nh .⁷⁶

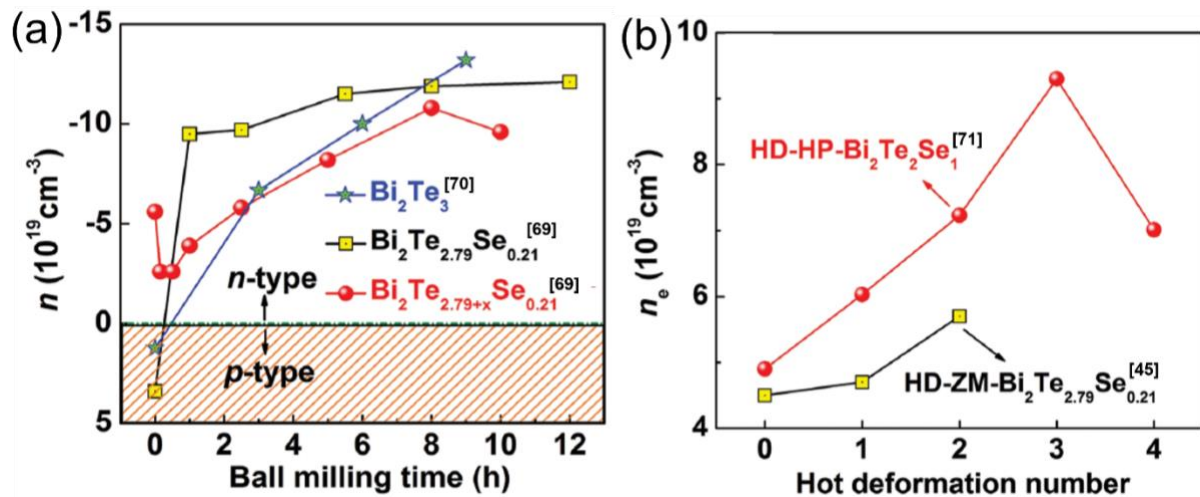
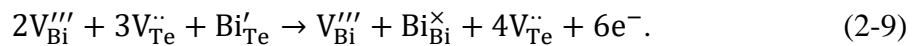


Figure 2.6 Donor-like effect of Bi₂Te₃ to generate extra n_e , induced by (a) balling milling^{77,78} and (b) hot deformations.^{54,79,80}

Lastly, point defects are also possible to be manipulated during the post-synthesis period through the mechanical deformation^{81,82} or post-annealing,^{54,65,80} where donor-like effect and recovery effect have been proposed to uncover the mechanism, respectively. For the donor-like effect of mechanical deformations, it describes the production of extra $V_{Te}^{\cdot\cdot}$ induced by non-basal slip after the plastic mechanical deformation, whose process can be expressed as:



Specifically, non-basal slip can generate extra $V_{Bi}^{\prime\prime\prime}$ during the deformation process, which can subsequently inhibit Bi_{Te}^{\prime} by inducing Bi atoms to diffuse from Te sites back to their initial sites.⁷⁹ In this way, extra $V_{Te}^{\cdot\cdot}$ is generated and in turn contribute to increased n_e . Donor-like effect can be induced by various methods, including grinding, ball milling (BM), extrusion and hot deformation (HD). **Figure 2.6(a)** shows the donor-like effect in Bi₂Te₃⁷⁸ and Bi₂Sb_{2.79}Te_{0.2177} induced by ball milling. Both Bi₂Te₃ and Bi₂Te_{2.79}Se_{0.21} realize the transformation from p -type to n -type due to the generation of extra $V_{Te}^{\cdot\cdot}$. The increased n_e with balling milling time indicates the occurrence of intensified donor-like effect. Besides, hot deformation was also reported to trigger the donor-like effect, as shown in the cases of Bi₂Te₂Se₁₅₄ and Bi₂Te_{2.79}Se_{0.2180} in **Figure 2.6(b)**. Even though the boost of n_e is visible, the promotion is not as significant as ball milling. This might because of the milder deformation brought by hot deformation than that of the ball milling. In terms of the recovery effect in Bi₂Te₃-based thermoelectric materials leaded by post-annealing, it depicts the annihilation of $V_{Bi}^{\prime\prime\prime}$ with the dislocation climb and array formation during the annealing process.⁸¹ With the dampened $V_{Bi}^{\prime\prime\prime}$, the donor-like effect is countered, which therefore contribute reduced n_e . Similar to intensified donor-like effect induced by heavy plastic deformation, more significant recovery effect may occur with higher annealing temperatures.^{65,83}

2.3.2 Texture engineering

Bi₂Te₃-based thermoelectric materials have intrinsic strong anisotropy, which could cripple $S2\sigma$ and improve κ in some cases. Manipulating the crystalline alignment using the texture engineering hold the potential to prevent above issues and therefore optimize zT . So far, texture engineering has been applied to p -type Bi_{2-x}Sb_xTe₃,⁸⁴ n -type Bi₂Te₃₈₅ and Bi₂Te_{3-x}Se_{x86} to boost their zT . However, different mechanisms are proposed. For p -type Bi_{0.5}Sb_{1.5}Te₃,⁸⁴ texturing engineering is employed by hot forging as-sintered pellet to weaken the strong anisotropy (i.e.

oriented textures). Consequently, additional defects can be generated, as shown in **Figure 2.7(a)** and **(b)**, leading reduced n_h from 4.56×10^{19} to 3×10^{19} cm⁻³ and in turn improved S and $S_2\sigma$. Meanwhile, extra defects induce intensified phonon scatterings and decreased κ , ultimately achieving peak zT of 1.3 at the room temperature.⁸⁴

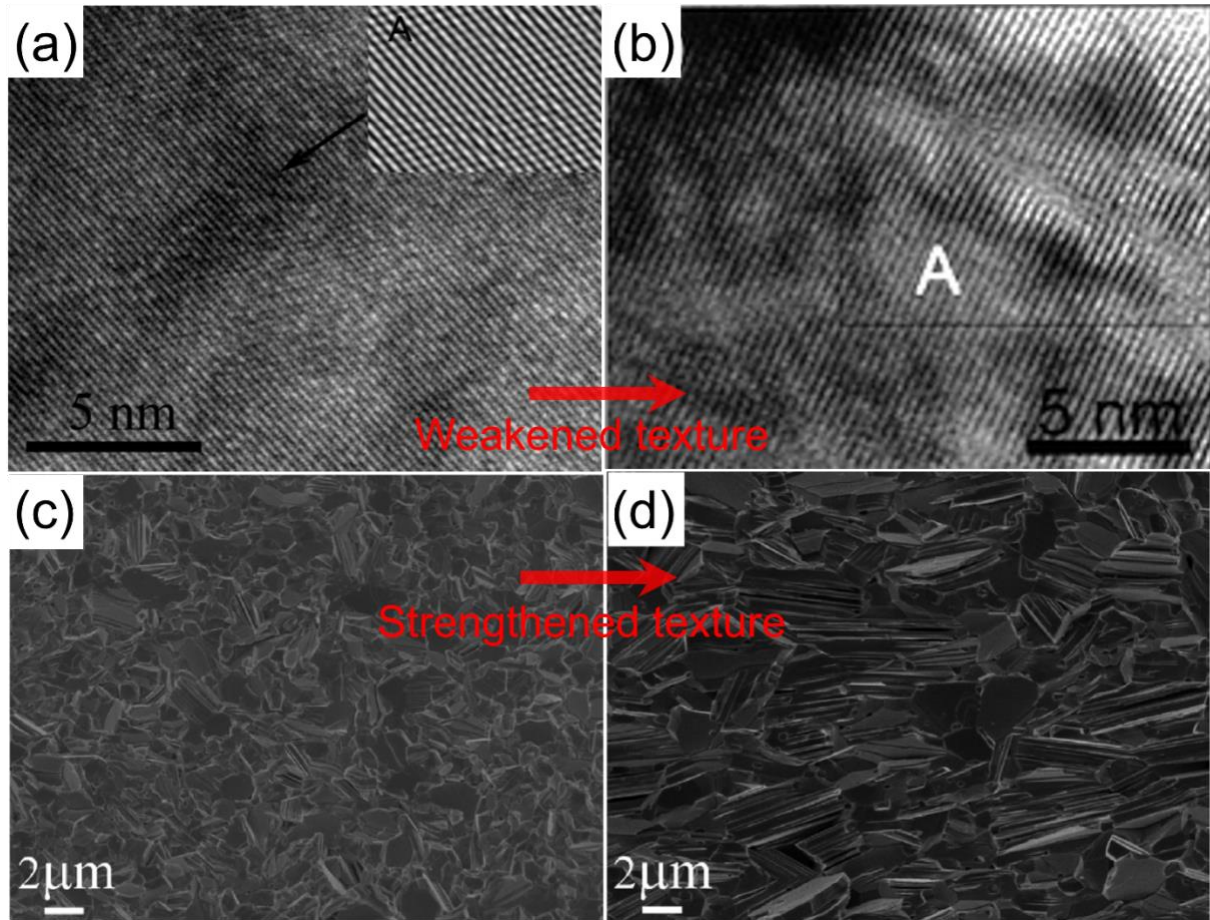


Figure 2.7 Texture engineering towards Bi₂Te₃ family with improved zT , where (a) texture of p -type Bi_{0.5}Sb_{1.5}Te₃ is weakened (b) after hot forging,⁸⁴ texture of n -type Bi₂Te_{2.7}Se_{0.3} is weakened (b) after sample repressing.⁸⁶

In regards to n -type Bi₂Te_{2.7}Se_{0.3},⁸⁶ it was found that enhancing the texture can dramatically elevate σ in spite of the slightly increased κ . Enhanced texture can be achieved by repressing as-sintered pellet in the furnace under the protective nitrogen gas, using larger graphite die than the initial sintering. As a result, as shown in **Figure 2.7(c)** and **(d)**, plate-like grains are clearly observed from the top-view scanning electron microscope (SEM) image of the plane perpendicular to the sintering direction, indicating the preferential texture. Effective zT improvement of 22% has been witnessed from n -type Bi₂Te_{2.7}Se_{0.3}, with peak zT from 0.85 to

1.04 at 125 °C.⁸⁶ Although texture engineering presents effects on σ and κ of Bi₂Te₃-based thermoelectric materials, S is found to be rarely changed, showing the isotropic feature.

2.3.3 Phonon scattering strengthening

Reducing κ serves as another effective strategy to improve zT . By strengthening phonon scattering, κ_l of Bi₂Te₃-based thermoelectric pellets has been reported to be significantly inhibited. In this section, strategies to strengthen phonon scattering are mentioned, which include nanostructure engineering, ball milling and melt spinning.

For nanostructured thermoelectric pellets, strong phonon scattering can be induced at the dense grain boundaries, which in turn lower κ_l . In Bi₂Te₃-based thermoelectric family, different nanostructures such as nanoplates,^{37,38} nanowires,^{87,88} nanosheet,⁸⁹ nanoflower,⁹⁰ and Te-Bi₂Te₃ hierarchical nanostring-cluster nanostructure^{91,92} have been reported, where significantly reduced κ is obtained, 50% less than that of the ingot,⁹³ as shown in **Figure 2.8**. During the synthesis of nanostructures, surfactant such as polyvinylpyrrolidone (PVP) is often used to modulate the surface tension and realize the preferential crystal growth. This meanwhile brings the potential issue of residual surfactant, which may deteriorate electrical properties of the final thermoelectric pellet. This to some extent can be prevented by thorough deionized water or ethonal washing during the sample collection. Besides, exploring nanostructure synthesis without surfactant is a promising path deserving future studies.

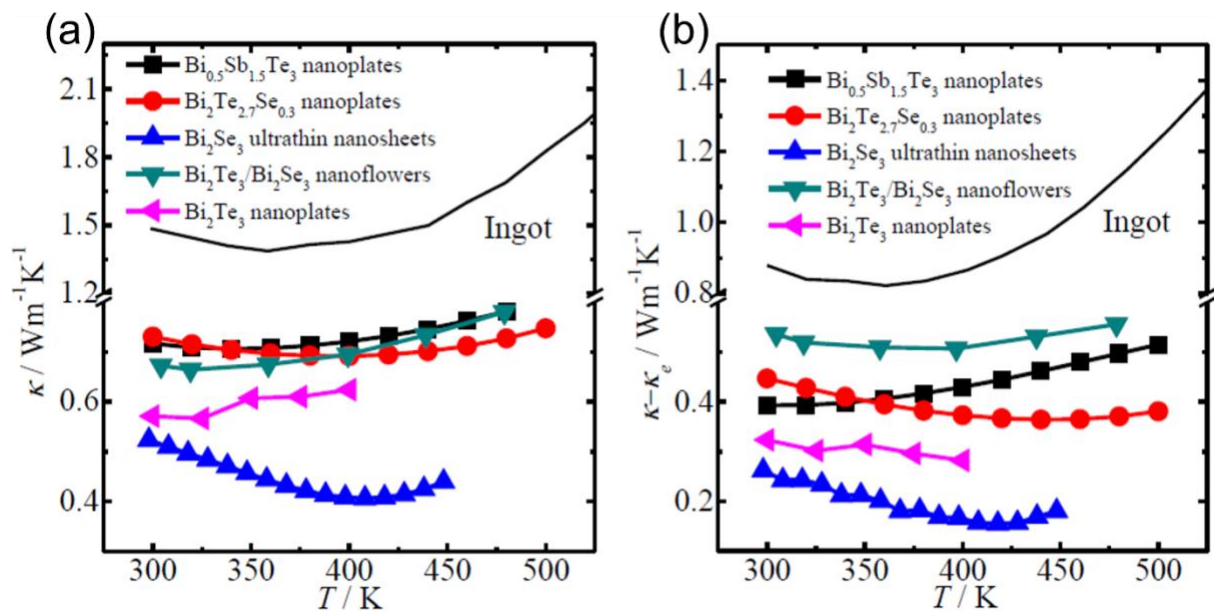


Figure 2.8 Significant decreased (a) κ and (b) κ_l of nanostructured Bi₂Te₃ family compared with the ingot counterpart.^{39,58,90,94,95}

Direct synthesis of nanostructure can be also realized by fast melt spinning (MS) approach, where short synthesis time constrains the crystal growth forming nano-sized grains. For example, 26% κ reduction was reported from MS-fabricated *p*-type Bi_{0.52}Sb_{1.48}Te₃ compared with ZM-fabricated counterpart, presenting κ as low as 0.67 W m⁻¹ K⁻¹ and promising zT of 1.56 at 300K.⁹⁶ However, MS is not found to obviously reduce κ of *n*-type Bi₂Te₃-based thermoelectric materials.⁹⁷ Apart from direct nanostructure synthesis, nanostructures can be also fabricated *via* post-synthesis ball milling,⁴⁵ which can be realized by either grinding as-synthesis ingot to obtain fine powders, or utilizing high-energy mechanical alloying method to form the pure phase. Bi₂Te₃-based thermoelectric materials processed by ball milling have witnessed effective zT improvements.⁹⁸

Considering the interdependence of various thermoelectric parameters, optimizations of zT are usually accompanied with multi-strategies application. To this end, compromises between carries transport, band structure and phonon scatterings need to be sought.¹²

2.4 Progresses and optimization strategies of Bi₂Te₃ family thermoelectric films

Apart from pellets, Bi₂Te₃ family thermoelectric materials can be also fabricated into flexible thermoelectric films, which is currently quite attractive to power flexible electronics.⁹⁹ In this section, progresses and optimization strategies of Bi₂Te₃ family thermoelectric films are reviewed.

In order to endow rigid Bi₂Te₃ family crystals with flexibility, conductive polymers and carbon nanomaterials have been respectively incorporated with Bi₂Te₃ family fillers, acting as the flexible matrix. Conductive polymers possess intrinsically σ -independent low κ ,³² and decent flexibility. Carbon nanomaterials present high σ , intrinsic flexibility, and superior mechanical properties.^{100,101} Considering Bi₂Te₃ family shows relatively high electrical properties.¹⁰²⁻¹⁰⁸ Therefore, a strategy of fabricating Bi₂Te₃ family/conductive polymer or carbon nanomaterials hybrids can be expected to inherit the merits of both components and realize the synergistic optimization of electrical and thermal properties. Currently, due to their relatively high zT and facile solution process-ability, PEDOT:PSS^{32,109,110} and PANI^{32,111} are the mostly commonly used conductive polymers for hybrids. Considering the low κ of the conductive polymer matrix,¹¹² current strategies mostly focus on the optimization of system electrical properties, with the strategies including the polymer/filler interfacial energy-filtering effect¹¹³ and control over the condition of the filler surface ¹¹⁴. In particular, polymer/filler interfaces can introduce an energy-filtering effect that may significantly increase S . Rational control over the filler

surfaces may effectively reduce the contact resistance of the polymer/filler interfaces and affect carrier interfacial transport which could potentially boost σ . As for carbon nanomaterials, free-standing CNT scaffolds have been developed as a base from which to grow Bi₂Te₃ family materials.¹¹⁵

2.4.1 Energy-filtering effect

The Energy-filtering effect has been extensively studied in inorganic thermoelectrics in order to effectively improve S with minor impact on σ , and in turn obtain optimized $S^2\sigma$.^{24,116,117} For conductive polymer composites, the energy-filtering effect can be induced at polymer/filler interfaces by appropriate design of band structures.^{110,113,118} **Figure 2.9** shows that, when there is an energy offset between transport bands of the filler and polymer, an energy barrier (ΔE_g) is generated at the interface. Only carriers with an energy of $>\Delta E_g$ can pass the barrier while those with an energy of $\leq\Delta E_g$ can be blocked. Calculation results¹¹⁶ have shown that low energy carriers negatively contribute to S , while carriers with an energy of between 0.05 and 0.1 eV contribute most of S . Therefore, filtered carriers with higher average energy can contribute to the enhanced S . n may be reduced after filtering and this leads to a slightly lower σ . However, since $S^2\sigma$ is more dominated by S than σ , optimization of $S^2\sigma$ is still possible.¹¹⁹

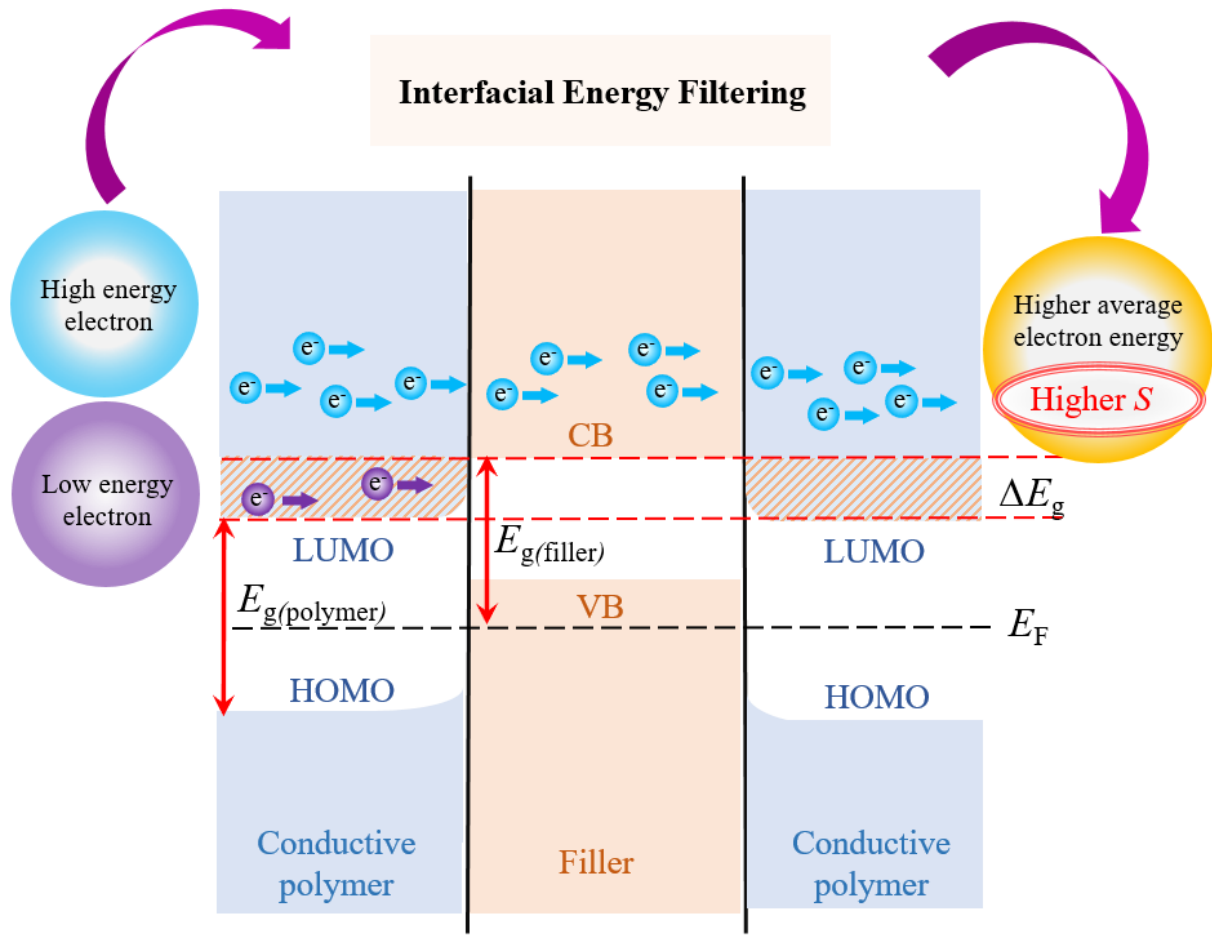


Figure 2.9. Schematic illustration of the energy-filtering effect at the interface between the conductive polymer and the filler.

In terms of the impact of band structure on energy-filtering effect, calculations indicate that an appropriate ΔE_g in the range of 0.04 eV - 0.1 eV can induce an effective energy-filtering effect.¹²⁰ Larger ΔE_g may trap carriers by forming energy barriers at the interface and therefore reduce μ and deteriorate σ .¹¹³ This prediction has been experimentally reflected in the Bi₂Te₃ incorporated P3HT composite.¹¹³ Variation of ΔE_g has been obtained from 0.1 to 0.2 eV by using different doping levels of P3HT. As a result, a higher $S_2\sigma$ of 13.6 $\mu\text{W m}^{-1} \text{K}^{-2}$ can be achieved with heavily doped P3HT,¹¹³ where ΔE_g below 0.1 eV induces more effective energy-filtering process and significantly improve S .

2.4.2 Filler surface modification

Filler surface status plays a critical role of interfacial carriers transport. By modifying filler surface status and reducing the interfacial contact resistance, electrical properties of the system are anticipated to be boosted. Most surfaces of inorganic thermoelectric semiconductors or

metal particle fillers are usually oxidized during fabrication. Such an oxidation layer can deteriorate σ . One solution is to clean the oxidized surfaces of fillers through chemical treatment. Zhang *et al.*¹¹⁴ fabricated Bi₂Te₃/PEDOT:PSS composites by drop-casting PEDOT:PSS on a pre-cast *p*-type Bi₂Te₃ film. **Figure 2.10(a)** shows a typical SEM image of the fabricated composites, in which PEDOT:PSS was deposited on the top of fillers with some infiltration into filler gaps. Oxidation on the Bi₂Te₃ surfaces during casting causes high contact resistivity with PEDOT:PSS, which blocks carrier transport.¹¹⁴ By rinsing Bi₂Te₃ particles in HCl solution, the surface oxidation layer can be effectively removed and this results in a better conductive interface with PEDOT:PSS. **Figure 2.10(b)** shows that an improved $S_2\sigma$ of 131 $\mu\text{W m}^{-1} \text{K}^{-2}$ was achieved in *p*-type Bi₂Te₃/PEDOT:PSS composites at room temperature.

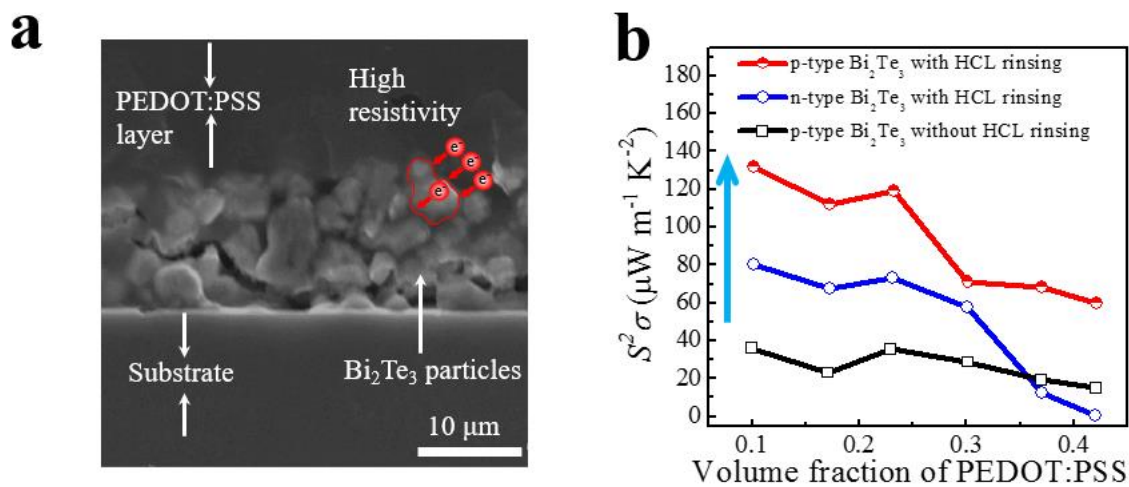


Figure 2.10. Effects of filler surface status in conductive polymer composites. (a) SEM image of cross section of Bi₂Te₃/PEDOT:PSS thin films,¹¹⁴ where high contact resistivity between Bi₂Te₃ filler and PEDOT:PSS is emphasised by the red solid line. (b) Significant enhancement of the power factor ($S_2\sigma$) after the removal of the oxidation layer on the filler surface through acid rinsing. Reproduced with permission.¹¹⁴

Besides aforementioned strategy, we also developed one strategy in this project to effectively reduce interfacial contact resistance, by facilely coating Bi_{0.5}Sb_{1.5}Te₃ fillers with highly conductive CuTe layers. Relevant work has been submitted for publication, which will be elucidated in **Chapter 6**.

2.4.3 Carbon-nanotube scaffolds

Due to their high σ , intrinsic flexibility, and superior mechanical properties, CNTs show great potential as flexible thermoelectric materials. Early studies show that Ar-plasma treated CNTs show a promising zT of 0.4.^{100,101} Very recently, free-standing CNT scaffolds have been

developed as a base from which to grow TE materials.¹¹⁵ These scaffolds involve a SWCNT network which can be used to guide the deposition and growth of layer-structured Bi₂Te₃-based nanocrystals to form a hybrid with highly ordered microstructure, as shown in **Figure 2.11**.¹¹⁵ Such an ordered arrangement can boost σ to ~ 527 S cm⁻¹ in the in-plane direction at room temperature. Furthermore, the ordered Bi₂Te₃-SWCNT interfaces can suppress the scattering of carriers during interfacial transport, while dampening κ due to the mismatch of phonon spectra between SWCNT and Bi₂Te₃. A few nanopores can also be found in the hybrid, which further contributes to phonon scattering and this further decreases κ . As a result, record zT of 0.89 has been obtained at room temperature.¹¹⁵ Such a CNT scaffold paves the way for the design and fabrication of high-performance flexible thermoelectric materials and generators by combining layer-structured Bi₂Te₃ materials with CNT networks.

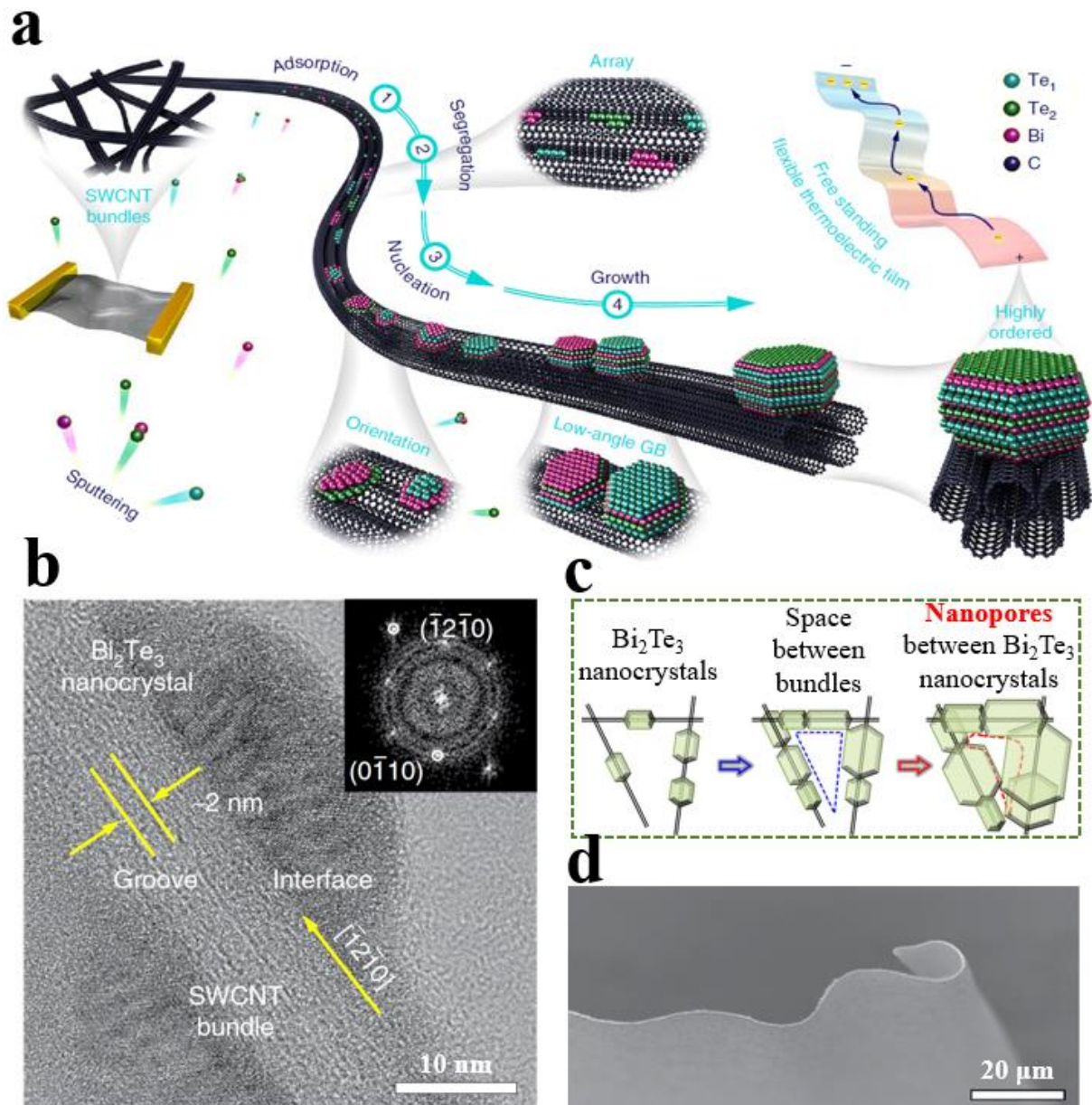


Figure 2.11. Fabrication of free-standing FTE thin films by applying carbon-nanotube scaffold.¹¹⁵ (a) Schematic of the fabrication of a free-standing highly ordered Bi₂Te₃–SWCNT FTE thin film. (b) A bright-field TEM image of the interface between Bi₂Te₃ nanocrystals and the SWCNT bundle. Inset: corresponding fast Fourier transform (FFT) pattern of the Bi₂Te₃. (c) Schematic of the generation of nanopores during Bi₂Te₃ nanocrystal growth. (d) Cross-sectional SEM image of free-standing Bi₂Te₃–SWCNT FTE thin film.

2.4.4 Physical vapour deposition

Apart from flexible thermoelectric hybrids, continuous inorganic films on flexible substrates with the thickness sufficiently thin (below 1 μm) to prevent cracks during bending, is also promising. This can be achieved by physical vapour deposition techniques.^{121,122}

Physical vapour deposition including magnetron sputtering^{121,123} and thermal co-evaporation deposition are two prevalent methods to directly deposit source materials onto flexible substrates, where the source materials can be ejected through ion bombardment or thermal evaporation,¹²⁴ respectively. For magnetron sputtering, deposition parameters that should be considered when seeking to obtain optimal TE performance include sputtering pressure,^{121,123} and annealing temperature.^{121,122} Higher sputtering pressure has been reported to positively contribute to the crystal structure, leading to high $S_2\sigma$ of 12 $\mu\text{W cm}^{-1} \text{K}^{-2}$ at 468 K in the Bi-Te thin film without the application of annealing processes.¹²³ Higher annealing temperatures can enhance the crystalline nature of the films by reducing microstructural defects.¹²¹ With a higher degree of crystallization, Fan et al. found n of the thin film can be tuned accordingly, and a promising $S_2\sigma$ of 23.5 $\mu\text{W cm}^{-1} \text{K}^{-2}$ has been reported at ~ 533 K with an optimal n .¹²²

For the thermal co-evaporation method, deposition parameters include the evaporation rate¹²⁵ and the substrate temperature.¹²⁶ With higher substrate temperature, larger grain sizes are available because the higher surface mobility and clustering of atoms can be facilitated by more thermal energy.¹²⁶ Higher substrate temperatures meanwhile tend to intensify the re-evaporation of deposited elements, leading to a deviation of the stoichiometry.¹²⁷ Therefore, the evaporation rate should be adjusted accordingly to produce films with an optimal stoichiometry. With optimized substrate temperature and evaporation rate, a promising zT of 0.3 has been achieved in flexible Sb₂Te₃ thin films at room temperature.¹²⁵

Reactive sputtering is another effective method that can be used to fabricate continuous inorganic films on a flexible substrate. Compared with the previously mentioned magnetron sputtering and thermal co-evaporation deposition methods, reactive sputtering can generate a higher plasma density and consequently improve the uniformity of films, when high

conductivity is available from the source material target.¹²⁸ Reactive sputtering has additional advantages as it can be conducted at room temperature, which enables the application of various organic flexible substrates.¹²⁹ A typical example can be found from CuI thin films fabricated on a flexible PET substrate.¹³⁰ However, no relevant works have been reported for Bi₂Te₃ family so far.

2.4.5 Other potential strategies

Apart from the aforementioned, chemical bath deposition and intercalated superlattice engineering are another two potential strategies to fabricate Bi₂Te₃ family flexible thermoelectric films. Despite their applications on Bi₂Te₃ family are still not visible, outstanding outcomes have been found from other thermoelectric systems.

Chemical bath deposition is one effective method to deposit thermoelectric thin films on different substrates.^{131,132} This method can be realized by immersing the substrate into a solution containing precursors, followed by nucleation and growth of the thin film under an appropriate reaction temperature and pH value.¹³³ Different from physical vapour deposition methods, chemical bath deposition can be conducted in the solution and under low temperatures. This method lends itself more easily to larger-scale production. One relevant piece of work was reported by Xun et al.¹³⁴ These investigators fabricated α -Ag₂S thin film on a fluoromica substrate. The as-deposited α -Ag₂S film exhibited semiconducting properties, as well as metal-like ductility and high plastic deformation strains at room temperature.

Intercalated superlattice engineering serves as another promising strategy to realize high-performance organic/inorganic hybrids, which are composed of an inorganic atomic layer and an organic molecular layer.^{135,136} In such a superlattice structure, high $S_{2\sigma}$ can be secured via the inorganic atomic layer while κ can be suppressed by the intercalated organic molecular layer *via* blocking phonon transport in both the in-plane^{136,137} and out-of-plane directions.¹³⁸⁻¹⁴¹ In this situation, extra charge carriers can be generated from intercalation complexes that are formed by chemically bonded organic molecules and inorganic layers.^{137,142} Organic molecules can also endow the superlattice structure with flexibility, since intercalated organic molecules expand the interlayer distance, which enables the development of inorganic layers that are more tolerant towards deformation without deteriorating electrical transport.^{137,142}

Three methods, including mechanical grinding and mixing,¹³⁷ atomic layer deposition (ALD) assisted by molecular layer deposition (MLD)¹⁴³ and electrochemical insertion,¹³⁶ have been employed for proper molecular layer insertion. A relevant review can be found from Tian *et al.*'s work.¹⁴⁴ This review emphasized the mechanisms of each method, demonstrated the

effects of intercalated molecules, and compared the advantages and disadvantages of each method.

2.5 Challenges and opportunities

In spite of above progresses, there are still several challenges for Bi₂Te₃-based thermoelectric pellets and films, which are desired to be solved in order to approach increased zT .

(1) n of Bi₂Te₃ pellets still deviates from the predicted optimal value, leading relatively low $S_2\sigma$. Considering the prevalent existence of intrinsic point defects, manipulation of n using point defect engineering is insufficiently studied.

(2) Nanostructured Bi₂Te₃ pellets can induce intense phonon scatterings leading suppressed κ_l and in turn κ . Relevant studies have approached κ close to predicted amorphous limit ($\kappa_{\min}=0.31$ W m⁻¹ K⁻¹ calculated by the Cahill's model). Further κ reduction of Bi₂Te₃ pellets is desired to break the bottleneck and achieve improved zT .

(3) Interfacial carriers transport between Bi₂Te₃-based inorganic fillers and conductive polymers are impeded by high interfacial contact resistances, leading poor σ of Bi₂Te₃ family flexible thermoelectric films. Although optimized interfacial carriers transport have been obtained by modifying filler surface status. The optimization is still limit. Further boost of interface carries transport is scarce.

(4) μ of Bi₂Te₃ family inorganic/organic thermoelectric films is constrained by low crystallinity of conductive polymers and poor interfacial carrier transports. Improving μ can lead the dramatic increase of $S_2\sigma$. However, studies of this aspect are barely reported.

Given above four challenges, studies in this PhD project will aim to provide new solutions and breakthroughs based on previous progresses, which will be elucidated in details in **Chapter 4-6**.

Chapter 3: Methodologies

In this project, Bi_2Te_3 , $\text{Bi}_{0.5}\text{Sb}_{1.5}\text{Te}_3$ and Cu-coated $\text{Bi}_{0.5}\text{Sb}_{1.5}\text{Te}_3$ powders are synthesized by solvo-thermal, solid-solution and electroless plating methods, respectively. After the centrifuging and drying procedure, powders are characterized by X-ray diffraction (XRD) and Scanning Electron Microscopy (SEM) for analysing the chemical composites and morphologies. In order to fabricate Bi_2Te_3 -based thermoelectric pellets, powders are then sintered by spark plasma sintering (SPS) technique and thermoelectric properties are measured by laser-flash method and ZEM-3 equipment. To fabricate Bi_2Te_3 -based thermoelectric films, glass substrates are pre-cleaned by chemical rinsing and plasma treatment equipment in order to enhance their hydrophilia. Then homogeneously mixed inorganic/organic hybrids are spin-coated or drop casted on pre-cleaned glass substrates, which are subsequently dried on heating plate. As-prepared films possess uniform surface and are ready for future characterizations and measurements.

3.1 Synthesis methods of Bi_2Te_3 family powders

In this section, synthesis methods including solvo-thermal, solid-solution and electroless plating methods are introduced, with corresponding principles and features highlighted.

3.1.1 Solvo-thermal synthesis

Among various synthesis methods, solvo-thermal synthesis is known for its ability to realize control over the shape distribution, size and crystallinity of products through tuning experimental parameters including reaction time, reaction temperature, precursor type, solvent type and surfactant type.^{15,38,46,145-147} Here, we take advantage of solvo-thermal synthesis to synthesize *n*-type Bi_2Te_3 nanoplates. The reactor for taking solvo-thermal synthesis is autoclave described as a steel pressure vessel, as shown in **Figure 3.1(a)**. The autoclaves are always put into the laboratory oven for taking the procedure of chemical reactions in autoclaves under high temperature, as shown in **Figure 3.1(b)**.

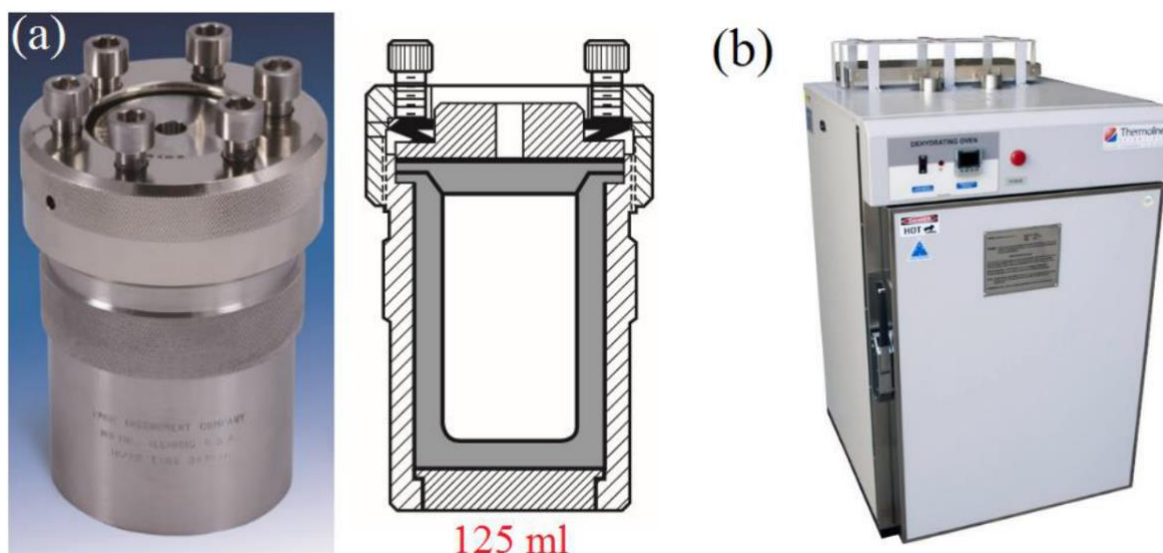


Figure 3.1 Apparatus and oven for solvo-thermal synthesis. (a) Autoclave with its section structure. (b) Laboratory oven used for the hydro- or solvo-thermal synthesis.

Principle and features of solvo-thermal is quite similar with hydro-thermal. Basically, with the increase of pressure and temperature, the ion product of solvent (ethylene glycol in this case) can rapidly increase. Under such an environment, solvents are thoroughly dissociated and act as a molten salt. Moreover, solvent viscosity will also decrease with the rise of temperature. Consequently, the mobility of ions and molecules is boosted compared with normal conditions, which in turn catalyse the occurrence of many chemical reactions.

3.1.2 Solid-solution synthesis

Solid-solution synthesis has advantages such as affordability, high efficiency and facile introduction of dopants or second phase into product.¹⁴⁸⁻¹⁵² In this project, we synthesize *p*-type $\text{Bi}_{0.5}\text{Sb}_{1.5}\text{Te}_3$ powders with solid-solution synthesis, which has been previously reported to exhibit high thermoelectric performances.¹⁵³ Before reaction, precursors are precisely weighed and placed into the quartz tube. Then tubes are sealed under high temperature before thrown into furnace for melting process, as shown in **Figure 3.2 (a)** and **(b)**. Melted precursors are mixed to form desired alloy under high temperature and pressure. Then synthesized alloy is annealed under certain temperature in order to optimize crystal structure and eliminate residual stress. Finally, desired powders are obtain through grinding and particle size may be controlled by grinding time and method. As-synthesised final $\text{Bi}_{0.5}\text{Sb}_{1.5}\text{Te}_3$ powders are shown in **Figure 3.2 (c)**.



Figure 3.2 Quartz tube and furnace for solid-solution synthesis. (a) Quartz tube with pre-weighted precursors inside. (b) Laboratory furnace used for solid solution synthesis. (c) As-ground $\text{Bi}_{0.5}\text{Sb}_{1.5}\text{Te}_3$ powders.

3.1.3 Electroless plating synthesis

Electroless plating which is also known as chemical or auto-catalytic plating, is a non-galvanic plating method that involves several simultaneous reactions in an aqueous solution. Due to the absence of external electrical power, this method is widely applied for chemical coating.¹⁵⁴⁻¹⁵⁷ It was utilized in this project to plate $\text{Bi}_{0.5}\text{Sb}_{1.5}\text{Te}_3$ particles with copper.

Basic procedures include pretreatment towards $\text{Bi}_{0.5}\text{Sb}_{1.5}\text{Te}_3$ powders with 5% HNO_3 solution in order to improve the interactions between powders and plated Cu, plating process in solution consisting of copper sulfate, formaldehyde as the reducing agent, EDTA-2Na as the complex agents and sodium hydrate to provide the alkaline environment. The coating process lasts for 1 h at 330 K under the sonication. As-coated powders are alternatively washed by deionized water and ethanol for at least three times, before being collected by centrifugation and dried at 330 K in the oven overnight. The powders are ultimately reduced under H_2 atmosphere at 580 K for 1 h, and naturally cooled down to the room temperature. As-reduced powders are sealed in the vacuum and ready for the next step.

3.2 Fabrication methods of Bi_2Te_3 family films

In this section, plasma treatment and spin coating are illustrated to pre-clean the glass substrate and fabricate Bi_2Te_3 family films, respectively.

3.2.1 Plasma treatment towards glass substrates

Plasma treatment can be used to introduce oxygen-containing groups on the surface of relatively inert polymer,¹⁵⁸ which will improve the wetting characteristic of an otherwise hydrophobic membrane, therefore making it more favourable for applications. The equipment

and principle of plasma treatment are shown in **Figure 3.3(a)** and **(b)**, where high energy level of the plasma can selectively break or open the structure of chemical or organic substances on the surface of material. Using ultrafine cleaning, undesirable substance even the smallest dust particles from plastics, which at first adhere firmly to the surface because of the additives, can be completely removed from the surface, which create an optimal prerequisite for later coating. As can be seen in **Figure 3.3(c)** and **(d)**, film fabrications using plasma treated glass substrates show obviously superior film quality, which is beneficial for subsequent processes.

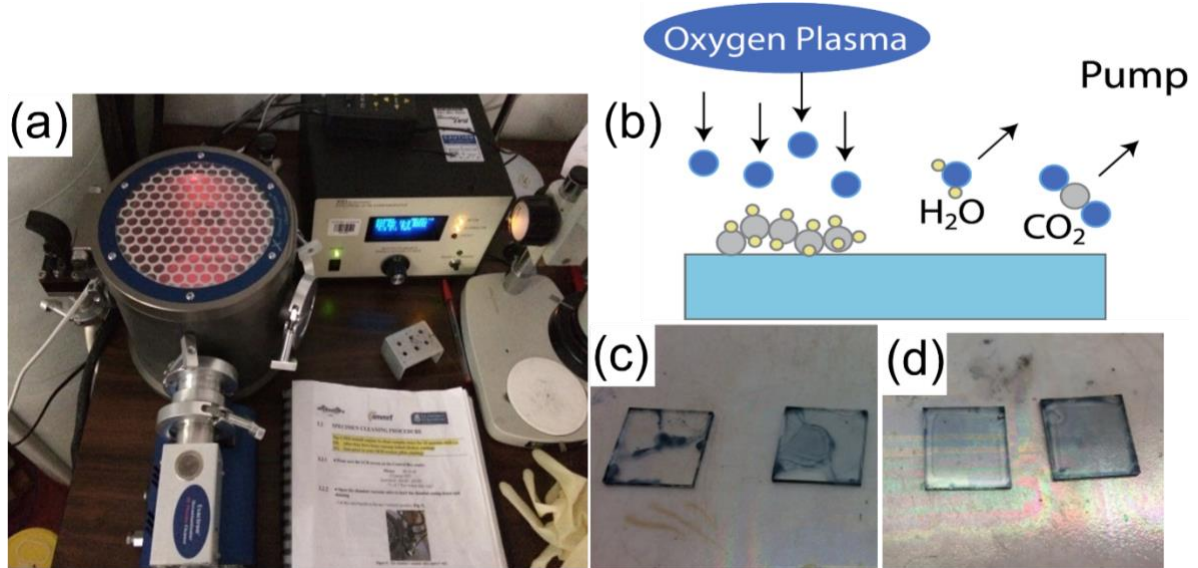


Figure 3.3 Principles and experimental photos of plasma treatment. (a) Laboratory equipment for plasma treatment. (b) Schematics of plasma treatment mechanism. (c) As-prepared PEDOT:PSS films on glass substrates without plasma treatment (d) As-prepared PEDOT:PSS films on glass substrates with plasma treatment.

3.2.2 Spin coating

Spin coating is a procedure used to deposit uniform thin films on flat substrates. As shown in **Figure 3.4(a)**, a small amount of coating ink is dropped on the centre of the substrate, which is either spinning at low speed or not spinning at all. The substrate is then rotated at high speed in order to spread the coating material by centrifugal force. **Figure 3.4(b)** is the laboratory spin coater used in this project.

During the spinning process, key parameters include spinning speed, spinning time and the amount of solution dropped on substrate once. Appropriate parameters should be determined according to properties of different polymers, such as viscosity and density, in order to obtain fine and uniform thin film. As for PEDOT:PSS in this project, optimized spinning route is 200 r min⁻¹ for 30 s. **Figure 3.4(c)** shows as-prepared films with different spinning parameters from

left to right. It can be found that our optimized spinning parameters are able to fabricate high-quality, uniform and transparent films.

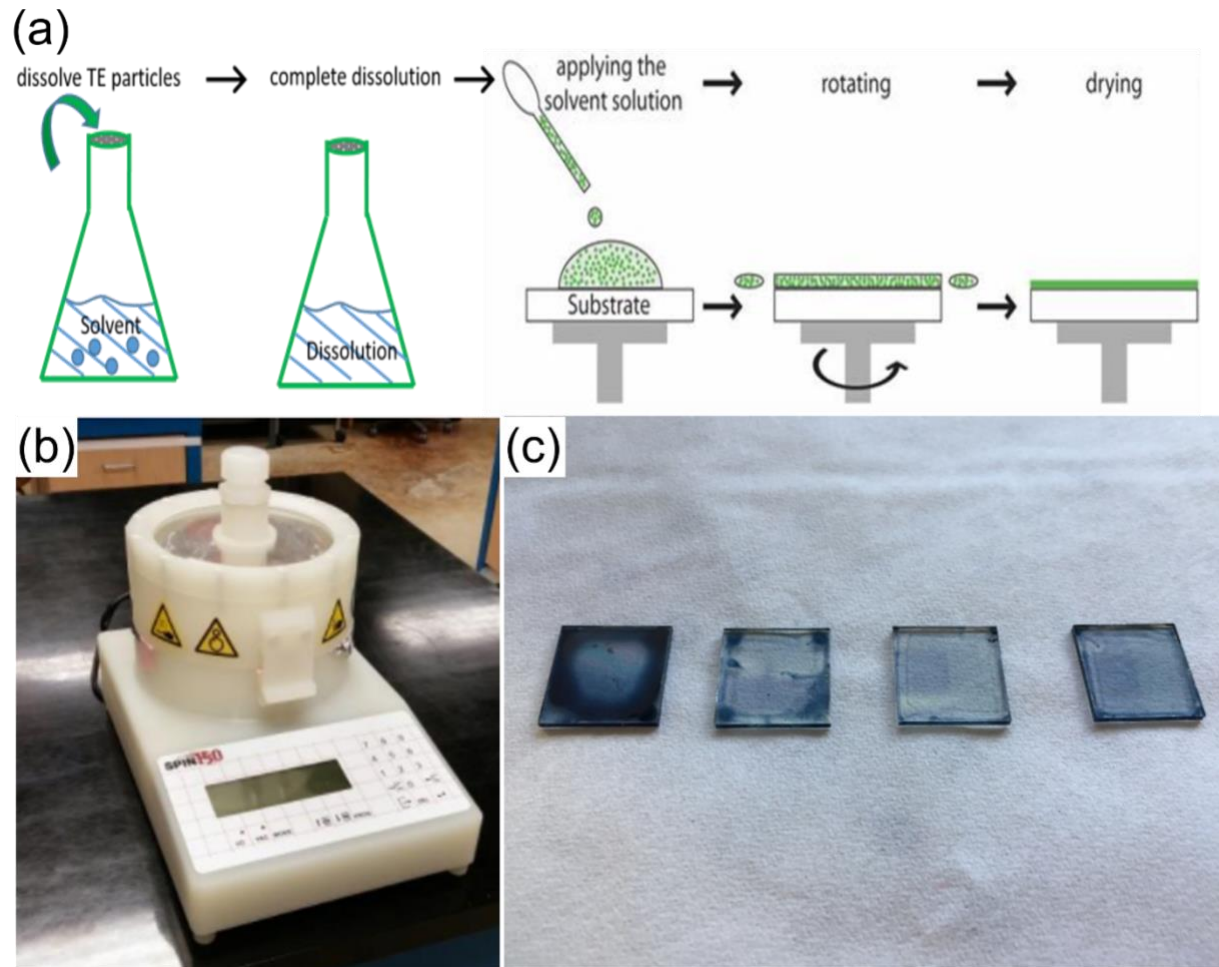


Figure 3.4 Principles and experimental photos of spin coating. (a) Schematics of spin coating process. (b) Laboratory spin coater. (c) As-prepared PEDOT:PSS films with different spinning parameters.

3.3 Characterization methods

3.3.1 X-Ray Diffraction (XRD)

XRD serves as one of the most accurate method to identify the chemical composition and crystal structures of as-prepared pellets and films. **Figure 3.5(a)** schematically shows the mechanisms of XRD, where high energy electron beams firstly bombard the metal target to emit X-ray with the wavelength in the range of 0.006 to 2 nm. X-ray can then penetrate the sample and get diffracted by sample crystal structures, forming diffraction peaks which are collected and subsequently used to identify the crystal information. The diffraction of X-ray follows Bragg's law:

$$2d \sin \theta = n\lambda \quad (3-1)$$

where θ is the incident angle, λ is the wavelength of X-ray, d is the inter-planar spacing and n is an arbitrary integer.

The working principle and typical framework of XRD are shown in **Figure 3.5(b)**. Basically, X-rays are ejected to the surface of sample with proper angles and generate corresponding diffraction patterns, which are collected by the signal detector on the other side. Collected signals are processed and further form the diffraction spectrum. Since the wavelength of X-rays from one machine is identical, d can be calculated accordingly based on above Bragg's law.

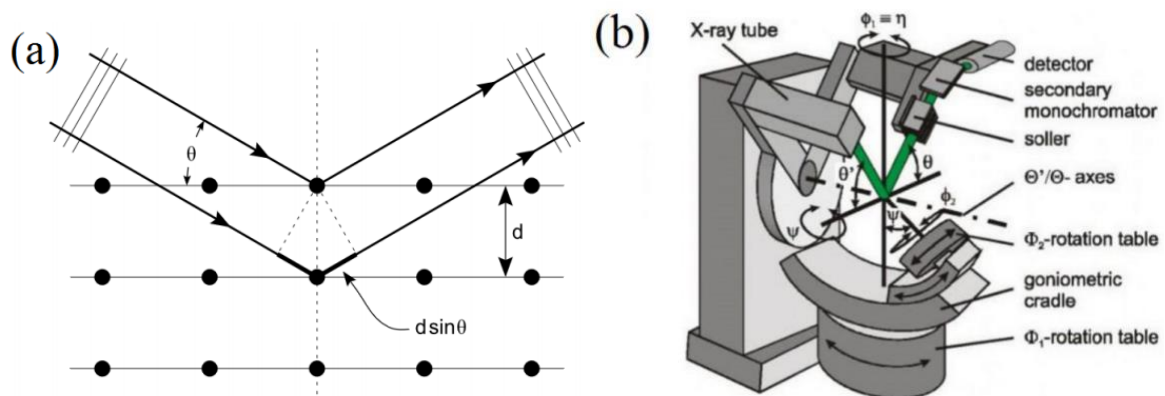


Figure 3.5 Schematic diagrams of (a) XRD mechanisms, (b) working principles and typical framework.

3.3.2 Scanning Electron Microscopy (SEM)

SEM serves as one powerful method to observe the morphology of sample surfaces. The working mechanism is schematically depicted in **Figure 3.6(a)**. Basically, a focused electron beam are emitted by the electron gun to scan the surface of samples, generating interaction volume and corresponding signals reflecting the morphological information. Such information are later processed and ultimately form the SEM image. It should be noted that interaction volume are associated with the energy of electron beams and the mean atomic numbers of the sample, where the former can be modulated by electron accelerating voltage in the practical operations.

Figure 3.6(b) shows the typical framework of one SEM. During the emission of electron beams, they are firstly accederalted by the anode with a certain voltage (1-50 kV) and then go through the condense lens. With condense lens and also the spot size adjuster, directions and size (several nanometers diameter) of electron beams are modulated, in order to generate a proper probe current. Adjusted electron beams are subsequently fouced by objective lens, scanning the sample surface and retuning scattered electrons, which can be classified as secondary electrons (SE)

and backscattered electrons (BSE). They are both collected by corresponding detectors and finally produce SE and BSE images, respectively.

Figure 3.6(c) and **(d)** explain the different mechanisms to generate SE and BSE. Specifically, SE is generated by inelastic collisions between incidence electrons and sample atomic electron cloud, which presents the low energy below 50 kV. Considering such a low energy, the interaction volume of SE is small and therefore SE mainly reflects the surface information of sample. The detection thickness of SE is normally 5 to 50 nm below the sample surface. More interior information of the specimen can be contributed by BSE. As shown in **Figure 3.6(d)**, BSE is high-energy electrons which can penetrate sample surfaces generating relatively large interaction volume. Different from SE, BSE is back-scattered electrons from elastic collisions between incidence electrons and sample atomic electron cloud, which can reflect the differences of sample atomic numbers. Specifically, sample atoms with smaller atomic numbers (lighter) can backscatter weaker electrons and therefore produce weaker BSE, while sample atoms with larger atomic numbers (heavier) can backscatter stronger electrons and therefore produce stronger BSE. Such a contrast can be applied to identify the changes of sample chemical compositions.

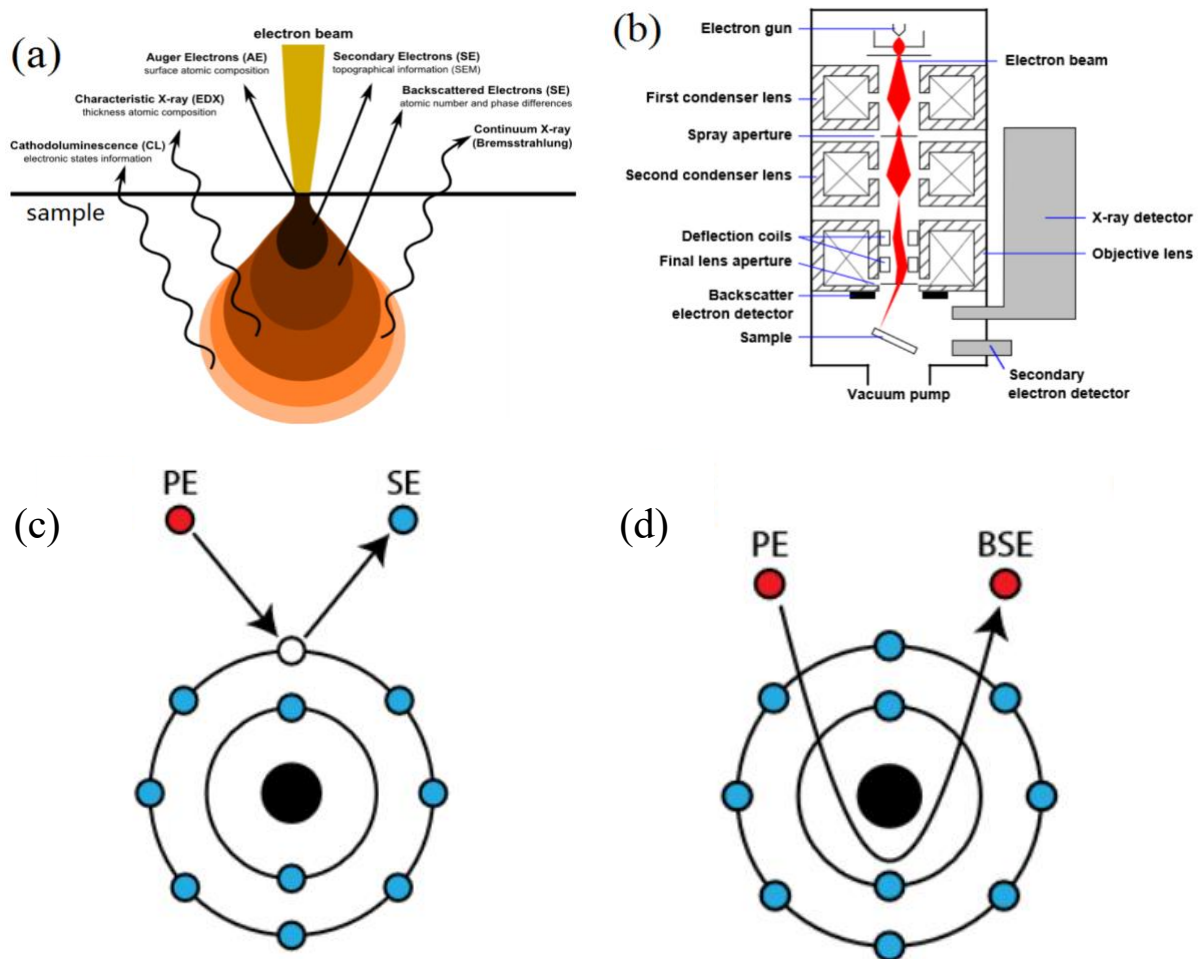


Figure 3.6 Introduction of SEM including schematics diagrams of (a) working mechanism, (b) typical framework, (c) generations of secondary electrons and (d) backscattered secondary electrons.

3.4 Properties measurements

Measurements towards thermoelectric properties of as-fabricated pellets and thin film can be achieved by utilizing SBA 458 Nemesis (NETZSCH) and laser flash (LFA 457, NETZSCH). Among which, SBA 458 is designed for Seebeck coefficient and electrical conductivity measurements, while LFA 457 is for thermal conductivity. In this section, their mechanisms are demonstrated.

3.4.1 Electrical properties

Electrical properties of thermoelectric materials include Seebeck coefficient (S) and electrical conductivity (σ). Mechanisms of their measurements using SBA458 are depicted in **Figure 3.7(a)**.

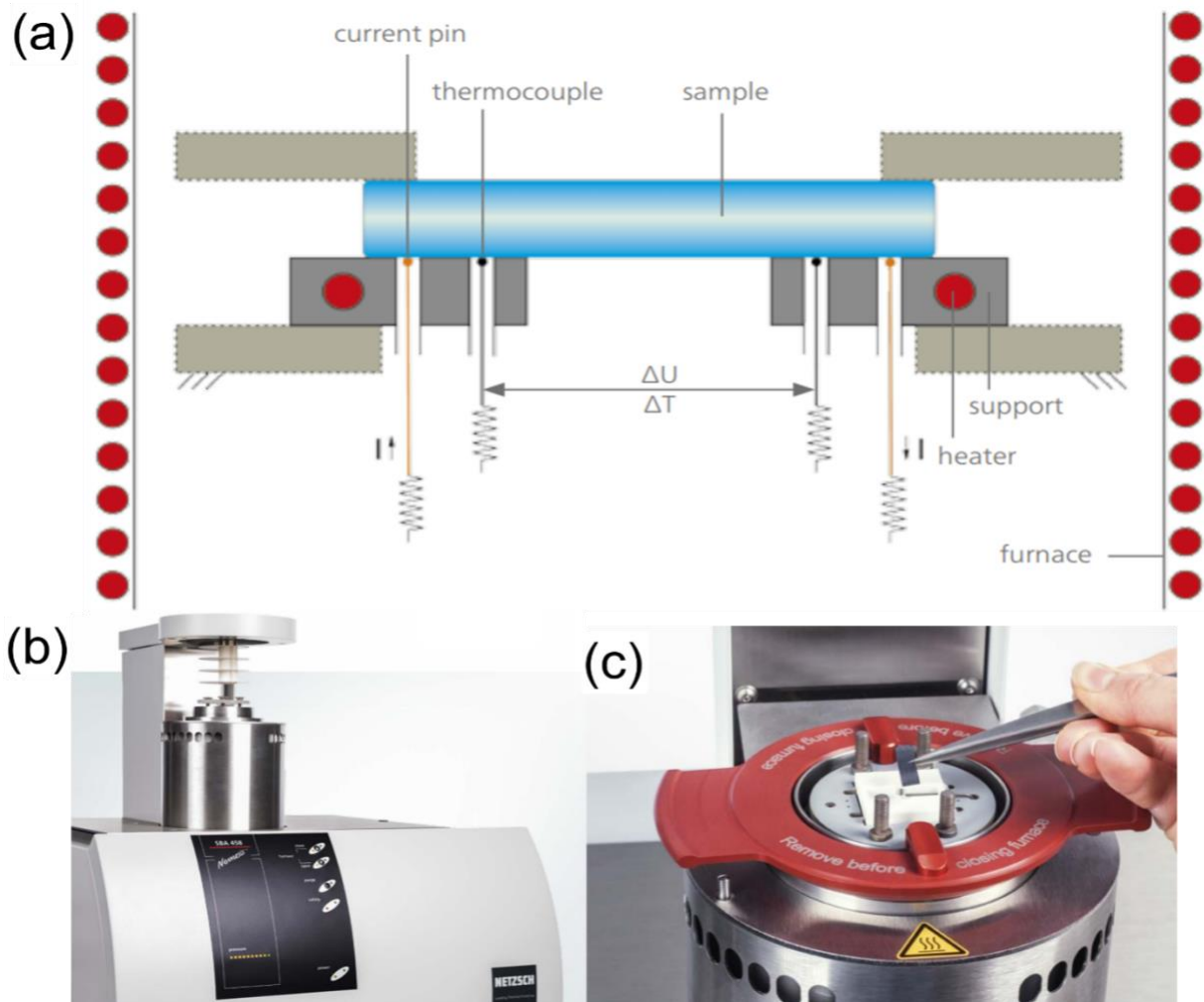


Figure 3.7 Schematic illustration of SBA458 working mechanism and photos of laboratory equipment. (a) Schematic of working mechanism in SBA 458. (b) Non-loaded SBA 458 in the laboratory. (c) Loaded SBA 458 in the laboratory.

Figure 3.7(b) and **(c)** show the photo of laboratory SBA458 and the method to load the sample. During the measurement of Seebeck coefficient, a temperature gradient is generated in both sample directions by two micro heaters operating in alternation. While the cyclic heating is in progress, the resulting voltages between the two thermocouple wires are measured. At the same time, ΔT is determined by two thermocouples. The resulting large number of measuring points is the basis for calculation of a regression line. From the slope of the regression line, the Seebeck coefficient can be precisely determined according to its definition:

$$S = \frac{\Delta V}{\Delta T} \quad (3-2)$$

During the measurement of electrical conductivity, at each testing temperature, different current values will be applied to the sample several times by current pins. These values will be

applied in both sample directions and the resulting voltages will be measured. This process yields a large number of measurement points between voltage and current, allowing for the calculation of electrical resistivity R of the sample. Then electrical conductivity can be obtained:

$$\sigma = \frac{1}{R} \quad (3-3)$$

As a result, electrical properties of sample are successfully measured and desired power factor PF can be calculated as below:

$$PF = S^2 \sigma \quad (3-4)$$

3.4.2 Thermal Properties

Thermal conductivity κ is defined as:

$$\kappa = D \times \rho \times C_p \quad (3-5)$$

where D , ρ , C_p is thermal diffusivity, density and specific heat capacity respectively. Density of sample can be easily calculated by measuring sample weight and volume. Heat capacity is always used as known result by formers. Therefore, the key point for thermal conductivity lies in the thermal diffusivity, which can be measured by LFA 457.

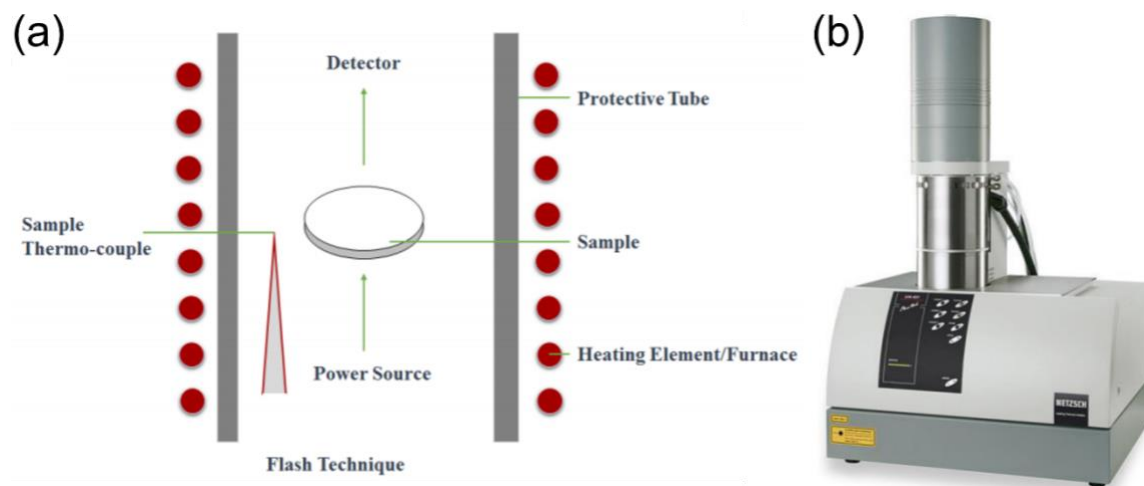


Figure 3.8 Schematic illustration of LFA 457 working mechanism and photos of laboratory equipment. (a) Schematic of working mechanism in SBA 458. (b) LFA 457 in the laboratory.

The principle of laser flash method and corresponding laboratory equipment can be seen from **Figure 3.8(a)** and **(b)**. The lower surface of sample is first heated by a short energy pulse (laser). After thermal diffuses through out of plane direction, the temperature on the upper surface will change and be measured by an infrared detector. Then sample thermal diffusivity can be calculated with:

$$D = 0.1388 \frac{d^2}{t_{\frac{1}{2}}} \quad (3-6)$$

where d is sample thickness and $t_{\frac{1}{2}}$ is time value at half signal height.

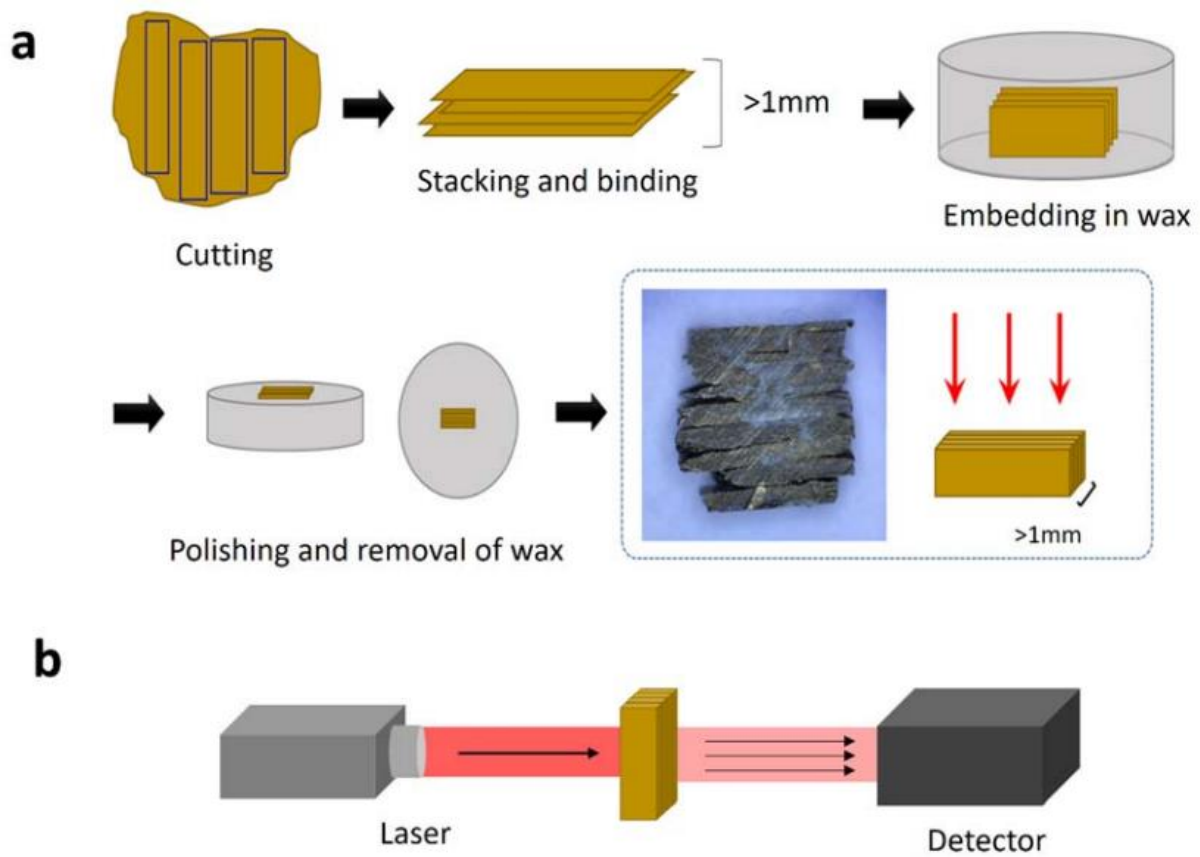


Figure 3.9 Sample preparation for the in-plane thermal diffusivity measurement by the laser flash method. (a) The thin sample was first cut into many small pieces and then stacked and bonded using epoxy resin. It was then put into melted wax and solidified. Both sides of the sample were polished using a sand paper. The wax was removed by heating and then washing in ethyl ether. (b) Thermal diffusivity of the prepared sample was measured by a standard laser flash analysis equipment.

It is noticeable that thermal diffusivity in above case is in out of plane direction. However, electrical properties obtained from SBA 458 are in in-plane direction. In some systems where material anisotropy cannot be neglected, in-plane direction thermal diffusivity is necessary to calculate the correct zT . For thermoelectric pellets, the measurement sample can be facily prepared by sintering chunks, followed by cutting chunks along the sintering pressure direction. As for thermoelectric films, we attempt to solve this problem by cutting, stacking and binding film pieces into thicker sample (more than 1mm) and then measure in-plane thermal properties. Detailed schematic is shown in **Figure 3.9**. Wax is utilized here in order to solidify stacked

film pieces. This is because thermal diffusivity of wax is quite different from the value of our sample, therefore it is convinced that temperature detected by infrared detector mostly come from sample or wax is “invisible” to the detector. In this way, in-plane thermal diffusivity of thin film may be measured.

Chapter 4 Enhanced Thermoelectric Properties of Nanostructured *n*-Type Bi₂Te₃ by Suppressing Te Vacancy through Non-equilibrium Fast Reaction

4.1 Overview

Bi₂Te₃ as one of the best low-temperature thermoelectric materials hold full potentials to power wearable electronics within the low temperature range. However, its energy conversion efficiency (zT) is restrained by excessive carrier concentrations beyond the predicted optimal value. Te vacancies as the predominant intrinsic point defects in *n*-type Bi₂Te₃ can solely contribute plenty of carrier concentrations. Suppression of Te vacancies in *n*-type Bi₂Te₃ is of great significance to dampen the carrier concentration and in turn push zT to a higher level. Moreover, nanostructured thermoelectric materials have been widely appreciated for its low lattice thermal conductivity, which is beneficial to achieve improved zT . Therefore, the realization of Te vacancies suppression in nanostructured Bi₂Te₃ could serve as one promising strategy to boost zT of Bi₂Te₃ thermoelectric materials.

Within our study, the effective suppression of Te vacancies is achieved in nanostructured *n*-type Bi₂Te₃ *via* a non-equilibrium fast reaction with facile fabrication methods. The carrier concentration has been greatly reduced from pristine $\sim 1 \times 10^{20}$ to $\sim 6 \times 10^{19}$ cm⁻³, generating a decent power factor of 12.84 μ W cm⁻¹ K⁻² at 320 K. Meanwhile, the decreased electron thermal conductivity due to deteriorated electrical conductivity, enables a very low thermal conductivity of 0.48 W m⁻¹ K⁻¹, which ultimately secures a promising peak figure of merit zT of ~ 1.1 at 420 K and an extraordinary average zT of ~ 1 from 320 to 470 K. Such a high performance is one of the cutting-edge binary *n*-type Bi₂Te₃ reported so far.

4.2 Journal publication

The journal publication included in **Chapter 4** is available at *Chem. Eng. J.* **2019**.
<https://doi.org/10.1016/j.cej.2019.123513>.

Enhanced Thermoelectric Properties of Nanostructured *n*-Type Bi₂Te₃ by Suppressing Te Vacancy through Non-equilibrium Fast Reaction

Yuan Wang^{a,b}, Wei-Di Liu^b, Xiao-Lei Shi^{a,b}, Min Hong^{a,b}, Li-Jun Wang^b, Meng Li^b, Hao Wang^a, Jin Zou^{b,c}, Zhi-Gang Chen^{a,b}*

^aCentre for Future Materials, University of Southern Queensland, Springfield central, Queensland 4300, Australia.

^bMaterials Engineering, The University of Queensland, Brisbane, Queensland 4072, Australia.

^cCentre for Microscopy and Microanalysis, The University of Queensland, Brisbane, Queensland 4072, Australia

*Corresponding author. Email: zhigang.chen@usq.edu.au (ZGC); zhigang.chen@uq.edu.au (ZGC)

Abstract

As one promising low-temperature thermoelectric material, Bi₂Te₃ suffers from high carrier concentrations beyond the optimal value contributed by excess Te vacancies. In this study, Te vacancies can be effectively suppressed in the *n*-type nanostructured Bi₂Te₃ *via* a non-equilibrium reaction induced by spark plasma sintering. The electron concentration has been greatly reduced from pristinely $\sim 1 \times 10^{20}$ to $\sim 6 \times 10^{19}$ cm⁻³, generating a decent power factor of 12.84 $\mu\text{W cm}^{-1} \text{K}^{-2}$ at 320 K. Meanwhile, the decreased electronic thermal conductivity due to deteriorated electrical conductivity enables a very low thermal conductivity of 0.48 W m⁻¹ K⁻¹, which ultimately secures a promising peak figure of merit zT of ~ 1.1 at 420 K and an outstanding average zT of ~ 1 from 320 to 470 K. Such a high performance is one of the cutting-edge values reported in binary *n*-type Bi₂Te₃ so far. Our study provides a new insight into manipulating intrinsic point defects in nanostructured Bi₂Te₃ thermoelectric materials for achieving higher zT .

Keywords: Thermoelectrics, Bismuth telluride, Te vacancy, Nanostructure

1. Introduction

Thermoelectric materials enable the direct conversion between heat and electricity, which act as environmentally friendly alternatives for sustainable power generations.^{5,24,159} The efficiency of thermoelectric materials is gauged by a dimensionless figure of merit (zT), which is defined as: $zT = S_2\sigma T/\kappa = S_2\sigma T/(\kappa_e + \kappa_l)$, where S , σ , κ , κ_e , κ_l , and T are the Seebeck coefficient, electrical conductivity, total thermal conductivity, electrical thermal conductivity, lattice thermal conductivity, and the absolute temperature, respectively.^{18,160,161} In order to obtain high zT , thermoelectric parameters including σ , S and κ_e need to be synergistically considered, as they are strongly interdependent and coupled by the carrier concentration (n).^{148,162,163} In this vein, modulating of n towards the optimal value is paramount in terms of developing promising thermoelectric materials. Currently, strategies to modulate n mainly include doping engineering,^{15,149,164} and point defect engineering, where vacancies,^{165,166} antisite defects^{65,167} and donor-like effects^{65,85,168} are engineered.

Bismuth telluride (Bi_2Te_3) is one of the best low-temperature thermoelectric materials with intrinsically decent σ and S , due to its narrow band gap (~ 0.15 eV) with high valley degeneracy and anisotropic effective mass.⁴⁴ A superior $S_2\sigma$ of $\sim 12 \mu\text{W cm}^{-1} \text{K}^{-2}$ was reported previously from pristine n -type Bi_2Te_3 without any doping.^{37,38} In order to further improve $S_2\sigma$, optimal electron concentration (n_e) was predicted to be $\sim 1 \times 10^{19} \text{ cm}^{-3}$ for n -type Bi_2Te_3 .⁹⁴ However, due to the competition between internal energy and entropy during the Bi_2Te_3 crystal growth,⁴⁸ the intrinsic point defects alone, which is predominately Te vacancies ($V_{\text{Te}}^{\bullet\bullet}$) for n -type Bi_2Te_3 ,^{169,170} can contribute n_e of 10^{18} - 10^{20} cm^{-3} .¹⁶⁶ Therefore, $V_{\text{Te}}^{\bullet\bullet}$ has to be suppressed in order to approach the optimal n_e . Previously, substituting anion sites with more electronegative or smaller atoms of the same valance, which is so called isoelectron extrinsic doping, was reported to be one effective strategy to suppress $V_{\text{Te}}^{\bullet\bullet}$ in the n -type Bi_2Te_3 , as it may increase the formation energy of $V_{\text{Te}}^{\bullet\bullet}$.⁷⁹ One typical example is Te substitution by Se in the $\text{Bi}_2\text{Te}_{2.3}\text{Se}_{0.7}$ alloy, where room temperature n_e was effectively reduced from $\sim 1 \times 10^{20} \text{ cm}^{-3}$ to $\sim 7 \times 10^{19} \text{ cm}^{-3}$ with record zT of 1.2 ultimately achieved at 445 K.⁶⁵ Moreover, post-deformation thermal relaxation processes, such as high temperature annealing,⁵⁴ high temperature hot pressing (HP)¹⁷¹ or spark plasma sintering (SPS),⁸⁵ were also found to suppress $V_{\text{Te}}^{\bullet\bullet}$, as they can mitigate the donor-like effect.⁷⁹ For example, Zhao et al. realized the reduction of n_e from $7.5 \times 10^{19} \text{ cm}^{-3}$ to $6 \times 10^{18} \text{ cm}^{-3}$ by raising SPS temperature of n -type Bi_2Te_3 from 623 K to 673 K, which consequently caused boosted $S_2\sigma$ from $15 \mu\text{W cm}^{-1} \text{K}^{-2}$ to $21 \mu\text{W cm}^{-1} \text{K}^{-2}$ at 420 K.⁸⁵ Apart from these, off-stoichiometry design of starting materials is also one potential strategy to dampen $V_{\text{Te}}^{\bullet\bullet}$ and in

turn decrease n_e , as it was reported that excess Bi may facilitate the formation of antisite defect Bi'_{Te} in the n -type $\text{Bi}_{2+x}\text{Se}_3$ ingot.¹⁶⁹ In spite of these progresses, previous efforts to suppress $V_{\text{Te}}^{\bullet\bullet}$ of n -type Bi_2Te_3 mainly focus on alloys with micro-scale grains. The suppression of $V_{\text{Te}}^{\bullet\bullet}$ in nanostructured n -type Bi_2Te_3 is rarely reported, whose low κ_l can potentially lead higher zT .^{38,172}

Herein, we reported the suppression of $V_{\text{Te}}^{\bullet\bullet}$ in nanostructured n -type Bi_2Te_3 *via* a non-equilibrium reaction induced by SPS. The schematic of experiment is depicted in **Figure 1**, where Cr_2TeO_6 and Bi_2Te_3 were firstly synthesized from the solvothermal synthesis, and then triggered to conduct a non-equilibrium reaction^{162,173} under the large plasma currents and heating environment of SPS. As a result, $V_{\text{Te}}^{\bullet\bullet}$ was compensated during the reaction, and n_e was effectively reduced from $\sim 1 \times 10^{20} \text{ cm}^{-3}$ to $\sim 6 \times 10^{19} \text{ cm}^{-3}$. Enhanced zT from 0.7 to 1.08 was achieved at 470 K, with high average zT close to 1 from 300 K to 470 K, which is one of the highest values reported for binary n -type Bi_2Te_3 so far.^{37,85,174-176} Our study might provide a new perspective for the manipulation of intrinsic point defects in Bi_2Te_3 thermoelectric materials.

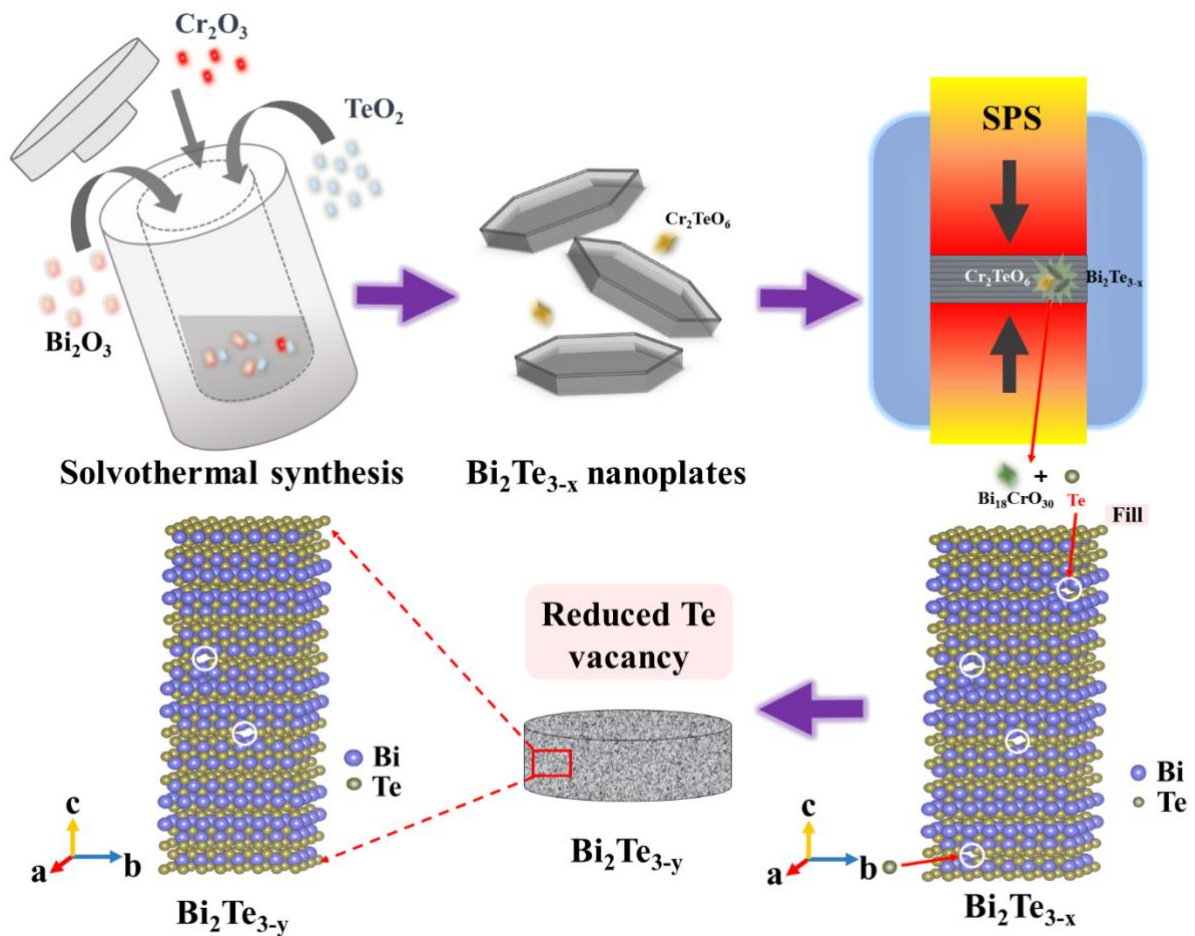


Figure 1. Illustration of the fabrication processes, where a non-equilibrium reaction occurred during the spark plasma sintering, leading the fabrication of nanostructured Bi₂Te₃ pellet with suppressed Te vacancies.

Experimental Section

Synthesis Method

Bi₂Te₃ nanoplates were synthesized *via* a typical solvothermal route. Analytical grade bismuth oxide (Bi₂O₃, 99.9%), tellurium dioxide (TeO₂, 99.999%), chromium oxide (Cr₂O₃, 99.999%), ethylene glycol (EG), polyvinylpyrrolidone (PVP, average molecular weight = 40000) and sodium hydroxide (NaOH, 99.99%) were purchased from Sigma-Aldrich as precursors without any further purification. During the synthesis, PVP was firstly dissolved into EG (36 ml) as the surfactant, followed by 20 min vigorous stirring in order to form a clear solution. Bi₂O₃ and TeO₂ were then added into the solution as the source materials of Bi and Te, respectively. The solutions were subsequently mixed with various amount of Cr₂O₃ (0.76 mg, 1.52 mg and 3.04 mg), followed by dropping 4 ml 5 mol L⁻¹ NaOH to provide the alkaline environment. Pristine Bi₂Te₃ was also prepared based on aforementioned procedures without the addition of Cr₂O₃. The solutions were stirred for 30 min to uniformly mix precursors, before sealed in a 125 ml polytetrafluoroethylene-lined stainless-steel autoclave. The autoclaves were heated to 210 °C for 24 h and naturally cooled down to the room temperature. Synthesized powders were separately collected and washed with deionized water and ethanol for several times by centrifugation, and finally dried in the oven at 60 °C for 12 h.

Spark Plasma Sintering and Thermoelectric Properties Measurements

In order to measure the thermoelectric properties, synthesized powders were sintered into a disc-shaped pellets ($\Phi = 12.6$ mm) by SPS (SPS-211Lx, Fuji Electronic Co., Ltd.) at 300 °C for 5 min under 60 MPa pressure. Densities (ρ) of different pellets were measured using the Archimedes method. Due to the intrinsic anisotropy of Bi₂Te₃,³⁰⁻³² thermoelectric properties of the pellets were measured in the in-plane direction, which is the high-performance direction.³² Among which, σ and S were measured simultaneously using ZEM3 (ULVAC Technologies, Inc.) within the temperature range between 300 and 570 K; the thermal diffusivity D was measured by LFA 457 (NETZSCH Group), which was subsequently applied to calculate $\kappa = D \cdot C_p \cdot \rho$,³³ where C_p is the specific heat capacity measured by DSC 404 C (NETZSCH Group); n and μ were measured by a Hall system under a reversible magnetic field of 1.5 T. All property

measurements of the pellet were conducted for at least three times in order to ensure the repeatability.

Characterization

Both synthesized powders and sintered pellets were systematically characterized. X-ray diffraction (XRD, Bruker-D8) was applied to determine the compositions and crystal structure of both prepared powders and pellets, where the pellet was characterized along the in-plane direction. Lattice parameters (a and c) of both powders and pellets were then calculated based on Bragg's law, and corresponding unit cell volumes were calculated according to determined Bi_2Te_3 crystal structure. Scanning Electron Microscope (SEM, JEOL JSM-7100F) and Transmission electron microscope (TEM, TECNAI-F20) were utilized to observe the morphology and structural characteristics. The TEM specimens of sintered pellets were prepared using an Ultramicrotome. Energy-dispersive X-ray spectroscopy (EDS) mapping and spot analysis (equipped in HITACHI-SU3500 SEM) were conducted to investigate the element distribution and $V_{\text{Te}}^{\text{II}}$ of the samples. In order to intuitively reflect the change of $V_{\text{Te}}^{\text{II}}$, pellets were labelled in the form of $\text{Bi}_2\text{Te}_{3-x}$, where x was determined by EDS spot analysis as 0.26, 0.23, 0.20 and 0.14 for Cr_2O_3 addition of 0 mg, 0.76 mg, 1.52 mg and 3.04 mg, respectively.

Results and Discussion

Figure 2a shows the XRD patterns of as-sintered pellets in the direction perpendicular to the sintering pressure. As can be seen, for the pristine $x = 0.26$ pellet ($\text{Bi}_2\text{Te}_{2.74}$), its diffraction patterns can be exclusively indexed as the rhombohedral structured Bi_2Te_3 with the lattice parameters of $a = 4.36518$ nm, $c = 30.39482$ nm and a space group of $R\bar{3}m$ (PDF#15-0863). However, for $x = 0.23$ ($\text{Bi}_2\text{Te}_{2.77}$), $x = 0.20$ ($\text{Bi}_2\text{Te}_{2.80}$) and $x = 0.14$ ($\text{Bi}_2\text{Te}_{2.86}$) pellets, although rhombohedral structured Bi_2Te_3 is still detected, the peaks of $\text{Bi}_{18}\text{CrO}_{30}$ (PDF#24-0303) emerge (highlighted with the red arrows), and they tend to exhibit higher intensities with smaller x . This is in contrast with as-synthesized powders, where no peaks of $\text{Bi}_{18}\text{CrO}_{30}$ are detected, as shown in the supporting information, indicating $\text{Bi}_{18}\text{CrO}_{30}$ should be generated *via* a non-equilibrium reaction during the SPS process.^{162,173} **Figure 2b** shows the magnified XRD patterns of (0 0 15) peak in different pellet samples. A obvious peak shift towards lower angles is observed, which hints the lattice expansion. This is ascribed to reduced $V_{\text{Te}}^{\text{II}}$ in the pellets. Lattice expansion is further manifested by the calculations of lattice constants and unit cell volumes, as shown in **Figure 2c**, where increased a and c are both obtained, and in turn lead

higher unit cell volumes. Detailed calculations of lattice constants and unit cell volumes are shown in the supporting information.

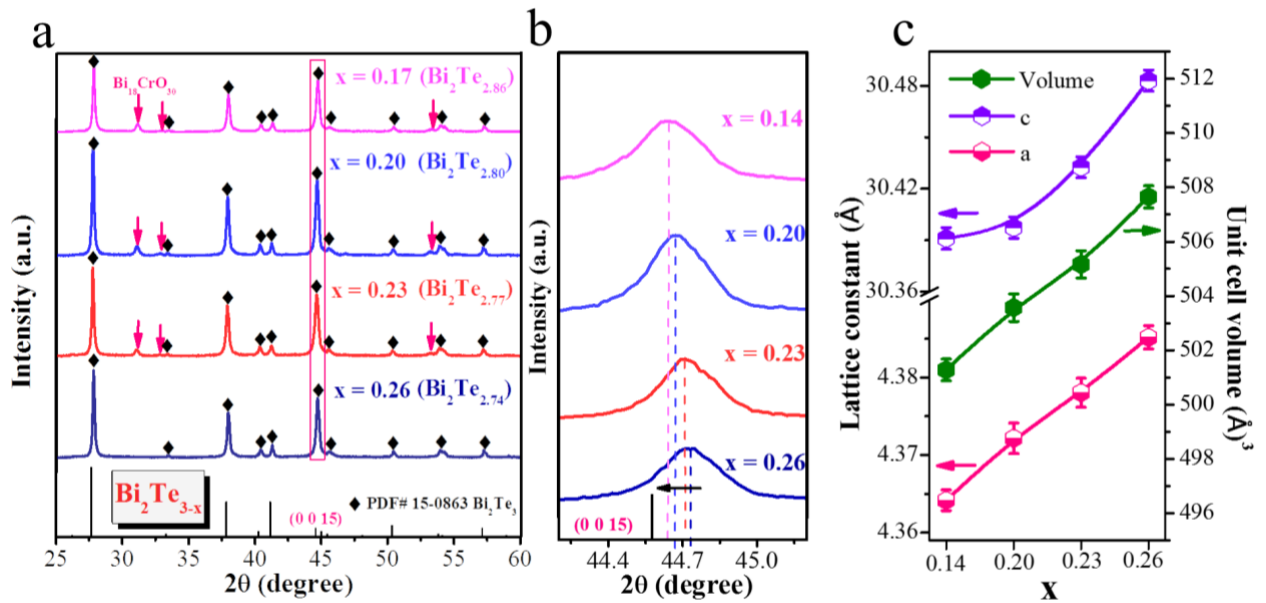


Figure 2. (a) XRD patterns of sintered $\text{Bi}_2\text{Te}_{3-x}$ pellets with different Te vacancies ($x = 0.26, 0.23, 0.20$ and 0.14); (b) magnified XRD patterns of 0015* peak to observe the peak shift; and (c) calculated lattice constants and unit cell volumes of sintered $\text{Bi}_2\text{Te}_{3-x}$ pellets.

Figure 3a shows the results of EDS spot analysis on the pellet samples. Lower $V_{\text{Te}}^{\text{vac}}$ is intuitively reflected by smaller x , which is consistent with aforementioned XRD results. Corresponding typical EDS point spectrums are shown in **Figure 3b**. Bi and Te are exclusively detected, and the atomic ratios between Te and Bi gradually increase, which indicate the suppression of $V_{\text{Te}}^{\text{vac}}$. **Figure 3c** are EDS mappings of Bi and Te in the $x = 0.14$ pellet, and the corresponding backscattered electron (BSE) SEM image. Uniform distributions of Bi and Te are observed without the element aggregation.

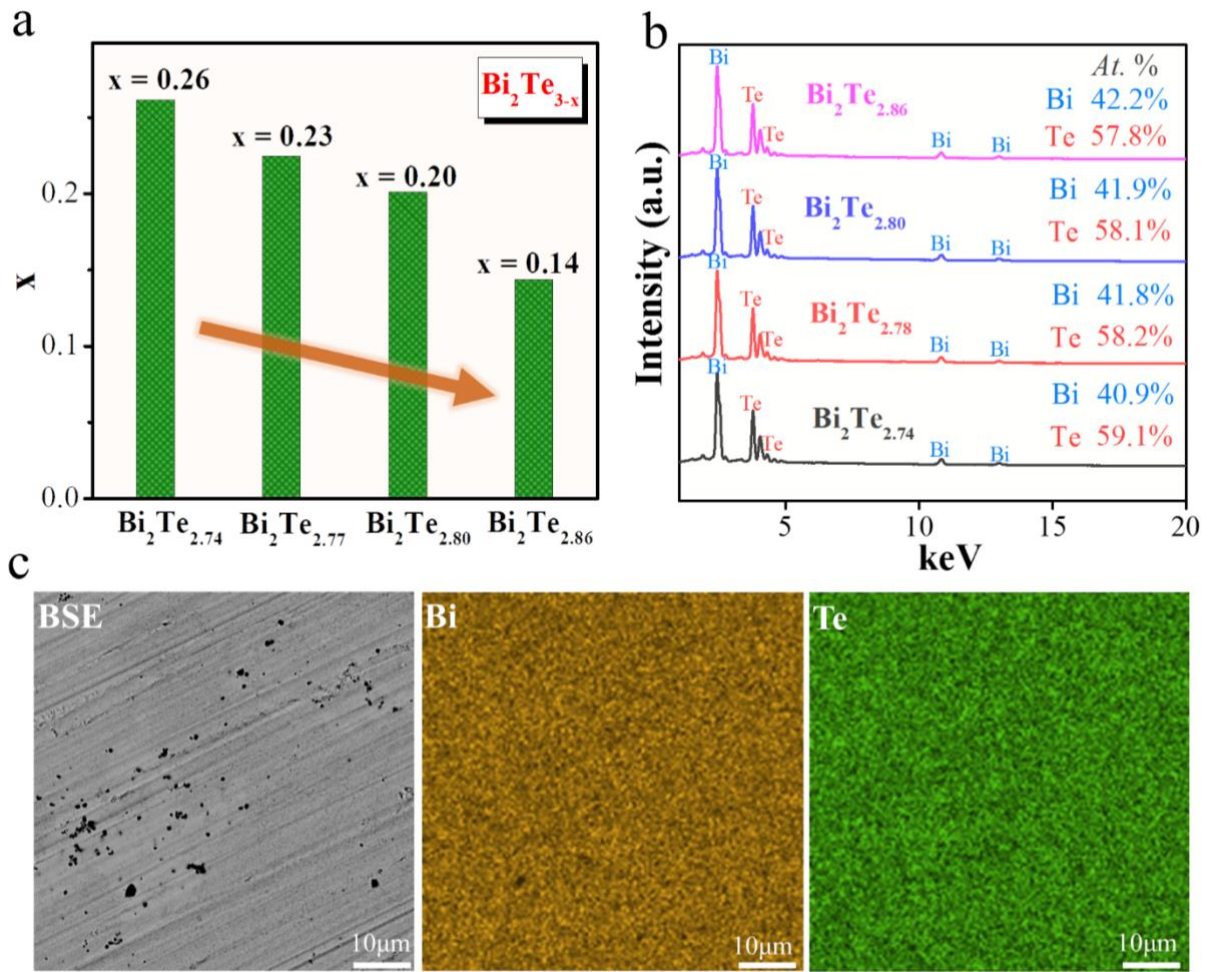


Figure 3. (a) Investigation of average Te vacancies in sintered Bi₂Te_{3-x} pellets by EDS spot analysis; (b) typical EDS spot spectrums of sintered Bi₂Te_{3-x} pellets; and (c) mapping results of Bi and Te in Bi₂Te_{2.86}.

Figure 4 shows measured electrical properties of the pellets in the direction perpendicular to the sintering pressure, including σ , S , n_e and $S_2\sigma$. As can be seen in **Figure 4a**, σ of different pellets tend to gradually decrease with higher temperature, which present typical metallic transport behaviours.¹⁷⁷ The peak σ of 844 S cm⁻¹ was achieved at 300 K in the pristine $x = 0.26$ pellet, which is also comparable to other reported nanostructured Bi₂Te₃.^{37,38} On the other hand, suppressed $V_{T_e}^{\ddot{}}$ compromises σ , leading higher σ of $x = 0.26$ pellet than $x = 0.14$ pellet in the whole temperature range from 300 K to 570 K. **Figure 4b** is S of different pellets, where negative values indicate typical n -type properties. S shows initial increase from 300 K to 450 K, and then slightly decrease. For semiconductors, S increases with elevated temperatures.⁴⁵ Our declined S is because of bipolar effects of Bi₂Te₃ due to its intrinsic narrow band gap, where minor carriers (holes) may be excited at high temperature and compensate the

contributions of major carriers (electrons).^{60,61} Reduced $V_{\text{Te}}^{\ddot{}}$ lead higher S , peak S of $141 \mu\text{V K}^{-1}$ is realized at 420 K from $x = 0.14$ pellet. In order to clarify the change of σ and S , n_e and carrier mobility (μ) were measured using Hall system. **Figure 4c** shows as-measured n_e . It can be found that lower $V_{\text{Te}}^{\ddot{}}$ can cause lower n_e at the whole temperature range, and n_e is effectively reduced from $\sim 1 \times 10^{20} \text{ cm}^{-3}$ in the $x=0.26$ pellet to $\sim 6 \times 10^{19} \text{ cm}^{-3}$ in the $x = 0.14$ pellet at 300 K. This is because one Te of n -type Bi_2Te_3 play the role of capturing two electrons.³⁸ With reduced $V_{\text{Te}}^{\ddot{}}$, more free electrons are captured and fail to participate into the carrier transport, which in turn lead lower n_e . As-measured carrier mobility (μ) is plotted in the supporting information, where no obvious change is observed. Since $\sigma = ne\mu$,^{150,178} where $e = 1.6 \times 10^{-19} \text{ C}$ is the electron charge constant, reduced n_e therefore can explain the decrease of σ . On the other hand, because S is negatively correlated with n_e ,^{145,179} lower n_e results in higher S . As-calculated $S_2\sigma$ is shown in **Figure 4d**, it can be found that reduced $V_{\text{Te}}^{\ddot{}}$ can effectively push $S_2\sigma$ to the higher level, and the highest $S_2\sigma$ of $12.84 \mu\text{W cm}^{-1} \text{ K}^{-2}$ was achieved in the $x = 0.2$ pellet at 320 K.

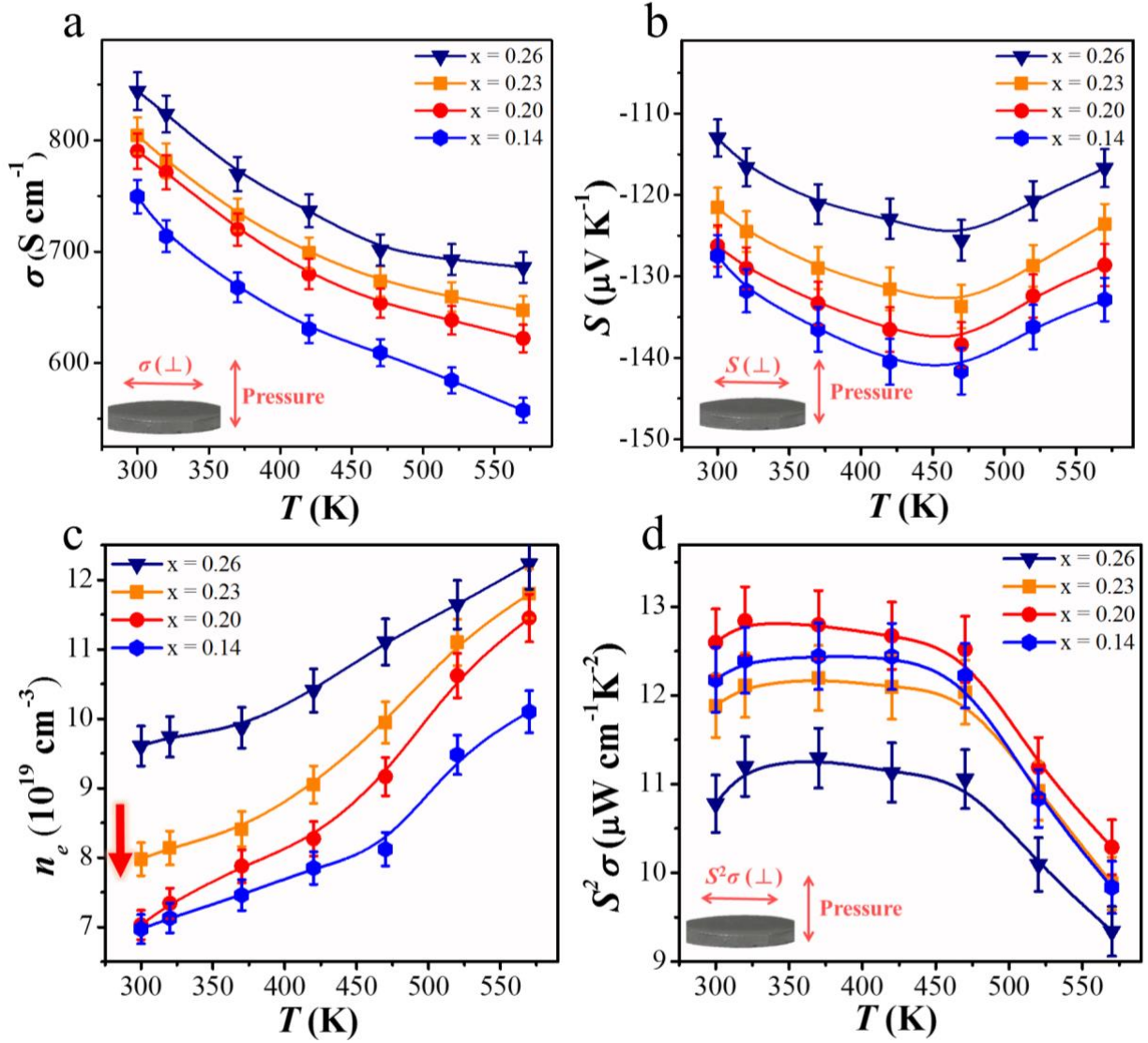


Figure 4. T -dependent (a) σ ; (b) S ; (c) n_e and (d) $S^2\sigma$ of sintered $\text{Bi}_2\text{Te}_{3-x}$ pellets in the direction perpendicular to the sintering pressure.

Figure 5a shows calculated κ of different pellet samples. Pristine $x = 0.26$ pellet presents the lowest κ of $\sim 0.5 \text{ W m}^{-1} \text{ K}^{-1}$ at 370 K, which is obviously lower than other reported Bi_2Te_3 alloys.^{31,96,180} This is ascribed to the dense grain boundaries in our nanostructure, as manifested by the SEM and TEM images in the supporting information. Such a value is also comparable to other reported nanostructured Bi_2Te_3 .^{37,38} Moreover, the reduction of $V_{\text{Te}}^{\text{II}}$ can further dampen κ . We investigated the underlying mechanism by calculating κ_l , as shown in the supporting information. It is found that different pellets show similar κ_l . Therefore, the reduction of κ mainly derives from κ_e . According to Wiedemann–Franz law,¹⁸¹ $\kappa_e = L\sigma T$, where L is the Lorenz number ($\sim 1.8 \times 10^{-8} \text{ v}_2 \text{ K}^{-2}$) and was calculated based on single parabolic band (SPB) model. Suppressed σ induced by lower $V_{\text{Te}}^{\text{II}}$ accounts for decreased κ_e , and in turn lower κ . The

final zT was calculated and shown in **Figure 5b**. The suppression of $V_{Te}^{\ddot{}}$ effectively improved zT , peak $zT \sim 1.1$ was achieved in $x = 0.14$ pellet at 420 K, which is among the highest zT reported so far for n -type binary Bi_2Te_3 .^{37,39,85,174-176,182} Furthermore, **Figure 5c** compared average zT of our work with other n -type binary Bi_2Te_3 works.^{37,85,174-176} Outstanding average $zT \sim 1$ was achieved from 300 K to 470 K, which is the highest value among others. Such a decent performance might be of interest for low-temperature wearable thermoelectric devices.⁹⁹ Above all, as shown in **Figure 5d**, zT of our work holds full potential to be further boosted with proper n_e ($\sim 1 \times 10^{19} \text{ cm}^{-3}$), which may guide our future work to manipulate intrinsic point defects.

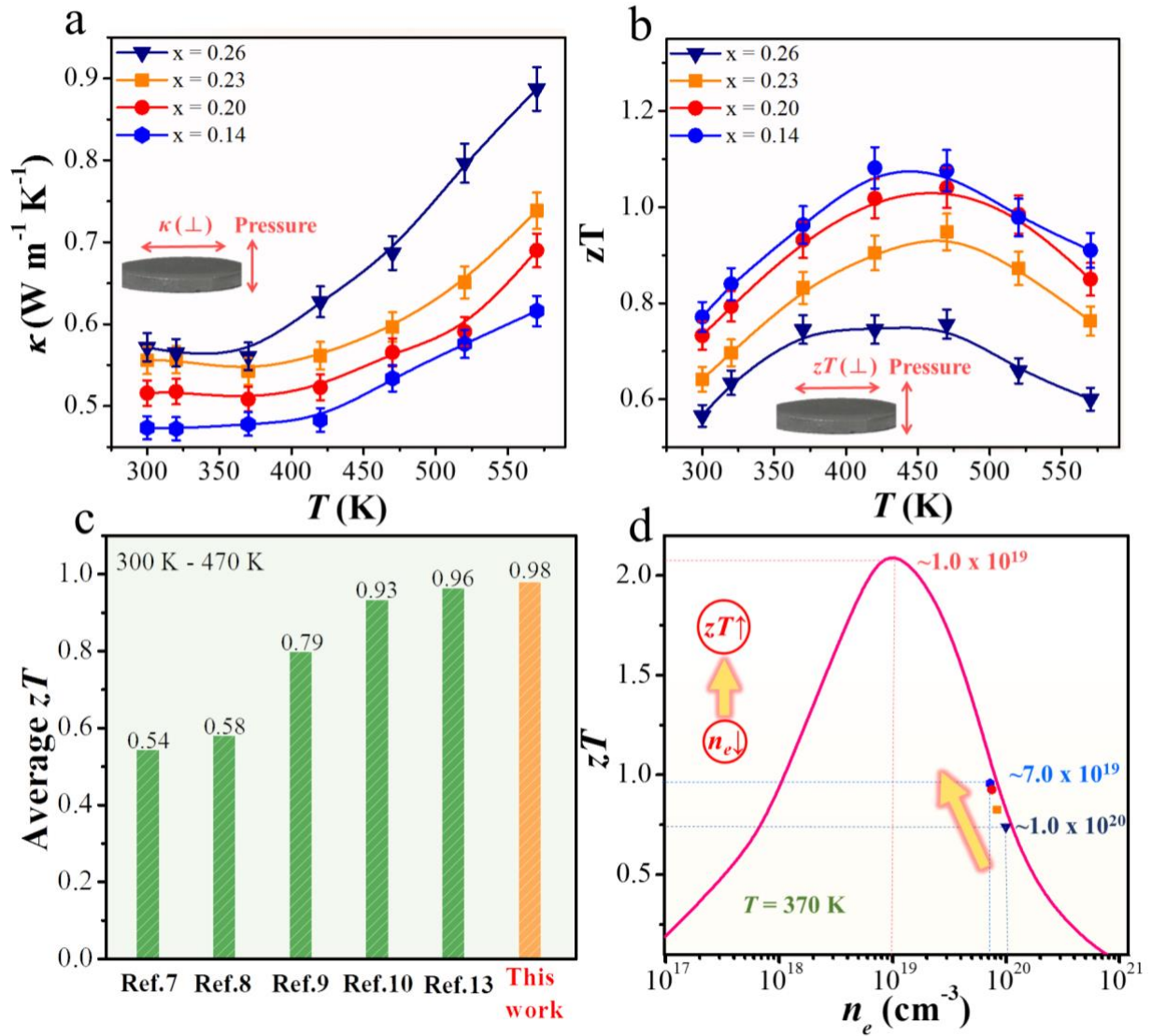


Figure 5. T -dependent (a) κ and (b) zT of sintered $\text{Bi}_2\text{Te}_{3-x}$ pellets. (c) A comprehensive comparison of average zT between this work and other state-of-art binary n -type Bi_2Te_3 works.^{37,85,174-176} (d) Calculation results of SPB model showing the effective zT enhancements with reduced n_e .

Conclusions

In this study, we realized the suppression of $V_{\text{Te}}^{\ddot{}}$ in the *n*-type nanostructured Bi_2Te_3 pellet *via* a non-equilibrium reaction induced by SPS. XRD and EDS results confirmed the reduction of $V_{\text{Te}}^{\ddot{}}$, and n_e was found to decrease from $\sim 1 \times 10^{20} \text{ cm}^{-3}$ to $\sim 6 \times 10^{19} \text{ cm}^{-3}$, which induced lower σ and increased S . Optimized $S_2\sigma$ of $12.84 \mu\text{W cm}^{-1} \text{ K}^{-2}$ was achieved at 320 K. With κ_l remained, decreased κ_e from lower σ further dampened κ as low as $0.48 \text{ W m}^{-1} \text{ K}^{-1}$, which consequently secured a promising $zT \sim 1.1$ at 420 K and outstanding average $zT \sim 1$ from 300 K to 470 K, which is one of the highest values report for binary *n*-type Bi_2Te_3 .^{37,39,85,174-176,182} Our work emphasizes the significance of manipulating intrinsic point defects in nanostructured Bi_2Te_3 thermoelectric materials, and future suppression of n_e potentially pushes zT to a higher level.

Associated Content

Supporting Information

Author Information

Corresponding Author

*E-mail: zhigang.chen@usq.edu.au (Z-G. Chen)

zhigang.chen@uq.edu.au (Z-G. Chen)

Acknowledgements

This work was financially supported by the Australian Research Council. ZGC thanks the USQ start-up grant and strategic research grant. The Australian Microscopy and Microanalysis Research Facility is acknowledged for providing characterization facilities.

Supporting Information

Enhanced Thermoelectric Properties of Nanostructured *n*-Type Bi₂Te₃ by Suppressing Te Vacancy through Non-equilibrium Fast Reaction

Yuan Wang^{a,b}, Wei-Di Li^{ub}, Xiao-Lei Shi^{a,b}, Min Hong^{a,b}, Li-Jun Wang^b, Meng Li^b, Hao Wang^a, Jin Zou^{b,c}, Zhi-Gang Chen^{a,b}*

^aCentre for Future Materials, University of Southern Queensland, Springfield central, Queensland 4300, Australia.

^bMaterials Engineering, The University of Queensland, Brisbane, Queensland 4072, Australia.

^cCentre for Microscopy and Microanalysis, The University of Queensland, Brisbane, Queensland 4072, Australia

*Corresponding author. Email: zhigang.chen@usq.edu.au (ZGC); zhigang.chen@uq.edu.au (ZGC)

1. Densities of the sintered Bi₂Te_{3-x} pellets measured by the Archimedes method

Densities of the sintered Bi₂Te_{3-x} pellets were measured using the Archimedes method, and the results are summarized in **Figure S1**. As can be seen, the densities of the sintered Bi₂Te_{3-x} pellets are within the range from 87% to 90% of the Bi₂Te₃ standard density, indicating that a porous structure exists in the pellets.¹ Such a porous structure may contribute to ultralow lattice thermal conductivity (κ_l) of the sintered Bi₂Te_{3-x} pellets.¹ With the suppression of Te vacancies ($V_{Te}^{\bullet\bullet}$), densities of as-sintered Bi₂Te_{3-x} pellets increase, manifesting the successful suppression of $V_{Te}^{\bullet\bullet}$ in our work.

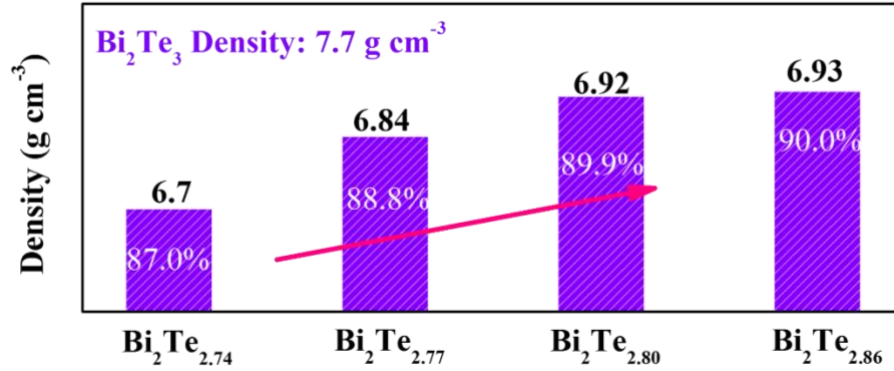


Figure S1. Measured densities of as-sintered Bi₂Te_{3-x} pellets using the Archimedes method.

2. XRD and EDS characterizations of as-prepared Bi₂Te_{3-x} powders and pellets

Figure S2a shows XRD patterns of as-synthesized Bi₂Te_{3-x} powders. The main diffraction patterns of all the Bi₂Te_{3-x} ($x = 0.26, 0.23, 0.20,$ and 0.14) powders can be indexed as the rhombohedral structured Bi₂Te₃ with lattice parameters of $a = 4.3852 \text{ \AA}$, $c = 30.483 \text{ \AA}$ and a space group of $R\bar{3}m$ (PDF#15-0863). Compared with the pristine Bi₂Te_{2.74} ($x = 0.26$) powder, 0 0 15 peaks of Bi₂Te_{2.77} ($x = 0.23$), Bi₂Te_{2.80} ($x = 0.20$), and Bi₂Te_{2.86} ($x = 0.14$) powders present higher intensities, as shown in the magnified XRD patterns in **Figure S2b**. On the other hand, other primary peaks show no obvious changes of the intensity. The higher intensities of 0 0 15 peaks are contributed by the increased amount of tetragonal Cr₂TeO₆ ($P42/mnm$, $a=4.545 \text{ \AA}$, $c=8.99 \text{ \AA}$, PDF#15-0696), generated by adding Cr₂O₃ during the solvothermal synthesis. Moreover, no obvious peak shift is detected in **Figure S2b**, which is in contrast with the left peak shift observed in XRD patterns of Bi₂Te_{3-x} pellets (**Figure 3b**). This hints that the suppression of V_{Te} occurs during the sintering process through the non-equilibrium fast reaction.^{2,3} This is further manifested by the calculated lattice constants and unit cell volumes, as shown in **Figure S2c** and **Figure S2d**, respectively. Lattice constants and unit cell volumes remain similar values for the synthesized Bi₂Te_{3-x} powders, while exhibit increasing trend in the sintered Bi₂Te_{3-x} pellets (**Figure 3c**). Apart from our XRD results, the existence of Cr₂TeO₆ in as-synthesized Bi₂Te_{3-x} powders is also supported by EDS mapping results in **Figure S2e**. The XRD results of **Figure 3a** verifies the existence of Bi₁₈CrO₃₀ in as-sintered Bi₂Te_{3-x} pellets. **Figure S2f** further provides the EDS mappings of Bi, Cr, and O in as-sintered Bi₂Te_{2.8} ($x=0.2$) pellets, indicating the existence of Bi₁₈CrO₃₀ therein.

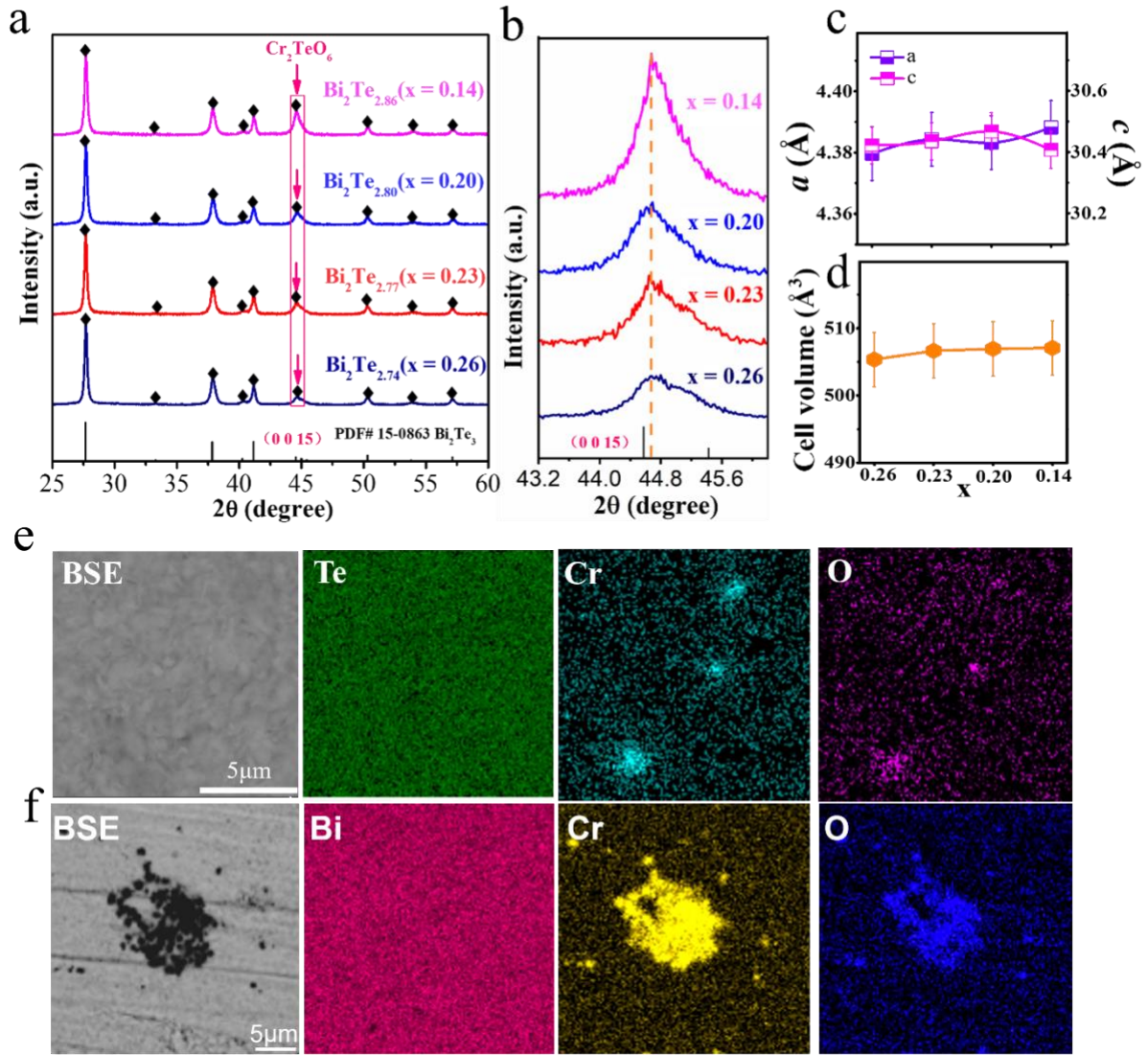


Figure S2. (a) XRD patterns of as-synthesized $\text{Bi}_2\text{Te}_{3-x}$ powders ($x = 0.26, 0.23, 0.20,$ and 0.14); (b) magnified XRD patterns of 0 0 15 peak; and calculated (c) lattice constants and (d) unit cell volumes. (e) EDS mappings of Te, Cr, and O in as-synthesized $\text{Bi}_2\text{Te}_{2.8}$ ($x=0.2$) powders. (f) EDS mappings of Bi, Cr, and O in as-sintered $\text{Bi}_2\text{Te}_{2.8}$ ($x=0.2$) pellets.

3. Calculations of lattice constants and unit cell volumes of both $\text{Bi}_2\text{Te}_{3-x}$ powders and pellets using Bragg's law

The X-ray diffraction (XRD) is based on constructive interference of monochromatic X-rays and a crystalline sample. These X-rays are generated by a cathode ray tube, filtered to produce monochromatic radiation, collimated to concentrate them, and directed toward the sample. The interaction of the incident rays with the sample produces constructive interference (and a diffracted ray) which fit Bragg's law,

$$n\lambda = 2d \sin\theta \quad (\text{S3-1})$$

where d , θ , n and λ are the spacing between diffracting crystal planes, the incident angle, an integer representing the order of the diffraction peak, and the wavelength of the beam, respectively. This law relates the wavelength of electromagnetic radiation to the diffraction angle and the lattice spacing in a crystalline sample, which therefore can be utilized to accurately calculate lattice constants by selecting particular crystal planes.⁴

In this experiment, crystal planes (0 0 15) and (3 0 0) were selected to calculate the lattice constants of our rhombohedral structured Bi_2Te_3 using the equation below⁵ ($a=b \neq c$, $\alpha=\beta=90^\circ$, $\gamma=120^\circ$, $R\bar{3}m$), as they intuitively reflect c and a , respectively.

$$d_{hkl} = \frac{1}{\sqrt{\frac{4}{3}(h^2+hk+k^2)/a^2 + \frac{1}{c^2}}} \quad (\text{S3-2})$$

With a Cu-K α radiation source ($\lambda=0.154$ nm), lattice constants a and c of both $\text{Bi}_2\text{Te}_{3-x}$ powders and pellets were calculated based on Bragg's law, and they are summarized in **Table S1**. Accordingly, the unit cell volume of rhombohedral structured Bi_2Te_3 is calculated as:

$$\text{Volume} = \frac{\sqrt{3}}{2} a^2 c \quad (\text{S3-3})$$

Table S1. Calculated lattice constants and unit cell volumes of both $\text{Bi}_2\text{Te}_{3-x}$ powders and pellets using Bragg's law

x (powder)	a (Å)	c (Å)	Volume (Å) ³
0.26	4.37963	30.4224	505.36
0.23	4.38431	30.435	506.65
0.2	4.38325	30.4674	506.94
0.14	4.38819	30.4071	507.08
x (pellet)	a (Å)	c (Å)	Volume (Å) ³
0.26	4.36419	30.3911	501.28
0.23	4.36518	30.3948	501.57
0.2	4.37806	30.4325	505.16
0.14	4.3852	30.483	507.65

4. Carrier mobility and measured thermal properties of as-sintered $\text{Bi}_2\text{Te}_{3-x}$

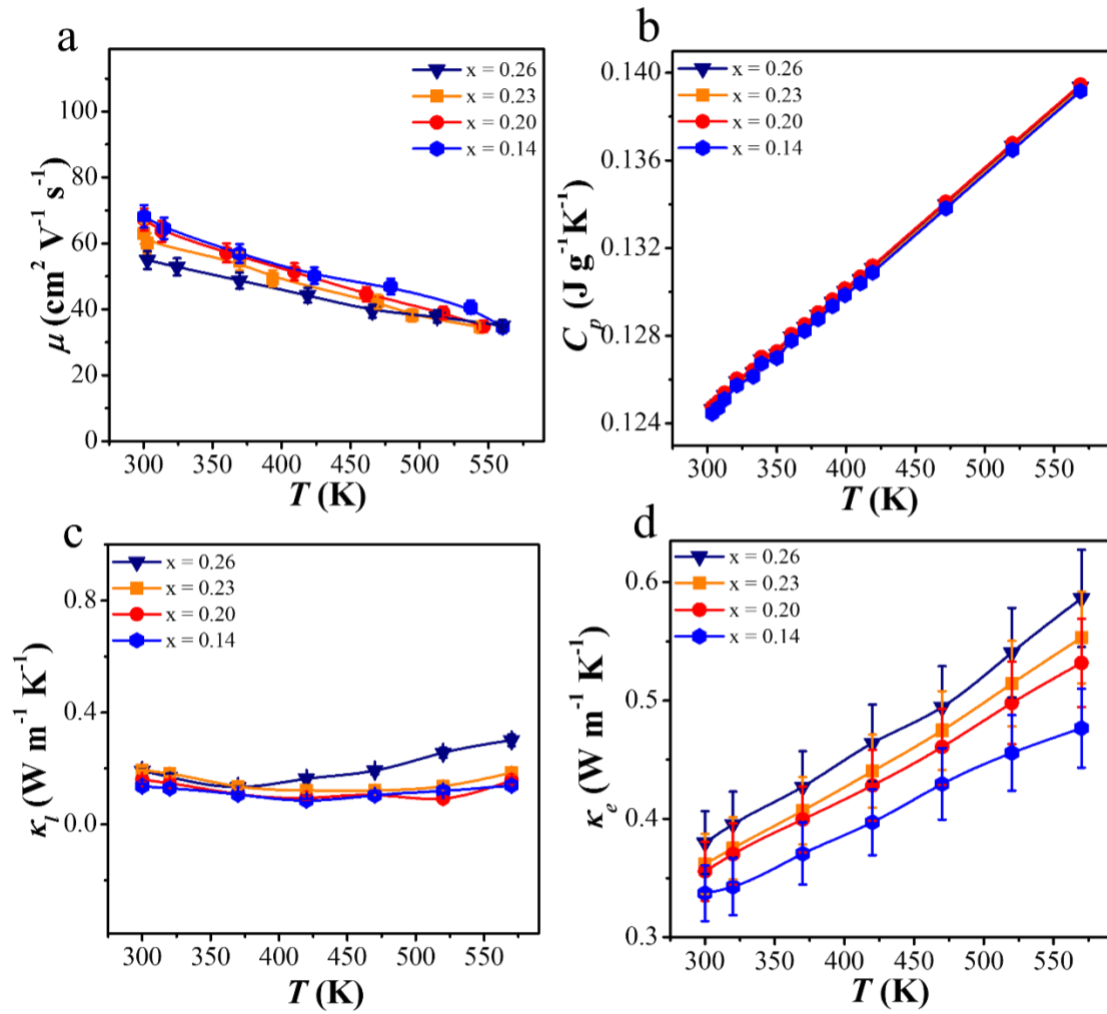


Figure S4. T -dependent (a) carrier mobility (μ); (b) heat capacity (C_p); (c) lattice thermal conductivity (κ_l) and (d) electrical thermal conductivity (κ_e) of as-sintered $\text{Bi}_2\text{Te}_{3-x}$ pellets ($x = 0.26, 0.23, 0.20, \text{ and } 0.14$).

5. SEM and TEM images of as-synthesized Bi_2Te_3 nanoplates and as-sintered $\text{Bi}_2\text{Te}_{3-x}$

Porous structure and nanosized grains induced dense grain boundaries lead strong phonon scatterings and contribute to ultralow lattice thermal conductivity (κ_l) in as-sintered Bi_2Te_3 pellets, as evidenced by SEM and TEM images in **Figure S5**.

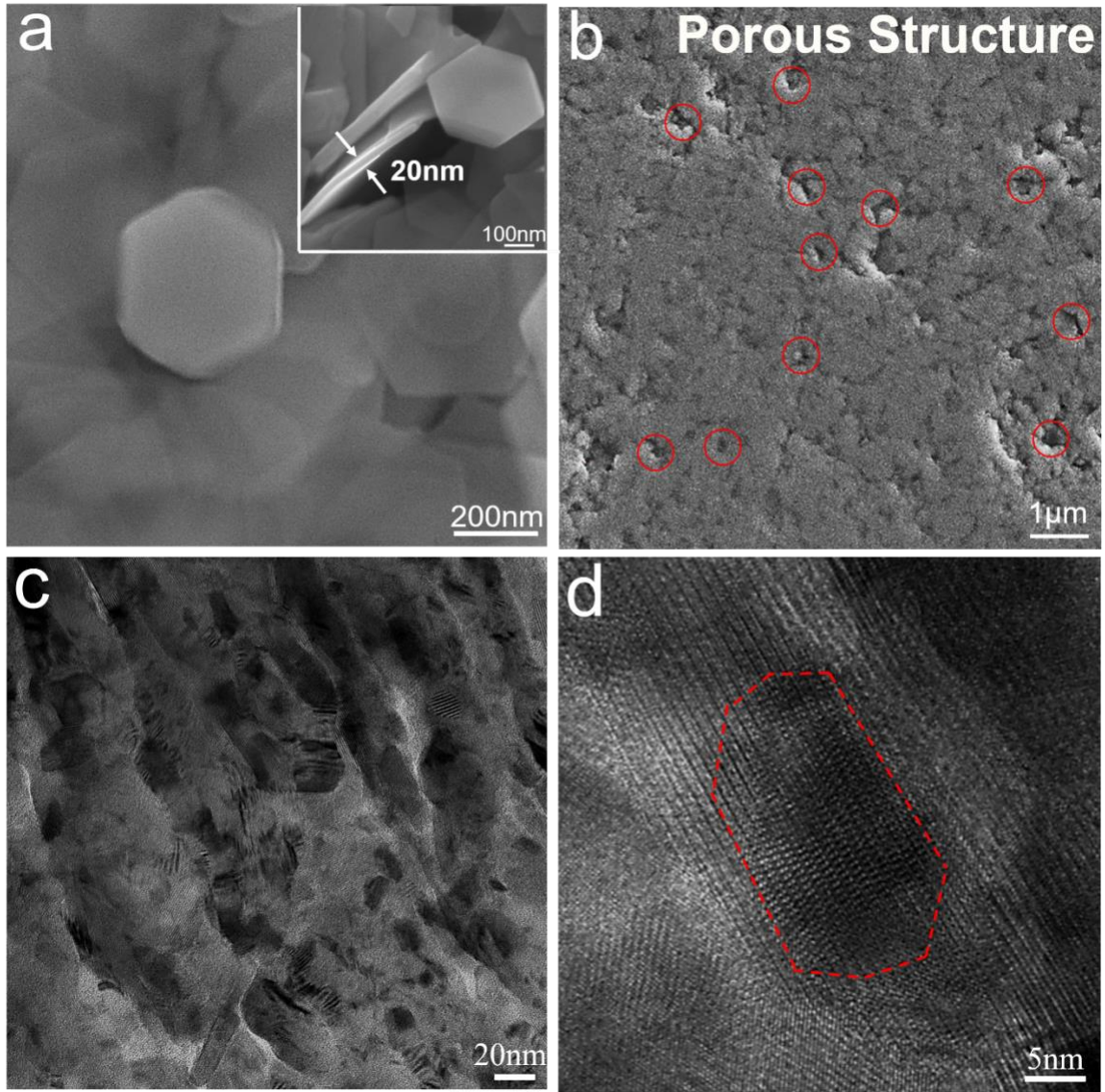


Figure S5. Typical SEM image of (a) as-synthesized Bi_2Te_3 nanoplates, with the inset showing the typical lateral thickness of the nanoplates is around 20 nm, and (b) as-sintered Bi_2Te_3 pellet showing porous structure. TEM image of as-sintered Bi_2Te_3 pellet showing (c) nanosized grains with dense grain boundaries, and (d) one typical nanosized grain.

6. SPB model calculation details

We used a single parabolic band (SPB) model^{6,7} to calculate the enhancement of n -dependent zT with reduced lattice thermal conductivity (κ_l). For calculation details, the carrier transport property analysis was employed as:

$$S(\eta) = \frac{k_B}{e} \cdot \left[\frac{\left(r + \frac{5}{2}\right) \cdot F_{r + \frac{3}{2}}(\eta)}{\left(r + \frac{3}{2}\right) \cdot F_{r + \frac{1}{2}}(\eta)} - \eta \right] \quad (\text{S6-1})$$

$$n = \frac{1}{e \cdot R_H} = \frac{(2m^* \cdot k_B T)^{\frac{3}{2}}}{3\pi^2 \hbar^3} \cdot \frac{\left(r + \frac{3}{2}\right)^2 \cdot F_{r+\frac{1}{2}}^2(\eta)}{\left(2r + \frac{3}{2}\right) \cdot F_{2r+\frac{1}{2}}(\eta)} \quad (\text{S6-2})$$

$$\mu = \left[\frac{4\pi \hbar^4 C_l}{\sqrt{2}(k_B T)^{\frac{3}{2}} E_{Def}^2 (m^*)^{\frac{5}{2}}} \right] \frac{\left(2r + \frac{3}{2}\right) \cdot F_{2r+\frac{1}{2}}(\eta)}{\left(r + \frac{3}{2}\right)^2 \cdot F_{r+\frac{1}{2}}(\eta)} \quad (\text{S6-3})$$

$$L = \left(\frac{k_B}{e}\right)^2 \cdot \left\{ \frac{\left(r + \frac{7}{2}\right) \cdot F_{r+\frac{5}{2}}(\eta)}{\left(r + \frac{3}{2}\right) \cdot F_{r+\frac{1}{2}}(\eta)} - \left[\frac{\left(r + \frac{5}{2}\right) \cdot F_{r+\frac{3}{2}}(\eta)}{\left(r + \frac{3}{2}\right) \cdot F_{r+\frac{1}{2}}(\eta)} \right]^2 \right\} \quad (\text{S6-4})$$

where η , k_B , e , r , R_H , \hbar , C_l , E_{def} , and L are the reduced Fermi level, the Boltzmann constant, the electron charge, the carrier scattering factor ($r = -1/2$ for acoustic phonon scattering), the Hall coefficient, the reduced plank constant, the elastic constant for longitudinal vibrations, the deformation potential coefficient, and the Lorenz number, respectively. Here:

$$C_l = v_l^2 \cdot \rho \quad (\text{S6-5})$$

where v_l is the longitudinal sound velocity and taken as 2884 m s⁻¹ in this study.⁸ $F_i(\eta)$ is the Fermi integral expressed as:

$$F_i(\eta) = \int_0^\infty \frac{x^i}{1+e^{(x-\eta)}} dx \quad (\text{S6-6})$$

To predict the zT enhancement, experimentally measured κ was utilized. Phonon mean free path Λ_b was calculated as:⁹

$$\Lambda_b = \frac{3 \cdot \kappa_{lb}}{C_v v_\alpha} \quad (\text{S6-7})$$

where C_v is the volumetric heat capacity. v_α is the average sound velocity taken as 2147 m s-

Chapter 5 High Porosity in Nanostructured *n*-Type Bi₂Te₃ Obtaining Ultralow Lattice Thermal Conductivity

5.1 Overview

The generation of low lattice thermal conductivity by inducing strong phonon scatterings serves as an effective strategy to enhance thermoelectric efficiency. Porous structure and nanostructure are both well believed to effectively scatter phonons at the pore interfaces and dense grain boundaries, respectively. The simultaneous realization of both structures holds full potential to strongly scatter phonons and in turn render ultralow lattice thermal. However, such a promising strategy is rarely reported. Moreover, conventional fabrications of porous structure may hinder carrier transport by reducing carrier mobility. Maintaining decent electrical performances is necessary to secure high thermoelectric efficiency.

Within our study, porous structure and nanostructure are simultaneously realized in *n*-type Bi₂Te₃ with facile fabrication methods. Benefited from the synergistic effects of both structures, strong phonon scatterings are induced at the pore interfaces and dense grain boundaries, causing ultralow lattice thermal conductivity less than 0.1 W m⁻¹ K⁻¹. Additionally, introduction of pores does not obviously deteriorate the electrical performance, where decent power factor of 10.57 μW cm⁻¹ K⁻¹ is maintained. Ultimately, the ultralow lattice thermal conductivity and well-maintained power factor secure a high zT of 0.97 in *n*-type Bi₂Te₃ at 420 K, which is one of the highest values reported for intrinsic *n*-type Bi₂Te₃.

5.2 Journal publication

The journal publication included in **Chapter 5** is available at *ACS Appl. Mater. Interfaces* **2019**, 11. <https://doi.org/10.1021/acsami.9b12079>.

High Porosity in Nanostructured *n*-Type Bi₂Te₃ Obtaining Ultralow Lattice Thermal Conductivity

Yuan Wang,¹ Wei-Di Liu,² Han Gao,² Li-Jun Wang,² Meng Li,² Xiao-Lei Shi,² Min Hong,¹ Hao Wang,¹ Jin Zou,^{2,3} and Zhi-Gang Chen,^{1,2}*

¹Centre for Future Materials, University of Southern Queensland, Springfield central, Queensland 4300, Australia.

²Materials Engineering, The University of Queensland, Brisbane, Queensland 4072, Australia.

³Centre for Microscopy and Microanalysis, The University of Queensland, Brisbane, Queensland 4072, Australia.

KEYWORDS: *thermoelectrics, bismuth telluride, porous, nanostructure, lattice thermal conductivity*

Abstract

Porous structure possesses full potentials to develop high-performance thermoelectric materials with low lattice thermal conductivity. In this study, *n*-type porous nanostructured Bi₂Te₃ pellet is fabricated by sintering Bi₂Te₃ nanoplates synthesized with a facile solvothermal method. With adequate sublimations of Bi₂TeO₅ during the spark plasma sintering, homogeneously distributed pores and dense grain boundaries are successfully introduced into the Bi₂Te₃ matrix, causing strong phonon scatterings. From which, an ultralow lattice thermal conductivity of $< 0.1 \text{ W m}^{-1} \text{ K}^{-1}$ is achieved in the porous nanostructured Bi₂Te₃ pellet. With the well-maintained decent electrical performance, a power factor of $10.57 \mu\text{W cm}^{-1} \text{ K}^{-2}$ at 420 K, as well as the reduced lattice thermal conductivity secured a promising zT value of 0.97 at 420 K, which is among the highest values reported for pure *n*-type Bi₂Te₃. This study provides the insight of realizing ultralow lattice thermal conductivity by synergistic phonon scatterings of pores and nanostructure in the *n*-type Bi₂Te₃-based thermoelectric materials.

Introduction

Thermoelectric materials, enabling the direct solid-state conversion between heat and electricity, are promising to realize emission-free power generation and refrigeration, and alleviate current energy dilemma.^{5,24,183} To evaluate efficiency of thermoelectric materials, the dimensionless figure of merit (zT) is defined as: $zT = S_2\sigma T/\kappa = S_2\sigma T/(\kappa_e + \kappa_l)$, where S , σ , κ , κ_e , κ_l , and T are Seebeck coefficient, electrical conductivity, total thermal conductivity, electrical thermal conductivity, lattice thermal conductivity, and the absolute temperature, respectively.^{15,18,184} Targeting at high zT , efforts have been devoted to improve the power factor ($S_2\sigma$) through doping engineering¹⁸⁵⁻¹⁸⁷ or band structure engineering,^{150,188,189} and reducing the κ_l through nanostructure engineering.^{152,178,190}

Among various thermoelectric materials, low-temperature ones are well-known for their high conversion efficiencies around the room temperature.^{65,191} They are especially attractive as the power of wearable electronics.¹⁸⁴ Bismuth telluride (Bi_2Te_3), as one of the best low-temperature thermoelectric materials, has intrinsically decent electrical properties due to its narrow band gap (~ 0.15 eV) with high valley degeneracy and anisotropic effective mass.⁴⁴ By means of alloying/doping with ternary elements,^{75,192} its electrical performance can be further boosted, and a record-high $S_2\sigma$ of $\sim 45 \mu\text{W cm}^{-1} \text{K}^{-2}$ was reported at 300 K from both sulphur doped Bi_2Te_3 ¹⁹² and $\text{Bi}_{0.5}\text{Sb}_{1.5}\text{Te}_3$.¹⁹¹ In order to further improve its zT , efforts have been devoted to reduce κ_l by inducing strong phonon scatterings.^{37,65,191} Specifically, defect engineering, including the introduction of point defects⁶⁵ or dislocations,¹⁹¹ was reported in the Bi_2Te_3 -based alloys. With the effective phonon scatterings due to defect engineering, reduced $\kappa_l \sim 0.3 \text{ W m}^{-1} \text{K}^{-1}$ was achieved at 300 K in the $\text{Bi}_{0.5}\text{Sb}_{1.5}\text{Te}_3$.¹⁹¹ Moreover, nanostructure engineering was reported to induce a high density of grain boundaries in the Bi_2Te_3 . As a result, significant phonon scatterings were caused, leading ultralow κ_l of $\sim 0.2 \text{ W m}^{-1} \text{K}^{-1}$ at 370 K.³⁷ In addition, porous structure is also known to effectively reduce κ_l .^{174,193,194} Due to the intensive phonon scatterings at the pore-induced interfaces, ultralow κ_l of $0.13 \text{ W m}^{-1} \text{K}^{-1}$ was reported at 488 K in the $\text{Bi}_2\text{Te}_{2.5}\text{Se}_{0.5}$.¹⁹⁴ In spite of these progresses, lower κ_l is still desiring for Bi_2Te_3 to achieve higher zT . According to the Callaway model, κ_l has positive relevance with the phonon relaxation time (τ), as defined below:¹⁹⁵

$$\kappa_l = \frac{1}{3} \int_0^{\omega_{max}} C_s(\omega) v_g(\omega)^2 \tau(\omega) d\omega \quad (1)$$

where C_s is the spectral heat capacity and v_g is the phonon group velocity. Based on the Matthiessen rule,¹⁹⁶ τ is further negatively related to the sum effects of different phonon scattering sources. Therefore, the combination of different phonon scattering sources can

contribute to smaller τ due to full-spectrum phonon scattering, which could in turn lead lower κ_l .

Here, in this work, we prepared nanostructured *n*-type Bi₂Te₃ with porous structure *via* a facile solvothermal method and subsequent sparking plasma sintering (SPS), as schematically shown in **Figure 1a**. During the sintering process, the Bi₂TeO₅ sublimed under the heating environment and large plasma currents.¹⁹⁷ Consequently, nanostructured Bi₂Te₃ with porous structure was fabricated. The density of as-prepared porous nanostructured Bi₂Te₃ is 6.536 g cm⁻³ (85 %). With the synergistic effects of both pores and nanostructure, strong phonon scatterings were induced, leading ultralow κ_l of less than 0.1 W m⁻¹ K⁻¹ at 420 K. Consequently, promising zT of ~ 1 was achieved, which is among the highest values reported for pure *n*-type Bi₂Te₃.^{37,39,174,198} **Figure 1b** compared our results with previously reported porous¹⁷⁴ or nanostructured Bi₂Te₃,³⁷ it was found that the simultaneous introduction of the nanostructure and the porous structure in our study can effectively generate further reduced κ_l , which in turn produce improved zT . Based on the analysis of single parabolic band (SPB) model as shown in **Figure 1c**,^{17,199} further reduced κ_l could potentially pushes zT to a higher level with appropriately engineered n_e .

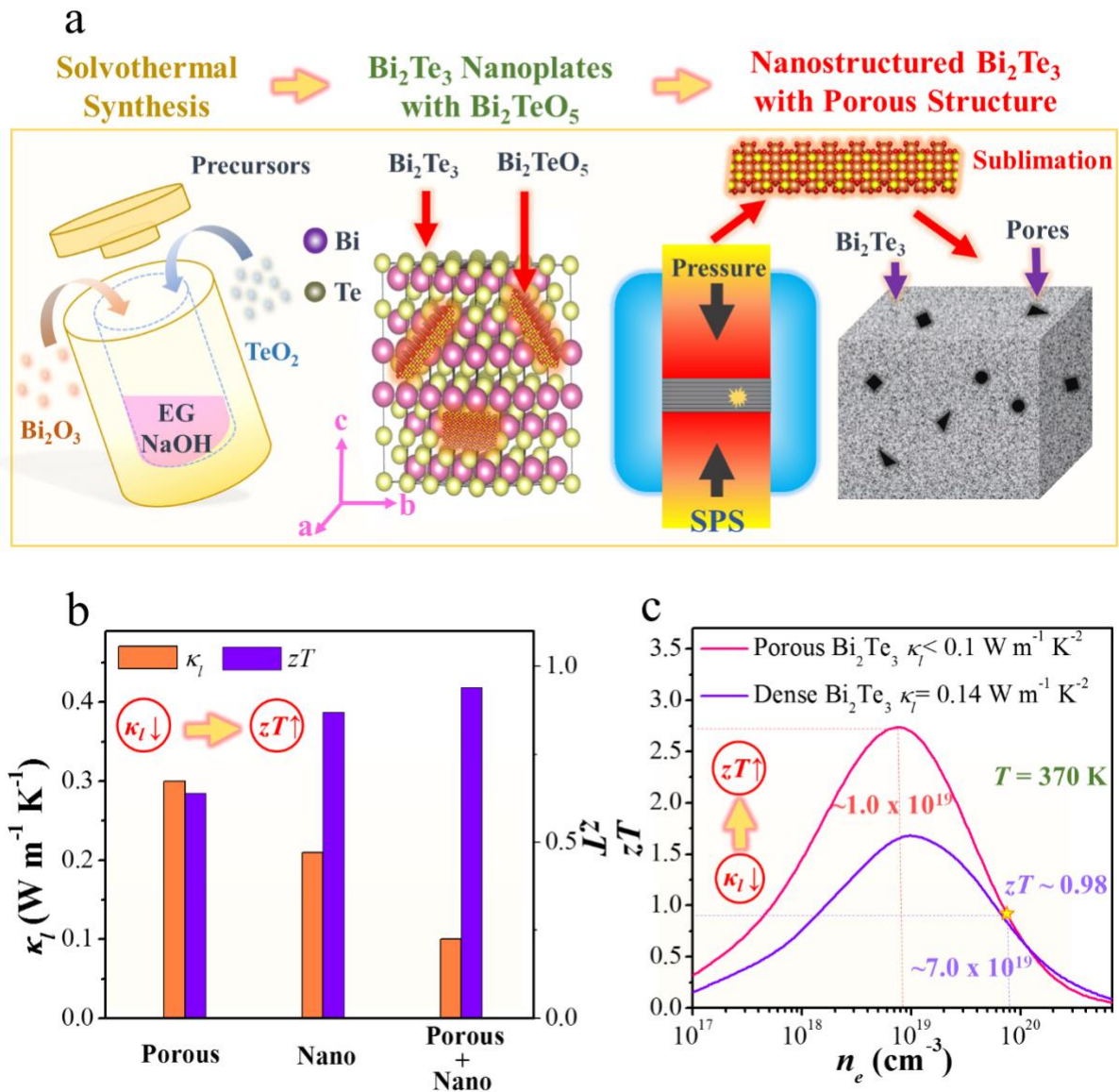


Figure 1. Enhancement of zT from reduced κ_l in the nanostructured Bi₂Te₃ with porous structure. (a) Illustration of the fabrication processes, where solvothermal synthesis and SPS technique were applied. (b) Comparisons of κ_l and zT between this work and previously reported porous¹⁷⁴ or nanostructured Bi₂Te₃.³⁷ (c) Calculation results of SPB showing the possibility to further enhance zT with controlled n_e and reduced κ_l .

Results and discussions:

Figure 2a shows the XRD patterns of as-synthesized Bi₂Te₃ nano-powders and as-sintered nanostructured porous Bi₂Te₃ pellet along the in-plane direction, respectively. The diffraction peaks of the powders can be exclusively indexed as the combination of Bi₂Te₃ (hexagonal

structure, R-3m space group, PDF#15-0863) and Bi_2TeO_5 (orthorhombic structure, Cm2a space group, PDF#38-0420). However, after the SPS process, diffraction peaks of as-sintered pellet can be only indexed as typical Bi_2Te_3 . The disappearance of Bi_2TeO_5 during the sintering process might be attributed to the sublimation of Bi_2TeO_5 under SPS heat treatments and large currents.¹⁹⁷ The X-ray spectroscopy (XPS) was further utilized to verify the sublimation of Bi_2TeO_5 during the SPS process. **Figure 2b** and **Figure 2c** show the high-resolution scans of XPS spectra for Te in both Bi_2Te_3 nano-powders and nanostructured porous Bi_2Te_3 pellet. As can be seen, strong singlet peaks of Te $3d_{5/2}$ and Te $3d_{3/2}$ were detected at the binding energy of 572.23 eV and 582.53 eV in both powder and pellet. This indicates the existence of Te^{2+} .^{175,200} Additional peaks at the binding energy of 575.67 eV and 586.14 eV evidencing the existence of Te^{4+} were only found in the powders.¹⁷⁵ The Te^{2+} and Te^{4+} should be ascribed to Bi_2Te_3 and Bi_2TeO_5 , respectively. The disappearance of Te^{4+} peaks after the SPS process further confirms the sublimation of Bi_2TeO_5 .

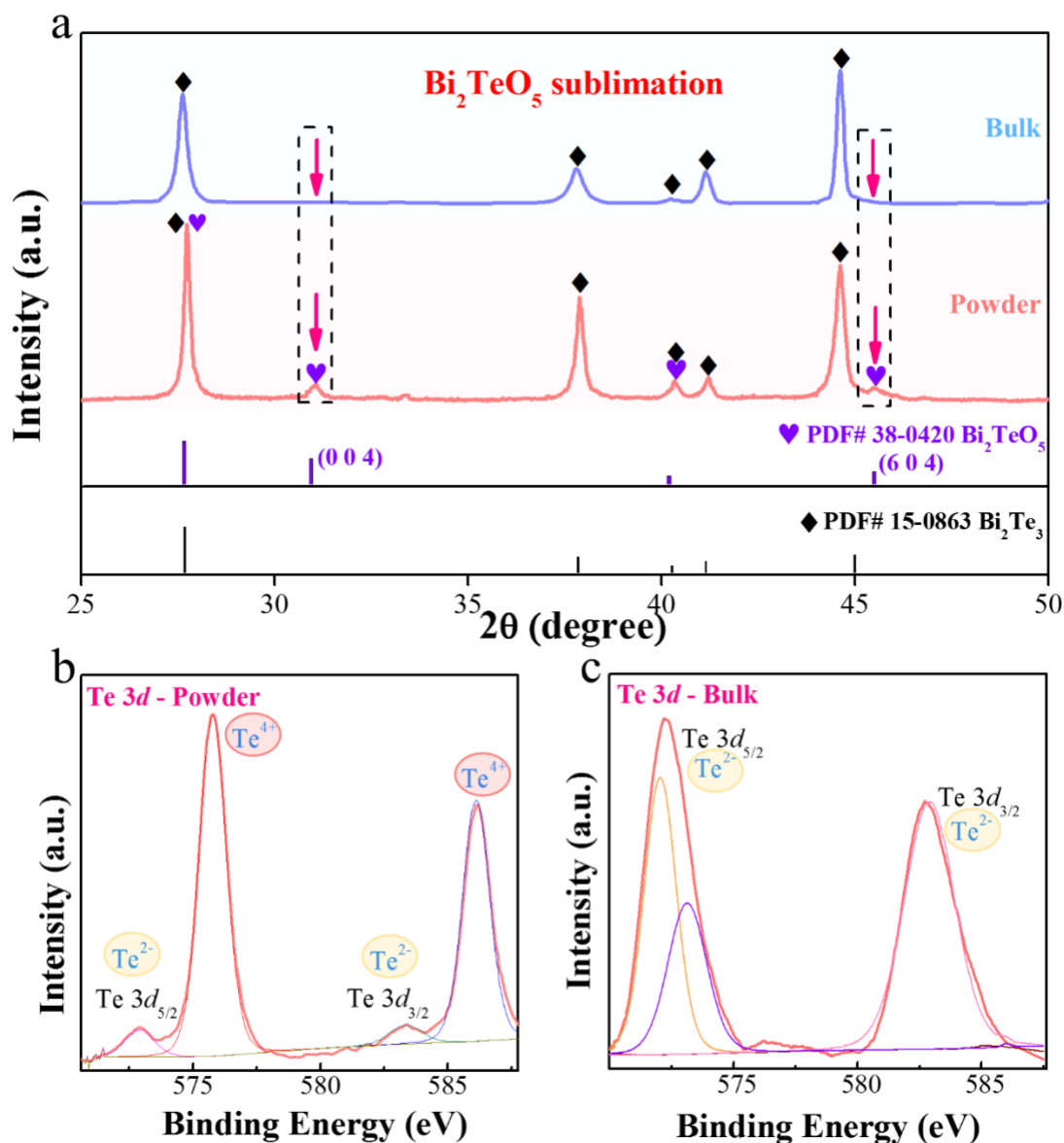


Figure 2. XRD and XPS of synthesized powder and sintered bulk. (a) XRD patterns of both as-synthesized Bi₂Te₃ nano-powders and as-sintered nanostructured porous Bi₂Te₃ pellet; high-resolution XPS scan of Te in the (b) as-synthesized Bi₂Te₃ nano-powders and (c) as-sintered nanostructured porous Bi₂Te₃ pellet.

Figure 3a-3c show the SEM images of synthesized powder, from low magnification to high magnification. It can be observed that as-synthesized Bi₂Te₃ nano-powders are hexagonal nanoplates, with typical lateral thickness of ~20 nm, as shown in the inset of **Figure 3c**. Such nanostructures can contribute to a high density of grain boundaries in the pellet after the sintering.³⁹ **Figure 3d-3f** show low-magnification and high-magnification SEM images of as-sintered nanostructured porous Bi₂Te₃ pellet. As highlighted in the image, porous structure can

be clearly seen, with pores homogeneously distributed in the matrix. **Figure 3f** shows one pore randomly selected in the matrix. It can be found the pore is in nanoscale, whose size is ~400 nm.

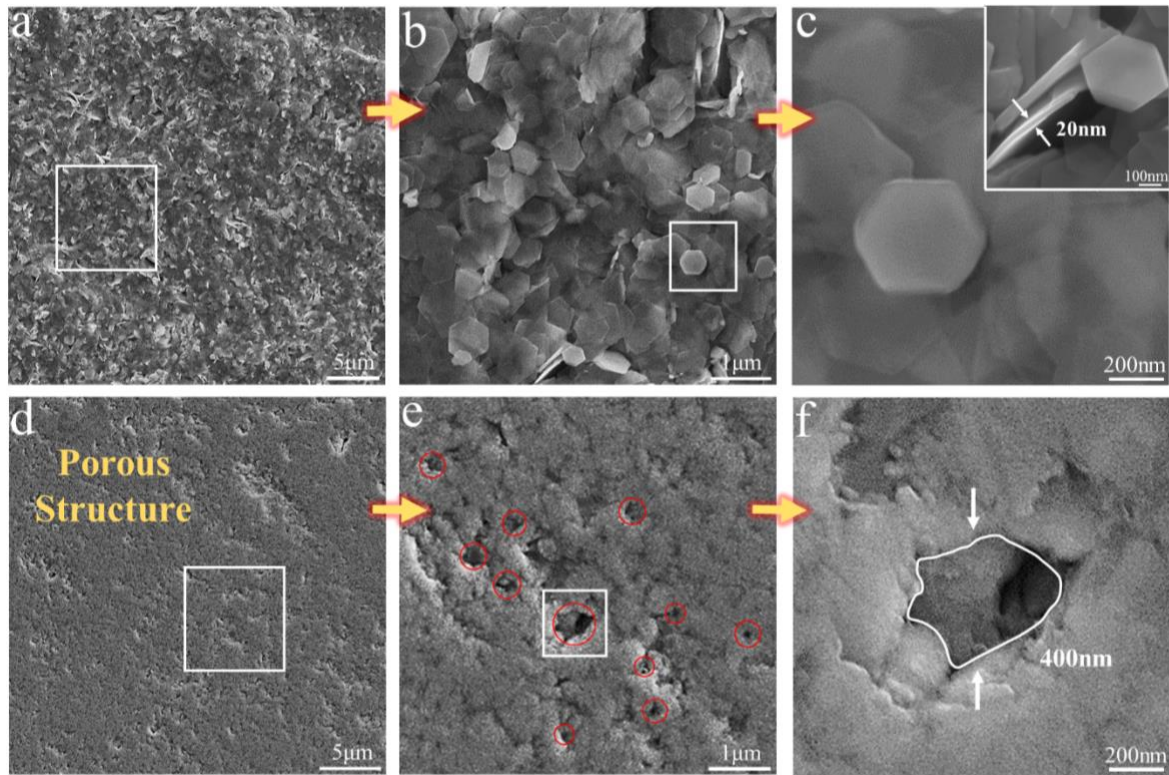


Figure 3. SEM images of synthesized powder and sintered bulk. (a) SEM image of as-synthesized Bi_2Te_3 nano-powder; (b) magnified SEM image of the area selected in (a); and (c) magnified SEM image of the area selected in (b), showing the hexagonal plate-like nanostructure. Inset is the SEM image showing the typical lateral thickness of the nanoplates is around 20 nm. (d) SEM image of as-sintered nanostructured porous Bi_2Te_3 ; (e) magnified SEM image of the area selected in (d); and (f) magnified SEM image of the pore selected in (e), showing the typical pore size of 400 nm.

Figure 4a show the energy dispersive spectroscopy (EDS) results conducted for as-sintered nanostructured porous Bi_2Te_3 pellet. EDS spot analysis (spot highlighted in the inset) suggests that the sample show binary composition, with Bi and Te exclusively detected. EDS mapping and corresponding backscattered electrons (BSE) image are shown as the inset, where homogeneous distributions of Bi and Te were observed. The atomic ratios of Bi and Te were evaluated as 41.2 % and 58.8 %, respectively. **Figure 4b** shows the electron probe micro-analyzer (EPMA) results, where the composition of as-sintered nanostructured porous pellet

was more accurately determined. The average ratio between Bi and Te in the bulk is around 0.715 indicating a composition of $\text{Bi}_2\text{Te}_{2.8}$.

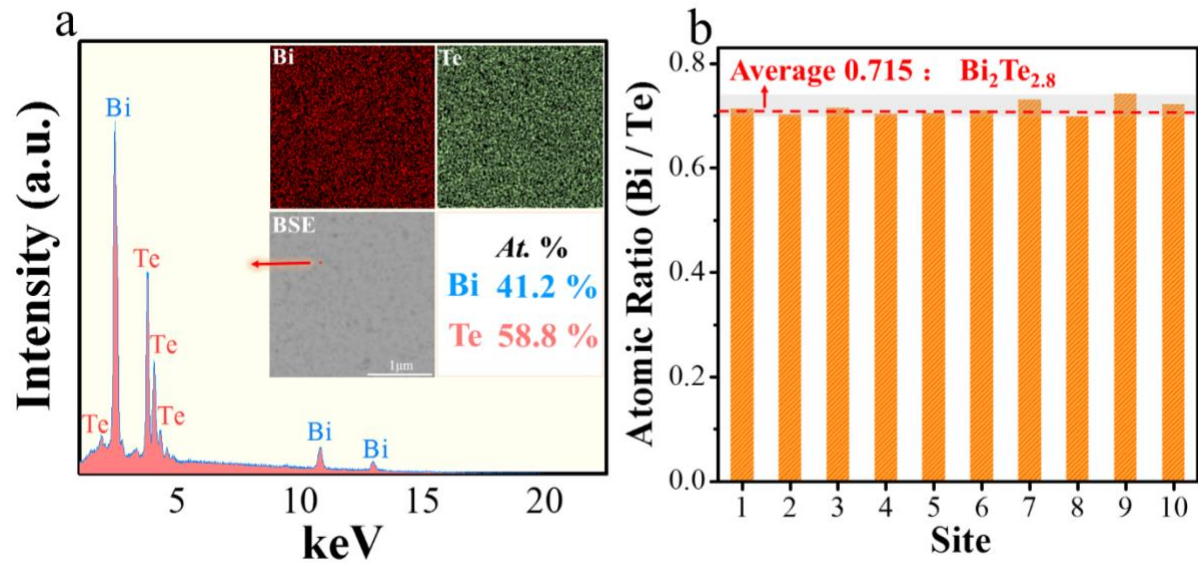


Figure 4. EDS and EPMA of sintered bulk. (a) EDS spot spectrum of as-sintered nanostructured porous Bi_2Te_3 pellet with the inset of mapping results of Bi and Te. (b) Atomic ratios between Bi and Te measured by EPMA at ten randomly selected area in the as-sintered nanostructured porous Bi_2Te_3 pellet.

Figure 5 shows the measured thermoelectric properties of as-sintered nanostructured porous Bi_2Te_3 pellet along the in-plane direction, including σ , n , μ , S and κ . In order to understand the effects of porous structure, thermoelectric properties are compared with previously reported dense nanostructured Bi_2Te_3 pellet.³⁷ As can be seen from the **Figure 5a**, σ of as-sintered nanostructured porous pellet showed no obvious difference than dense nanostructured Bi_2Te_3 pellet, and decreased gradually with increasing T , presenting typical metallic transport behaviours.¹⁷⁷ The peak σ of 770 S cm^{-1} occurred at 300 K, which is comparable to other reported pure Bi_2Te_3 .^{37,198,201} The measured n and μ are shown in **Figure 5b**. It was found that n slightly increases from $7 \times 10^{19} \text{ cm}^{-3}$ to $1 \times 10^{20} \text{ cm}^{-3}$ in the temperature range of 300 K to 550 K, while μ gradually decreases with higher temperature, with the value of $66 \text{ cm}^2 \text{ V}^{-1} \text{ s}^{-1}$ at 300 K. Such a μ is similar to other porous Bi_2Te_3 -based thermoelectric bulks.^{194,202} In terms of S , as shown in **Figure 5c**, negative values were measured, indicating typical n -type properties. The peak value of $-145 \mu\text{V K}^{-1}$ was available at around 450 K, which is also similar to the dense nanostructured Bi_2Te_3 .^{37,201} As a result, uncompromised $S_2\sigma$ was shown in **Figure 5d**, with peak value of $12.89 \mu\text{W cm}^{-1} \text{ K}^{-2}$ at 320 K. It can be concluded that the

introduction of pores possesses negligible effects on electrical properties of our nanostructured porous Bi₂Te₃ pellet along the in-plane direction. This might be ascribed to the strong anisotropy of Bi₂Te₃,^{86,203,204} where negative effects of pores is compensated by the outstanding carrier transport in the in-plane direction. **Figure 5e** shows calculated κ of as-sintered nanostructured porous Bi₂Te₃ pellet. It was found that introduction of pores led to lower κ at all temperature range from 300 K to 560 K, with the lowest value of $\sim 0.5 \text{ W m}^{-1} \text{ K}^{-1}$ at 418 K. In order to understand such an ultralow κ , we investigated κ_e and κ_l using the Wiedemann – Franz law,¹⁸¹ where $\kappa_e = L\sigma T$ and $\kappa_l = \kappa - \kappa_e$. L is the Lorenz number and was calculated based on SPB model.^{17,199} It was found that κ_e lied in the range of $0.39 \text{ W m}^{-1} \text{ K}^{-1}$ to $0.47 \text{ W m}^{-1} \text{ K}^{-1}$, which is comparable to the values of dense nanostructured Bi₂Te₃.³⁷ Therefore, the reduction of κ of as-sintered nanostructured porous Bi₂Te₃ pellet mainly derives from κ_l . **Figure 5e** shows calculated κ_l in as-sintered nanostructured porous Bi₂Te₃ pellet. It was found porous structure can effectively reduce κ_l and ultralow κ_l less than $0.1 \text{ W m}^{-1} \text{ K}^{-1}$ was found at 370 K. This significant reduction can be understood with phonon gas theory, where κ_l can be written as $\kappa_l = (1/3)C_v v l$. Among which, C_v is the specific heat capacity at a constant volume, v is the sound velocity and l is the phonon mean free path.²⁰⁵ Reduced ρ of the porous bulk can negatively contribute to C_v , considering $C_v = C'_v \rho$, where C'_v reflects the specific heat properties of the materials.²⁰⁶ Moreover, formation of pores has been proved to reduce v and l of thermoelectric materials.²⁰⁶ As a result, κ_l was significantly reduced in our porous structure, and in turn lead ultralow κ . Benefited from uncompromised $S_2\sigma$ and effectively reduced κ , we ultimately realized boosted zT near 1 at 370 K, as shown in the **Figure 5f**. Such promising zT is among the highest values reported for pure n -type Bi₂Te₃ so far.^{37,39,198}

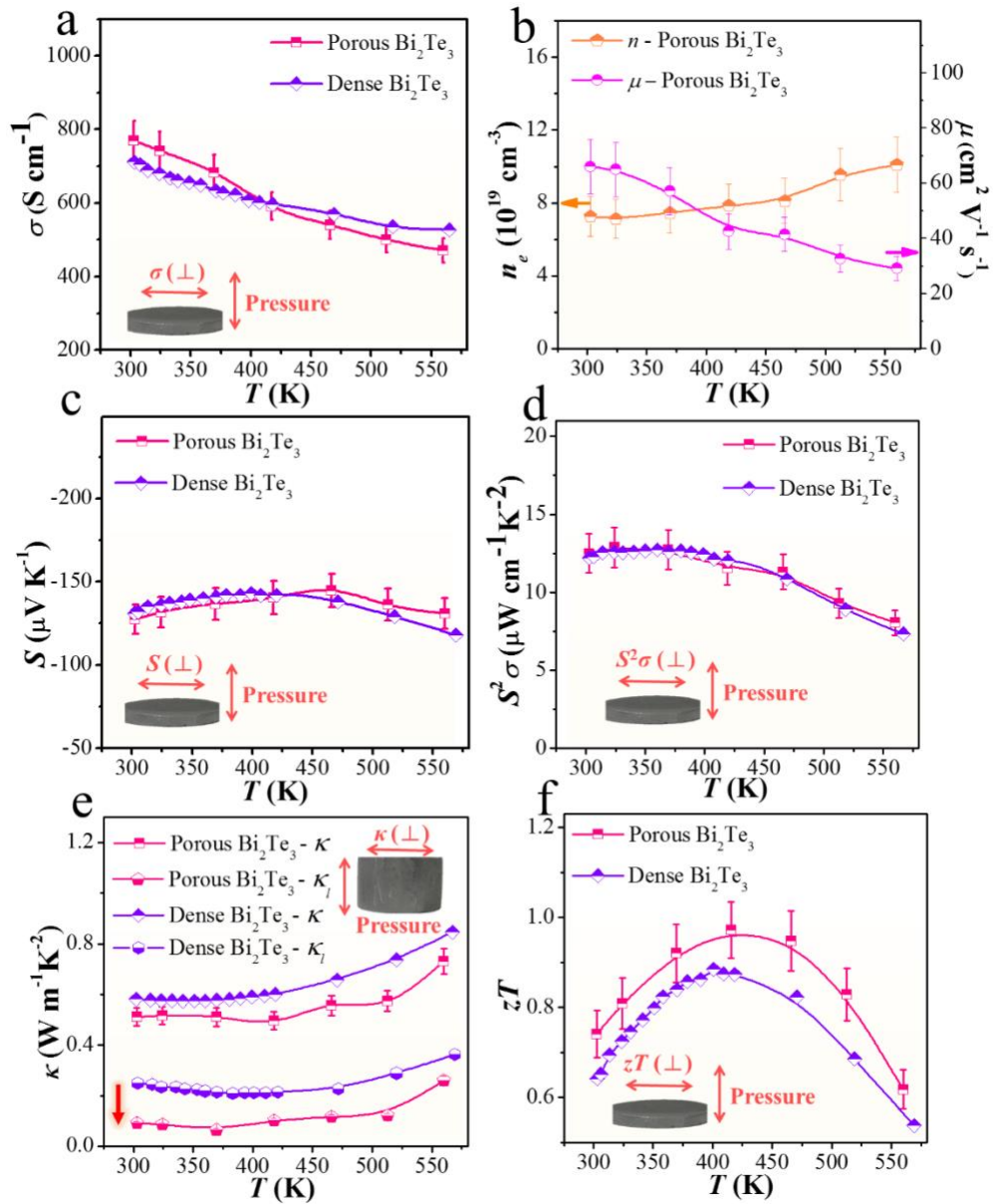


Figure 5. Measured thermoelectric properties of sintered bulk in the in-plane direction. T -dependent (a) σ ; (b) n and μ ; (c) S ; (d) $S^2\sigma$; (e) κ and κ_l ; and (f) zT of as-sintered nanostructured porous Bi_2Te_3 pellet compared with dense nanostructured Bi_2Te_3 .³⁷

Conclusion:

In summary, we fabricated n -type porous nanostructured Bi_2Te_3 pellet with facile solvothermal method and subsequent SPS technique. With adequate sublimations of Bi_2TeO_5 during the sintering process, homogeneously distributed pores were successfully introduced into the nanostructured Bi_2Te_3 pellet. As a consequence of simultaneous strong phonon scatterings at both dense grain boundaries due to nanostructure engineering and interfaces induced by pores, an ultralow κ_l ($< 0.1 \text{ W m}^{-1} \text{ K}^{-1}$) was realized. The well-maintained decent electrical

performance, a $S_2\sigma$ of $10.57 \mu\text{W cm}^{-1} \text{K}^{-2}$ at 420 K, as well as the reduced κ_l secured promising $zT \sim 1$, which is among the highest values reported for pure n -type Bi_2Te_3 .^{37,39,174,198} This study provides an alternative insight of realizing ultralow κ_l by synergistic phonon scatterings of pores and nanostructure in n -type Bi_2Te_3 -based thermoelectric materials.

Experimental Section:

Synthesis Method. Bi_2Te_3 nanoplates were synthesized *via* a typical solvothermal route. Analytical grade bismuth oxide (Bi_2O_3 , 99.9%), tellurium dioxide (TeO_2 , 99.999%), ethylene glycol (EG), polyvinylpyrrolidone (PVP, average molecular weight = 40000) and sodium hydroxide (NaOH, 99.99%) were purchased from Sigma-Aldrich as precursors without any further purification. Details of the synthesis procedures are described as follows. Firstly, PVP was dissolved into EG (36 ml) as the surfactant, followed by 20 min vigorous stirring in order to form a clear solution. Then Bi_2O_3 and TeO_2 were added into the solution as the source materials of bismuth and tellurium, respectively. 5 mol/L NaOH (4 ml) was dropped into the solution to provide the alkaline environment. The solution was stirred for 30 min to uniformly mix precursors, before sealed in a 125 ml polytetrafluoroethylene-lined stainless steel autoclave. The autoclave was heated to 210°C for 24 h and naturally cooled down to the room temperature. Synthesized products were collected by centrifugation and washed with deionized water and ethanol for several times, and finally dried in the oven at 60°C for 12 h.

Spark Plasma Sintering (SPS) and Thermoelectric Properties Measurements. In order to measure the thermoelectric properties, synthesized powders were sintered into a disc-shaped bulk ($\Phi = 12.6 \text{ mm}$) by SPS (SPS-211Lx, Fuji Electronic Co., Ltd.) at 300°C for 5 min under 60 MPa pressure. Density (ρ) of the bulk (92%) was measured using Archimedes method. Due to the strong anisotropy of Bi_2Te_3 ,^{86,203,204} thermoelectric properties of the bulk were only measured in the in-plane direction, which was reported to be the high-performance direction.²⁰⁴ Among which, σ and S were measured simultaneously using ZEM3 (ULVAC Technologies, Inc.) within the temperature range between 300 and 573 K; the thermal diffusivity D was measured by LFA 457 (NETZSCH Group), which was subsequently applied to calculate $\kappa = D \cdot C_p \cdot \rho$,²⁰⁷ where C_p is the specific heat capacity measured by DSC 404 C (NETZSCH Group); n and μ were measured by the Hall system under a reversible magnetic field of 1.5 T. Measurements of the bulks are conducted for at least three times in order to ensure the repeatability.

Characterization. Both synthesized powder and sintered bulk were systematically characterized. XRD (Bruker-D8) was applied to determine the composition and crystal structure of both as-synthesized Bi₂Te₃ nano-powder and as-sintered nanostructured porous Bi₂Te₃ pellet, where bulk sample was characterized along the in-plane direction. XPS (Kratos Axis Ultra) was used to investigate the valence states of Te in Bi₂Te₃ and Bi₂TeO₅. SEM (JEOL JSM-7100F) were utilized to observe the morphology and structural characteristics. EPMA (JEOL JXA-8200) was used to determine the chemical composition of the sample. The instrumental deviation of EPMA is 0.1% and ten randomly selected areas of the sample were measured. EDS mapping and spots (installed in HITACHI-SU3500) were conducted to verify the element distribution and the chemical composition of the sample, respectively.

ASSOCIATED CONTENT

Supporting Information. XPS spectra; Lorenz factor and measured thermal properties; EPMA results; and SPB calculation details.

AUTHOR INFORMATION

Corresponding Author

*E-mail: zhigang.chen@usq.edu.au (Z-G. Chen)

zhigang.chen@uq.edu.au (Z-G. Chen)

ACKNOWLEDGMENTS

This work was financially supported by the Australian Research Council. ZGC thanks the USQ start-up grant and strategic research grant. The Australian Microscopy and Microanalysis Research Facility is acknowledged for providing characterization facilities.

Supporting Information

High Porosity in Nanostructured *n*-Type Bi₂Te₃ Obtaining Ultralow Lattice Thermal Conductivity

Yuan Wang,¹ Wei-Di Liu,² Han Gao,² Li-Jun Wang,² Meng Li,² Xiao-Lei Shi,² Min Hong,¹ Hao Wang,¹ Jin Zou,^{2,3} and Zhi-Gang Chen*,^{1,2}

¹Centre for Future Materials, University of Southern Queensland, Springfield central, Queensland 4300, Australia.

²Materials Engineering, The University of Queensland, Brisbane, Queensland 4072, Australia.

³Centre for Microscopy and Microanalysis, The University of Queensland, Brisbane, Queensland 4072, Australia

Corresponding author: ¹ zhigang.chen@usq.edu.au, ² zhigang.chen@uq.edu.au

1. Magnified XRD results of as-synthesized Bi₂Te₃ powder and as-sintered Bi₂Te₃ pellet

Te vacancy can be manifested from the peak shift in our magnified XRD results in the **Fig. S1**. Specifically, Te vacancy can lead lattice shrinkage in Bi₂Te₃ due to the absence of Te atoms. According to Bragg's Law, this will accordingly induce higher θ of the XRD peaks, which is reflected from the shifted (0 0 15) peaks of both powder and pellet samples towards higher degree.

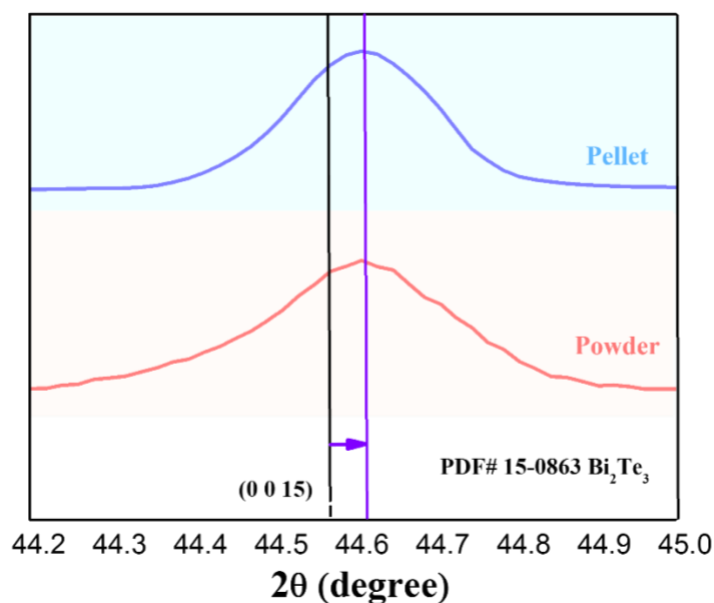


Fig. S1. Magnified XRD results of as-synthesized Bi_2Te_3 powder and as-sintered Bi_2Te_3 pellet, where peak shift towards higher degree is observed.

2. XPS spectra of as-synthesized Bi_2Te_3 powder and as-sintered Bi_2Te_3 pellet

Full X-ray spectroscopy (XPS) spectra of as-synthesized Bi_2Te_3 nano-powder and as-sintered porous nanostructured Bi_2Te_3 pellet are shown in **Fig. S2a** and **Fig. S2b**, respectively. The presences of Bi 4f and Te 3d energy states were exclusively determined, without any energy states detected for other elements, except C 1s and O 1s. Corresponding high-resolution XPS scans of Bi in the as-synthesized Bi_2Te_3 nano-powder and as-sintered porous nanostructured Bi_2Te_3 pellet are shown in **Fig. S2c** and **Fig. S2d**, respectively. No obvious difference was found after the sintering. The existence of single valence state Bi^{3+} in both Bi_2Te_3 nano-powder and porous nanostructured Bi_2Te_3 pellet was verified, where peaks of Bi 4f_{5/2} and Bi 4f_{7/2} were detected at 162.5 eV and 157.2 eV, respectively.¹⁷⁵

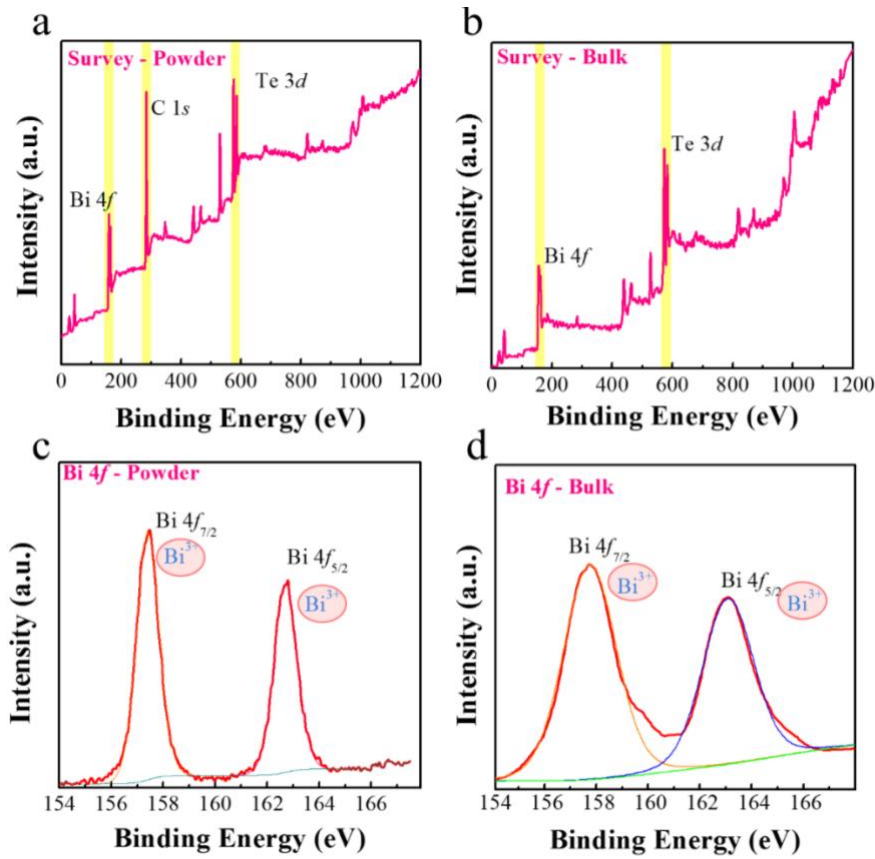


Fig. S2. Full XPS spectra of (a) as-synthesized Bi₂Te₃ nano-powder and (b) as-sintered porous nanostructured Bi₂Te₃ pellet. High-resolution XPS scans of Bi in the (c) as-synthesized Bi₂Te₃ nano-powder and (d) as-sintered porous nanostructured Bi₂Te₃ pellet.

3. Lorenz factor and measured thermal properties

Fig. S3a shows the SPB-calculated Lorenz factor (L) of as-sintered porous nanostructured Bi₂Te₃ pellet. L was found to be around $1.8 \times 10^{-8} \text{ v}^2 \text{ K}^{-2}$, with no obvious change within the temperature between 300 K and 550 K. **Fig. S3b** shows calculated electrical thermal conductivity (κ_e) of as-sintered porous nanostructured Bi₂Te₃ pellet. Similar values were found compared with dense nanostructured Bi₂Te₃ pellet.³⁷ **Fig. S3c** shows measured thermal diffusivity (D) of as-sintered porous nanostructured Bi₂Te₃ pellet. **Fig. S3d** shows measured heat capacity (C_p) of as-sintered porous nanostructured Bi₂Te₃ pellet, which is well consistent with dense nanostructured Bi₂Te₃ pellet.³⁷

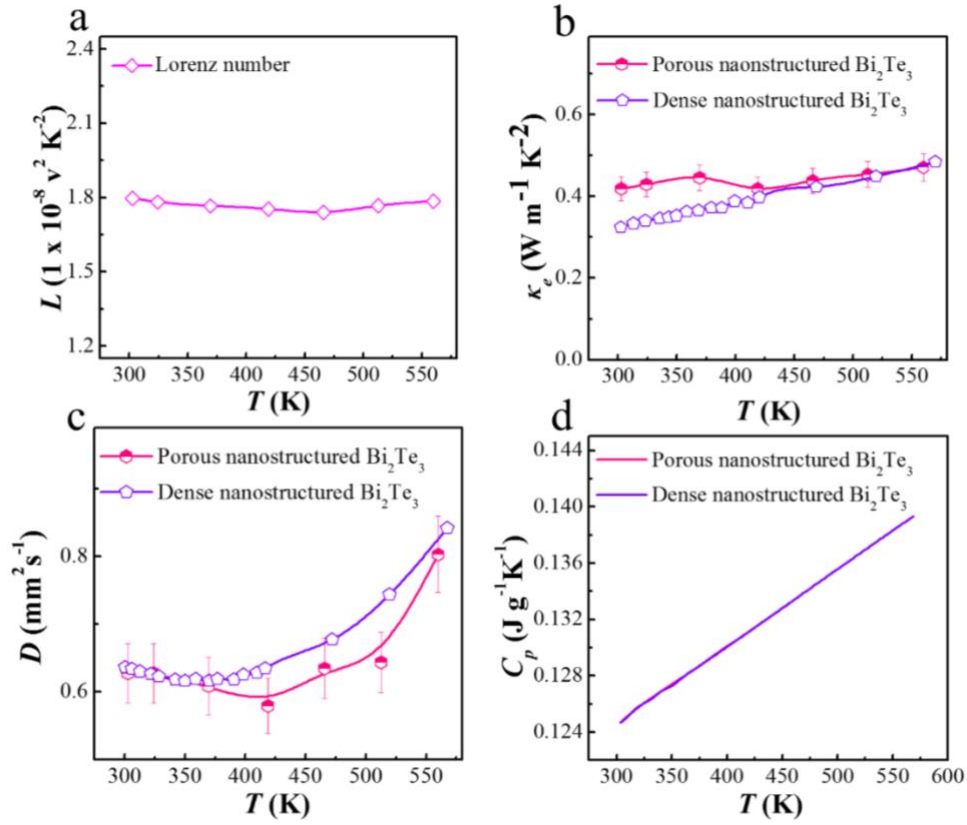


Fig. S3. (a) Calculated Lorenz factor with SPB model. T -dependent (b) κ_e ; (c) D and (d) C_p of as-sintered porous nanostructured Bi_2Te_3 pellet and dense nanostructured Bi_2Te_3 pellet.³⁷

4. EPMA results

Table S1 shows detailed atomic composition of as-sintered porous nanostructured Bi_2Te_3 pellet characterized by electron probe micro-analyzer (EPMA). Ten sites were randomly selected to ensure the reliability and accuracy of the pellet composition.

Table S1. EPMA measured atomic composition of as-sintered porous nanostructured Bi_2Te_3 pellet.

Point	Bi (at. %)	Te (at. %)	Total (at. %)	Bi/Te
1	35.2934	49.3951	100	0.714512
2	33.1585	46.3125	100	0.715973
3	33.2491	47.0595	100	0.706533
4	37.0272	50.6173	100	0.731513
5	36.3166	48.8793	100	0.742985
6	38.8218	55.1961	100	0.703343
7	39.0351	55.3944	100	0.704676
8	39.134	55.0341	100	0.711086
9	38.4345	54.9078	100	0.699983
10	38.5582	53.2736	100	0.723777
Average	36.90284	51.60697	100	0.715438

5. SPB model calculation details

We used a single parabolic band (SPB) model^{17,199} to calculate the enhancement of n -dependent zT with reduced lattice thermal conductivity (κ_l). For calculation details, the carrier transport property analysis was employed as:

$$S(\eta) = \frac{k_B}{e} \cdot \left[\frac{\left(r + \frac{5}{2}\right) \cdot F_{r + \frac{3}{2}}(\eta)}{\left(r + \frac{3}{2}\right) \cdot F_{r + \frac{1}{2}}(\eta)} - \eta \right] \quad (S4-1)$$

$$n = \frac{1}{e \cdot R_H} = \frac{(2m^* \cdot k_B T)^{\frac{3}{2}}}{3\pi^2 \hbar^3} \cdot \frac{\left(r + \frac{3}{2}\right)^2 \cdot F_{r + \frac{1}{2}}^2(\eta)}{\left(2r + \frac{3}{2}\right) \cdot F_{2r + \frac{1}{2}}(\eta)} \quad (S4-2)$$

$$\mu = \left[\frac{4\pi \hbar^4 C_l}{\sqrt{2} (k_B T)^2 E_{Def}^2 (m^*)^2} \right] \frac{\left(2r + \frac{3}{2}\right) \cdot F_{2r + \frac{1}{2}}(\eta)}{\left(r + \frac{3}{2}\right)^2 \cdot F_{r + \frac{1}{2}}(\eta)} \quad (S4-3)$$

$$L = \left(\frac{k_B}{e}\right)^2 \cdot \left\{ \frac{\left(r + \frac{7}{2}\right) \cdot F_{r + \frac{5}{2}}(\eta)}{\left(r + \frac{3}{2}\right) \cdot F_{r + \frac{1}{2}}(\eta)} - \left[\frac{\left(r + \frac{5}{2}\right) \cdot F_{r + \frac{3}{2}}(\eta)}{\left(r + \frac{3}{2}\right) \cdot F_{r + \frac{1}{2}}(\eta)} \right]^2 \right\} \quad (S4-4)$$

where η , k_B , e , r , R_H , \hbar , C_l , E_{def} , and L are the reduced Fermi level, the Boltzmann constant, the electron charge, the carrier scattering factor ($r = -1/2$ for acoustic phonon scattering), the Hall coefficient, the reduced plank constant, the elastic constant for longitudinal vibrations, the deformation potential coefficient, and the Lorenz number, respectively. Here:

$$C_l = v_l^2 \cdot \rho \quad (S4-5)$$

where v_l is the longitudinal sound velocity and taken as 2884 m s⁻¹ in this study.¹⁷² $F_i(\eta)$ is the Fermi integral expressed as:

$$F_i(\eta) = \int_0^\infty \frac{x^i}{1 + e^{(x-\eta)}} dx \quad (S4-6)$$

To predict the zT enhancement with reduced κ by inducing porous structure, we assume that the pores are uniformly distributed in the Bi_2Te_3 matrix. In this situation, κ_{lp} can be defined as the κ of porous Bi_2Te_3 . Here, experimentally measured κ was utilized. Phonon mean free path Λ_b was calculated as:²⁰⁶

$$\Lambda_b = \frac{3 \cdot \kappa_{lp}}{C_v v_\alpha} \quad (\text{S4-7})$$

where C_v is the volume heat capacity. v_α is the average sound velocity taken as 2147 m s⁻¹.¹⁷²

6. A comprehensive comparison of zT with other state-of-art binary n -type Bi_2Te_3 works

A comprehensive comparison with other state-of-art binary n -type Bi_2Te_3 works can be found from **Fig. S4**, where the achieved zT of 0.97 in our work is listed as one of the highest values reported for binary n -type Bi_2Te_3 .

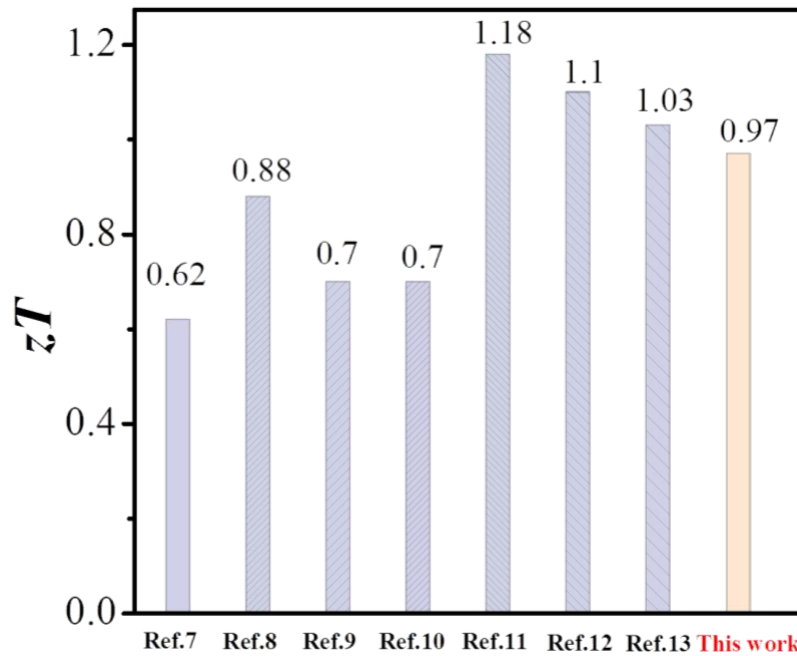


Fig. S4. A comprehensive comparison of zT with other state-of-art binary n -type Bi_2Te_3 works.⁷⁻¹³

Chapter 6 Outstanding $\text{Bi}_{0.5}\text{Sb}_{1.5}\text{Te}_3$ /PEDOT:PSS Flexible Thermoelectric Film and Device *via* Boosted Interfacial Carrier Transport

6.1 Overview

Incorporating inorganic thermoelectric fillers into the conductive polymer matrix serves as one effective strategy to develop high-performance flexible thermoelectric materials, where the system is anticipated to possess decent electrical properties of fillers and low thermal conductivity of polymers. However, due to the high contact resistance of interfaces, interfacial carrier transports are deteriorated, which significantly constrain the optimizations contributed by fillers. To this end, boosting interfacial carrier transports is of vital significance. Additionally, improving the crystallinity of conductive polymers is well believed to render high electrical conductivities. Therefore, simultaneously optimizing interfacial carrier transports and improving the crystallinity of conductive polymers may be one effective strategy to synergistically develop high-performance flexible thermoelectric materials. However, such a promising strategy is never reported previously.

Within our study, optimized interfacial carrier transports and crystallized conductive polymer are simultaneously realized in $\text{Bi}_{0.5}\text{Sb}_{1.5}\text{Te}_3$ /PEDOT:PSS composite, by coating fillers with highly conductive CuTe nano-layer and DMSO- H_2SO_4 double treatments, respectively. Superhigh power factor of $312 \mu\text{W cm}^{-1} \text{K}^{-1}$ is achieved with outstanding electrical conductivity of $\sim 2300 \text{ S cm}^{-1}$, which is a record-high value in the reported $\text{Bi}_{0.5}\text{Sb}_{1.5}\text{Te}_3$ /PEDOT:PSS composites. Additionally, a home-made flexible thermoelectric device is fabricated using our prepared composites, generating a promising open-circuit thermovoltage of $\sim 7.7 \text{ mV}$ with the human wrist as the thermal source. This hints the bright prospects of cheap conductive polymers as the effective power source of wearable electronics.

6.2 Journal publication

The journal publication included in **Chapter 6** is available at *Chem. Eng. J.* **2020**.
<https://doi.org/10.1016/j.cej.2020.125360>.

Superhigh-Performance $\text{Bi}_{0.5}\text{Sb}_{1.5}\text{Te}_3$ /PEDOT:PSS Flexible Thermoelectric Film and Device via Boosted Interfacial Carrier Transport

Yuan Wang,^{a,b} Min Hong,^{a,b} Wei-Di Liu,^b Xiao-Lei Shi,^{a,b} Sheng-Duo Xu,^b Qiang Sun,^b Han Gao,^b Jin Zou,^{b,c} Zhi-Gang Chen^{,a,b}*

^aCentre for Future Materials, University of Southern Queensland, Springfield, Queensland 4300, Australia.

^bSchool of Mechanical and Mining Engineering, The University of Queensland, Brisbane, Queensland 4072, Australia.

^cCentre for Microscopy and Microanalysis, The University of Queensland, Brisbane, Queensland 4072, Australia.

*Corresponding author. Email: zhigang.chen@usq.edu.au (ZGC); zhigang.chen@uq.edu.au (ZGC)

Abstract

Incorporating inorganic thermoelectric fillers into conductive polymers is one promising strategy to develop high-performance flexible thermoelectric films. However, due to the relatively high interfacial contact resistance between fillers and polymers, carriers tend to be scattered at the interfaces during the interfacial transports, which deteriorates the electrical properties of the system, and in turn leads to low energy conversion efficiency. Here, a new strategy is developed to optimize interfacial carrier transports in $\text{Bi}_{0.5}\text{Sb}_{1.5}\text{Te}_3$ /PEDOT:PSS composite, by coating $\text{Bi}_{0.5}\text{Sb}_{1.5}\text{Te}_3$ fillers with highly conductive CuTe layer. With highly crystallized PEDOT:PSS prepared as the matrix, high-performance Cu- $\text{Bi}_{0.5}\text{Sb}_{1.5}\text{Te}_3$ /PEDOT:PSS film is fabricated with promising σ of $\sim 2300 \text{ S cm}^{-1}$ and peak $S_2\sigma$ of $312 \mu\text{W m}^{-1} \text{ K}^{-2}$ at room temperature, which reaches to a record-high value in the reported $\text{Bi}_{0.5}\text{Sb}_{1.5}\text{Te}_3$ /PEDOT:PSS composites. Accordingly, a home-made flexible thermoelectric device is fabricated using our prepared composites, generating a promising open-circuit thermovoltage of $\sim 7.7 \text{ mV}$ with the human wrist as the thermal source. This study addresses the significance of interfacial carrier transport, hinting the bright prospects of cheap conductive polymers as the effective power source of wearable electronics.

Keywords: Thermoelectrics, Flexible, PEDOT:PSS, Bismuth telluride, Interface

1. Introduction

Rapid advances of Internet of Things (IoT) spark the increasing developments of miniature and integrated wearable electronics, where conventional batteries as the power source have the severe disadvantages such as frequent replacements/recharge and extra maintenance.^{99,208} Flexible thermoelectric (FTE) materials enable the direct power generation from heat through the Seebeck effect, and can present conformal interactions with heat sources to maximize heat harvesting, which can therefore act as energy-autonomous, maintenance-free and emission-free power sources for wearable electronics.²⁰⁹ To evaluate the power generation efficiency of FTE materials, a dimensionless figure of merit (zT) is defined as: $zT = S^2\sigma T/\kappa$, where S , σ , κ , and T is the Seebeck coefficient, electrical conductivity, thermal conductivity, and operating temperature, respectively.⁵ Promising zT can thus be effectively contributed by high power factor ($S^2\sigma$) and low κ . Currently, studies on FTE materials mainly focus on conductive polymers, such as poly(3,4-ethylenedioxythiophene)-poly(styrenesulfonate) (PEDOT:PSS),²¹⁰⁻²¹³ poly(3-hexylthiophene-2,5-diyl) (P3HT),^{204,214,215} and polyaniline (PANI),²¹⁶⁻²²⁰ due to their intrinsic flexibility and low κ . However, their poor electrical properties result in inferior $S^2\sigma$ than inorganic TE materials, which restricts their zT improvements. In this regard, optimizing electrical properties of conductive polymers is of vital significance.

So far, several strategies have been used to increase $S^2\sigma$ of conductive polymers. For example, improved σ of PEDOT:PSS can be realized from ordered microstructure or improved crystallinity after polar solvents pre-treatments with dimethyl sulfoxide (DMSO)^{221,222} or ethylene glycol (EG),^{109,223,224} or concentrated H_2SO_4 post-treatments.^{213,225} S can be effectively tuned with controlled oxidation levels of conductive polymers, by means of reducing PEDOT-Tos film in the tetrakis(dimethylamino)ethylene (TDAE) atmosphere,²²⁶ or immersing PEDOT:PSS film in reducing $NaBH_4$,²²⁷ $NaOH$ ²¹⁰ and N_2H_4 ²²⁷ solutions.

Additionally, incorporating inorganic TE fillers into conductive polymers matrix has also been proposed to be an effectively strategy to boost $S^2\sigma$,²²⁸⁻²³² where FTE composites might be synergistically endowed with decent $S^2\sigma$ of inorganic TE fillers and low κ of conductive polymers. So far, FTE composites mainly focus on PEDOT:PSS as the polymer matrix, due to its promising σ of 4380 S cm^{-1} at room temperature,²²⁵ abundance, and facile processability, which may be beneficial for scale-up productions. Inorganic TE fillers mainly include Bi_2Te_3 ^{229,232,233} and $Bi_{0.5}Sb_{1.5}Te_3$ (BST)²²⁸ considering their decent low-temperature $S^2\sigma$, or Te ^{230,234,235} and $SnSe$ ²³⁶ due to their outstanding low-temperature S . Effectively enhanced $S^2\sigma$ of $32.26 \mu\text{W m}^{-1} \text{ K}^{-1}$ has been witnessed from BST/PEDOT:PSS composite, which presents

more than three times higher value than pristine PEDOT:PSS film.²²⁸ In spite of the progress, $S_{2\sigma}$ of FTE composite is still much inferior than inorganic TE materials, possibly caused by the overlook of interfacial carrier transports between fillers and polymers, which significantly restrains contributions of fillers to $S_{2\sigma}$. By applying surface engineering to inorganic fillers, interfacial carrier transports can be optimized, and in turn further boost of $S_{2\sigma}$ becomes possible.^{229,233} Typically, Zhang *et al.*²²⁹ applied HCl rinsing to remove the potential oxidation layer on the surface of *p*-type Bi₂Te₃ filler to optimize interfacial carrier transports, and found significantly increased $S_{2\sigma}$ of 131 $\mu\text{W m}^{-1} \text{K}^{-1}$ in the Bi₂Te₃/PEDOT:PSS film, compared with that of 35.6 $\mu\text{W m}^{-1} \text{K}^{-1}$ without HCl rinsing. Recently, Goo *et al.*²³³ conducted proton-irradiation treatments on the surface of Bi₂Te₃ fillers, which intentionally induced surface defect sites as the extra adsorption sites for polymer chains, and in turn led to intensified interfacial interactions. Consequently, outstanding $S_{2\sigma}$ of 325.3 $\mu\text{W m}^{-1} \text{K}^{-1}$ was achieved in the Bi₂Te₃/PEDOT:PSS film,²³³ which is among the top values of Bi₂Te₃/PEDOT:PSS composites. Therefore, surface engineering of fillers is a promising approach in securing splendid $S_{2\sigma}$ in FTE composites.

In this study, we develop a new strategy to optimize interfacial carrier transports in the BST/PEDOT:PSS composite, by coating BST fillers with highly conductive CuTe layer ($\sigma > 5.2 \times 10^5 \text{ S cm}^{-1}$).²³⁷ With highly crystallized PEDOT:PSS prepared as the matrix, superhigh-performance Cu-BST/PEDOT:PSS film was fabricated and showed promising σ of 2270 S cm^{-1} and peak $S_{2\sigma}$ of 312 $\mu\text{W m}^{-1} \text{K}^{-1}$ at room temperature, which reached to state-of-the-art values reported for BST/PEDOT:PSS composites.^{228,229,238,239} **Figure 1** schematically depicts the fabrication process of the composites, where fillers and polymers are separately prepared. Cu-BST fillers were synthesized by a facile electroless plating method.^{154,157} Crystallized PEDOT:PSS was obtained through DMSO polar solvent pre-treatments, followed by concentrated H₂SO₄ post-treatment to selectively remove insulating PSS, which in turn render increased σ . Finally, the BST/PEDOT:PSS film with decent flexibility was fabricated by drop casting TE ink onto pre-cleaned glass substrate. A home-made FTE device was fabricated accordingly, showing the effective power generation with human wrist as the thermal source.

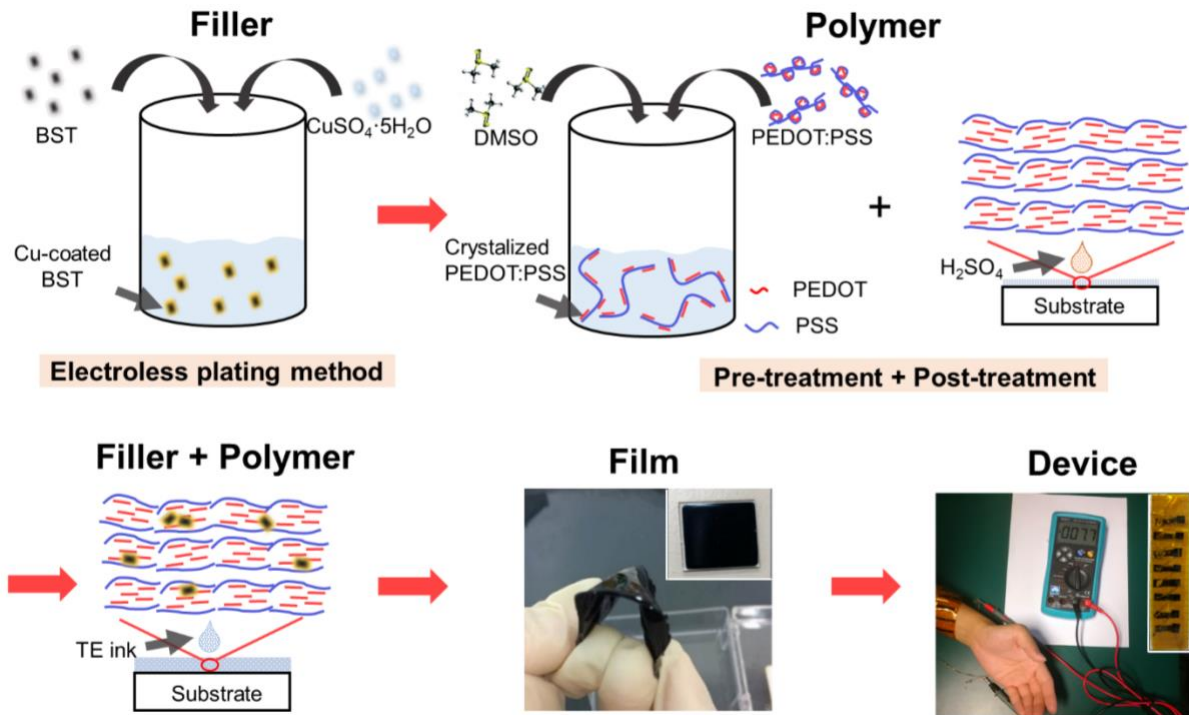


Figure 1. Schematic illustration of the processes to fabrication Cu-BST/PEDOT:PSS FTE films and device.

Results and Discussion

Figure 2 shows the structural characterizations of BST fillers before and after Cu coating. **Figure 2a** is XRD patterns taken from BST, 0.05 wt.% Cu-BST and 0.1 wt.% Cu-BST fillers, respectively. As can be seen, the diffraction peaks of the as-synthesized BST powders can be exclusively indexed as hexagonal structured BST with lattice parameters of $a = 4.28424$ nm and $c = 30.52389$ nm and a space group of $R\bar{3}m$ (PDF#49-1713). After Cu coating, additional peaks at 2θ of 12.8° , 25.4° and 31.1° emerge in the diffraction peaks of 0.05 wt.% Cu-BST, which can be precisely retrieved as orthorhombic structured CuTe with lattice parameters of $a = 3.16$ nm, $b = 4.08$ nm and $c = 6.93$ nm and a space group $Pmmn$ (PDF#22-0252). This indicates that Cu reacts with BST particles during the coating process to form CuTe. **Figure 2b** shows the EDS results, and further confirms the successful coating of Cu on the surface of BST particles, where Cu is detected from EDS spot analysis and clearly observed on the boundaries of BST particles from the EDS maps. **Figure 2c-g** are TEM results to clarify the insights of the coating process. As can be seen, the uncoated BST particles (**Figure 2c**) show relatively smooth boundaries, while zig-zag boundaries appear in the coated BST particles (**Figure 2d**), which is attributed to the HNO_3 pre-treatments to generate sufficient reaction sites for maximum Cu coating. As verified in **Figure 2d** and **e**, CuTe is clearly observed on BST

boundaries, which is consistent with SEM EDS maps, shown in **Figure 2b**. **Figure 2e** shows typical high-resolution TEM image, in which the as-coated CuTe layer is relatively uniform with a thickness of 17 nm. **Figure 2f** is its corresponding high-angle annular dark-field (HAADF) image of the interface, where the CuTe layer with small atomic mass shows dark contrast compared with the bright contrast of the BST particle. **Figure 2g** is a zoom-in high-resolution TEM (HRTEM) image taken from the CuTe layer (highlighted by red square in **Figure 2e**), in which two sets of lattice planes with d -spacing of 0.18 and 0.23 nm can be detected with the angle of 50.3° that correspond to the (022) and (102) atomic planes of CuTe, respectively.

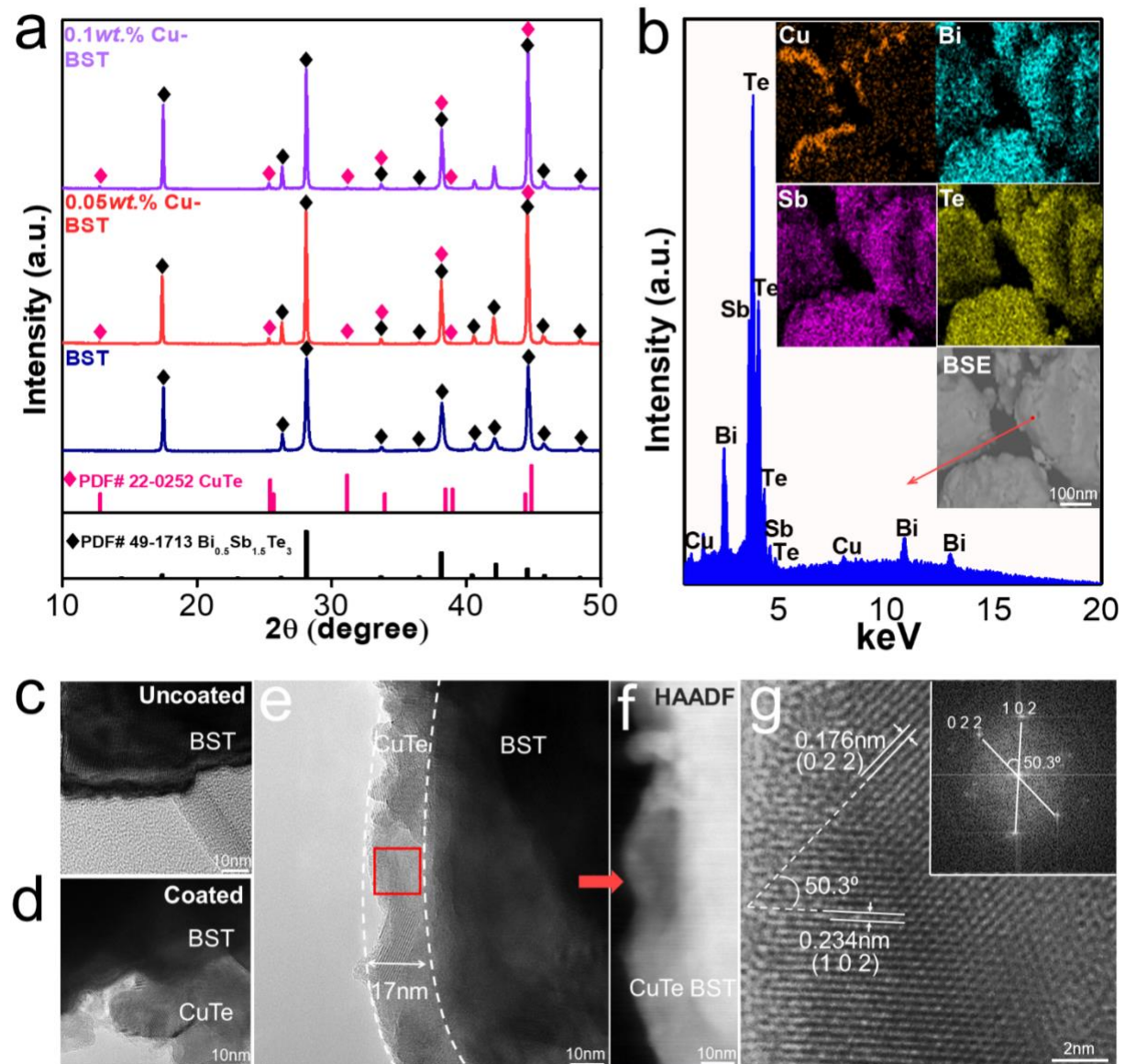


Figure 2. (a) XRD patterns of BST, 0.05 wt.% Cu-BST and 0.1 wt.% Cu-BST fillers. (b) EDS spot spectrum of 0.1 wt.% Cu-BST fillers with the inset of mapping results of Cu, Bi, Sb and

Te. Typical high-magnitude TEM images of BST fillers (c) before and (d) (e) after Cu coating, together with corresponding (f) HAADF and (g) HRTEM images.

It has been reported that high crystallinity of PEDOT:PSS can lead to high σ_{225} while selectively removal of insulating PSS can induce improved crystallinity of PEDOT:PSS.²⁴⁰ Here, we applied DMSO-H₂SO₄ double treatments to effectively remove insulating PSS and in turn result in highly crystallized PEDOT:PSS. **Figure 3a** shows XRD patterns of PEDOT:PSS films before and after the treatments. Pristine film shows weak peaks at low 2θ of 3.3 and 7° corresponding to the lamella stacking of alternate PEDOT and PSS along the (100) plane, and high 2θ of 18 and 26°, which can be attributes to amorphous PSS and inter-chain planar stacking along the (010) planes.²⁴¹ The weak intensities of all diffraction peaks indicate the amorphous microstructure and low crystallinity of pristine PEDOT:PSS film. These form a sharp contrast with DMSO-H₂SO₄ treated PEDOT:PSS film, where two sharp diffraction peaks at ~7 and 12.5° indicate that (100) stacking has been greatly intensified after the treatment. Moreover, it should be noted that two peaks of (100) stacking both exhibit an obvious right peak shift after the treatment, which is from the original 2θ of 3.3 and 7° to ~7 and 12.5°, respectively. According to Bragg's law,²¹³ this hints the shrink of spacing between (100) stackings, which confirms the effectively removal of insulating PSS. On the other hand, two peaks of (010) planes stacking are still quite weak after the treatment, and present ignorable intensities compared with two peaks of (100) stacking. This means (100) stacking dominates in the microstructure of treated film, which contributes to highly crystallized PEDOT:PSS. Increased crystallinity of PEDOT:PSS is also associated with chemical structure transition of PEDOT monomers from benzoid to quinoid after DMSO-H₂SO₄ double treatments,^{242,243} as shown in **Figure 3a**. PEDOT monomers with benzoid structure are connected by relatively flexible C-C bonds, which tend to induce deviations of adjacent thiophene rings and formation of coiled-up conformation.²⁴⁴ However, PEDOT monomers with quinoid structure are connected by rigid π bonds (C=C bonds), which is favoured by flat PEDOT backbones and in turn enhanced crystallinity.²⁴³ Cross-sectional SEM images of PEDOT:PSS films of **Figure 3b** further confirm the improved crystallinity, where lamella stacking is clearly visible after the treatment. Additionally, the decreased thickness of film from 4 to 2.5 μm verifies the PSS depletion.

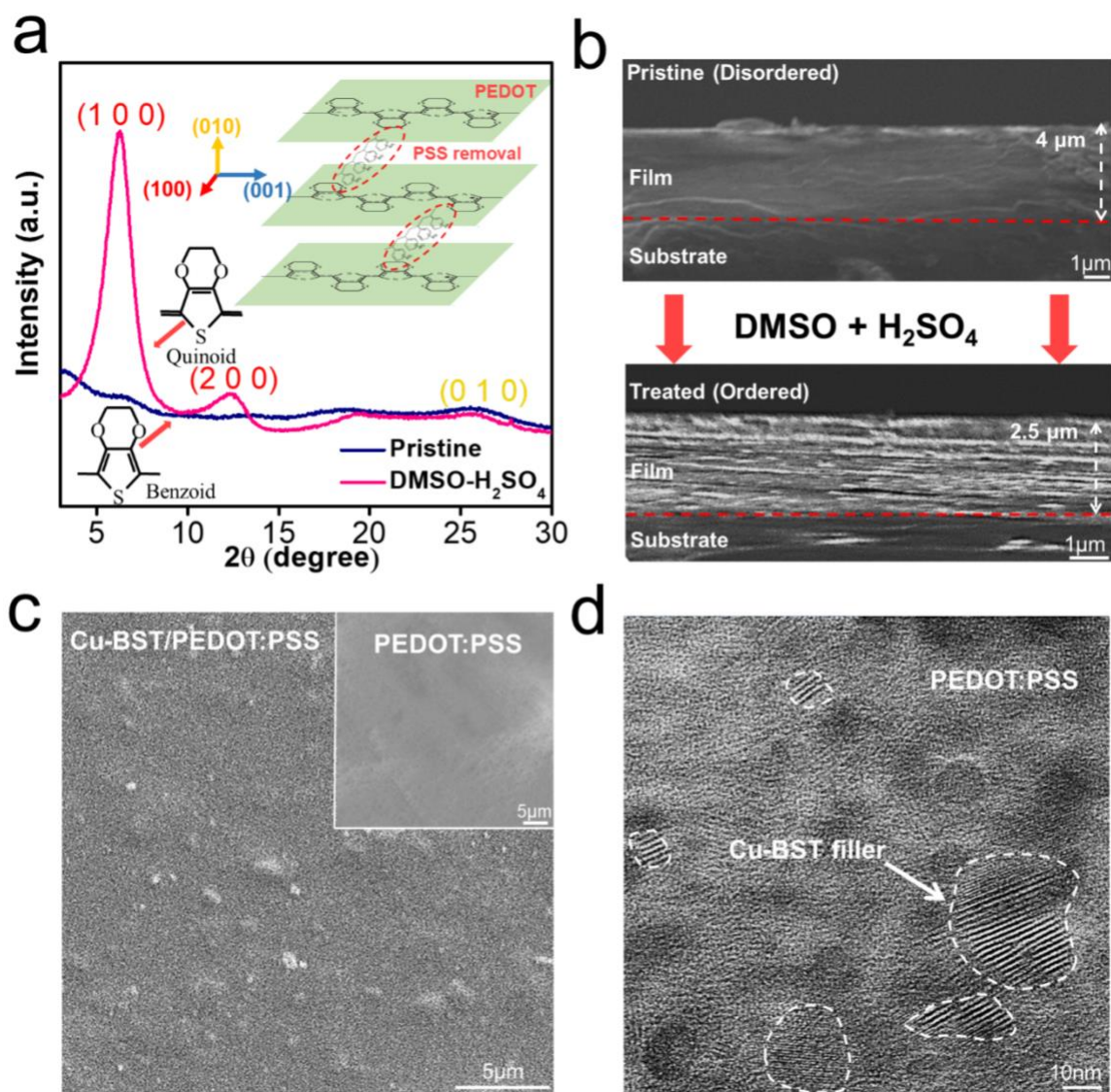


Figure 3. (a) XRD patterns and (b) cross-sectional SEM images of PEDOT:PSS films before and after DMSO-H₂SO₄ double treatments. (c) Typical top-view SEM and (d) TEM images of PEDOT:PSS films with 6 wt.% Cu-BST filler incorporation, with the inset of (c) showing PEDOT:PSS film without fillers.

With Cu-coated BST fillers and crystallized PEDOT:PSS conductive polymer, Cu-BST/PEDOT:PSS film was fabricated. **Figure 3c** shows the typical top-view SEM image of the film, with the inset of PEDOT:PSS film without fillers. Relatively uniform dispersion of fillers can be observed, and the introduction of fillers result in the improved roughness of the films. **Figure 3d** is a TEM image, and further confirms the well dispersion of fillers. Moreover, PEDOT:PSS is observed to closely envelop Cu-BST fillers, which can be beneficial to optimize the interfacial carrier transport.

Figure 4 plots the room-temperature σ and S of the as-fabricated films. **Figure 4a** shows DMSO-H₂SO₄ treated PEDOT:PSS films, in which decent σ of 1815 S cm⁻¹ is achieved, which is ascribed to the as-obtained high crystallinity, and this value agrees with reported crystalline PEDOT:PSS.^{213,225} With filler incorporations, it is found that pristine BST fillers can deteriorate σ , showing values lower than treated PEDOT:PSS films. On one hand, this may be due to the lower σ value of pristine BST fillers (~ 500 S cm⁻¹, **Figure S1a**) than treated PEDOT:PSS. On the other hand, the surface of pristine BST fillers can potentially scatter carriers during the transport due to the relatively high interfacial contact resistance, which leads to the depressed carrier mobility (μ) and in turn low σ .

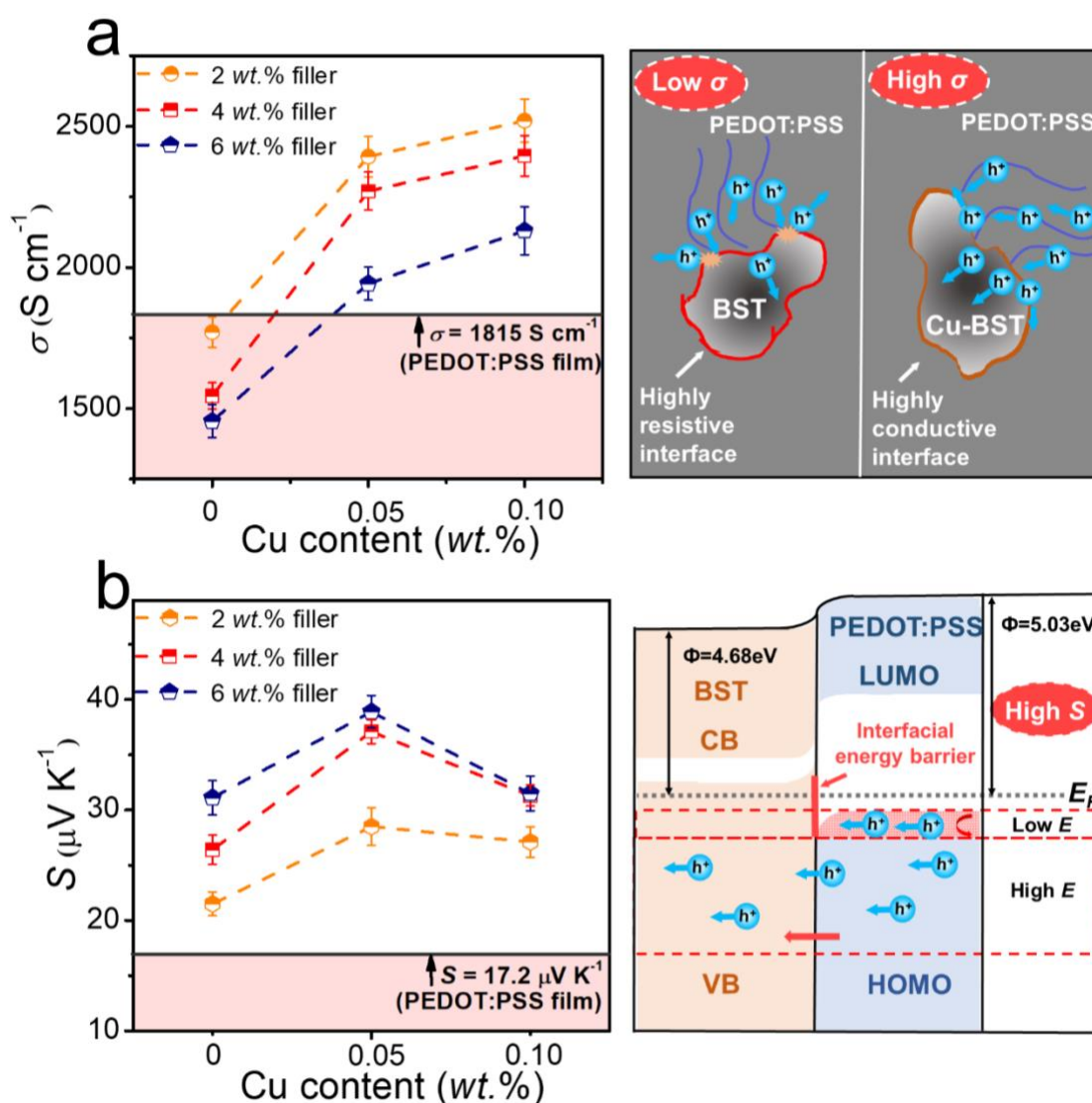


Fig. 4. Measured room-temperature (a) σ and (b) S of PEDOT:PSS films incorporated with BST fillers before and after Cu coatings (filler content 2 wt.%, 4 wt.% and 6 wt.%), corresponding schematics are shown on the right.

With introducing highly conductive CuTe interfacial layers, σ can be significantly enhanced and exceed that of treated PEDOT:PSS films under various filler contents. Such a tendency is more obvious with increasing the Cu coating, and an outstanding σ value of 2520 S cm⁻¹ is achieved in the 0.1 wt.% Cu-BST/PEDOT:PSS film with 2 wt.% filler content. Such a σ improvement can be attributed to high σ value of the CuTe layers ($\sigma > 5.2 \times 10^5$ S cm⁻¹),²³⁷ as well as the optimized interfacial carriers transport, as schematically depicted on the right of **Figure 4a**. In contrast to the carrier blocking effect induced by pristine BST fillers, highly conductive CuTe interfacial layers can render carriers to travel within CuTe layers or through BST fillers, rather than being scattered. In this way, optimized interfacial carriers transport with improved μ is generated, which is favourable by high σ .

Table 1. n and μ of BST/PEDOT:PSS films before and after Cu coatings (4 wt.% filler).

Parameter	BST/PEDOT:PSS	0.05 wt.% Cu-BST/PEDOT:PSS	0.1 wt.% Cu-BST/PEDOT:PSS
μ (cm ² V ⁻¹ s ⁻¹)	13.72±1.96	18.04±2.21	18.82±2.82
n (10 ²⁰ cm ⁻³)	8.06±1.21	8.29±1.24	8.37±1.19

Hall measurements are applied to investigate the change of μ before and after Cu coatings, and **Table 1** summarizes the results. Effective increases of μ occur from ~13.72 to ~18.04 and ~18.82 cm² V⁻¹ s⁻¹ after 0.05 wt.% and 0.1 wt.% Cu coatings, respectively. These are consistent with aforementioned claims and should be responsible for boosted σ . Additionally, high filler contents are found to cause low σ . This agrees with other reports,^{113,245} and stems from more introduced interfaces between polymers and fillers.

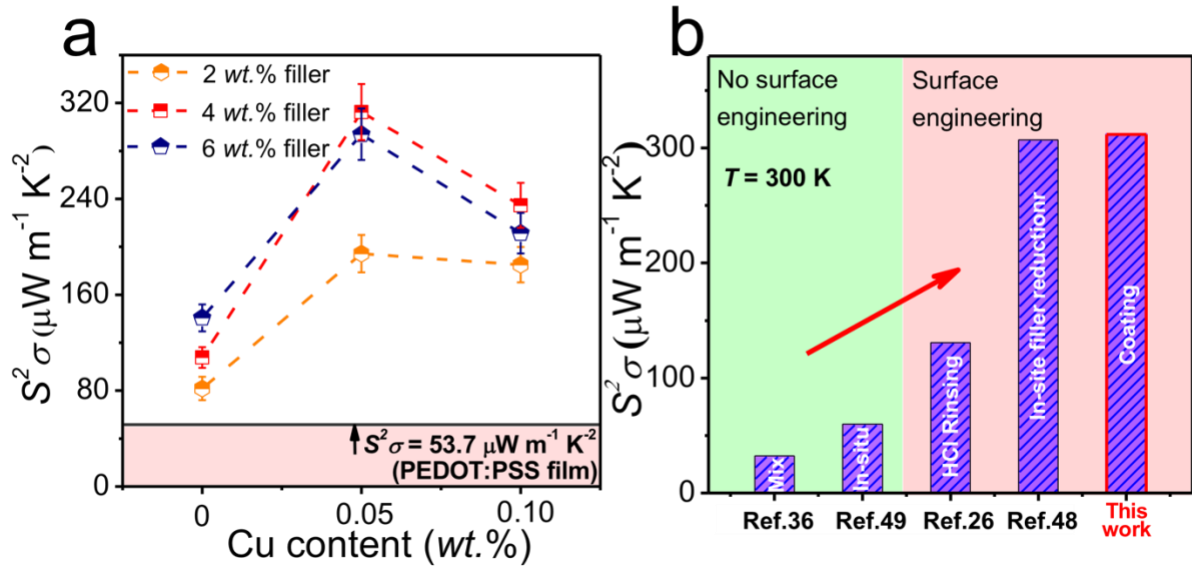


Fig. 5. (a) Measured room-temperature $S^2\sigma$ of PEDOT:PSS films incorporated with BST fillers before and after Cu coatings (filler content 2 wt.%, 4 wt.% and 6 wt.%). (b) Comparisons of $S^2\sigma$ between this work and other BST/PEDOT:PSS works,^{229,239,246,247} where the potentials of filler surface engineering is visible.

In terms of S , **Figure 4b** shows that additions of fillers before and after Cu coatings both show positive effects. Peak S of $38.9 \mu\text{V K}^{-1}$ can be achieved from 0.05 wt.% Cu-BST/PEDOT:PSS films with 6 wt.% filler content. The S improvement is contributed by the interfacial energy filtering effect,^{248,249} as shown in the schematic diagram of **Figure 4b**. With the interfacial energy offset existing between PEDOT:PSS and BST fillers, an interfacial energy barrier can be formed between the highest occupied molecular orbital (HOMO) of PEDOT:PSS and valance band (VB) of BST fillers. Carriers (holes) with relatively low energy tend to be scattered at the interfaces while those with high energy pass through. Therefore, the average energy of system carriers is improved, which is favoured by high S .²⁴⁹ On the other hand, it should be noted that Cu-BST fillers (both 0.05 wt.% and 0.1 wt.%) possess more obvious boost towards S compared with BST fillers. This may be because introduced CuTe layers allow more carriers transport through BST fillers, inducing more sufficient interfacial energy filtering.

With the measured σ and S , $S^2\sigma$ is calculated and plotted in **Figure 5a**. The $S^2\sigma$ enhancement induced by Cu coating is evident, and an outstanding $S^2\sigma$ value of $312 \mu\text{W m}^{-1} \text{K}^{-2}$ can be observed in the 0.05 wt.% Cu-BST/PEDOT:PSS film with 4 wt.% filler content, which exhibits almost six times improvements than our treated PEDOT:PSS film. Compared with other BST/PEDOT:PSS FTE works,^{229,239,246,247} **Figure 5b** shows the outstanding performance of

our strategy, in which significant $S_2\sigma$ enhancement is obtained after considerations of interfaces, manifesting surface engineering of fillers.

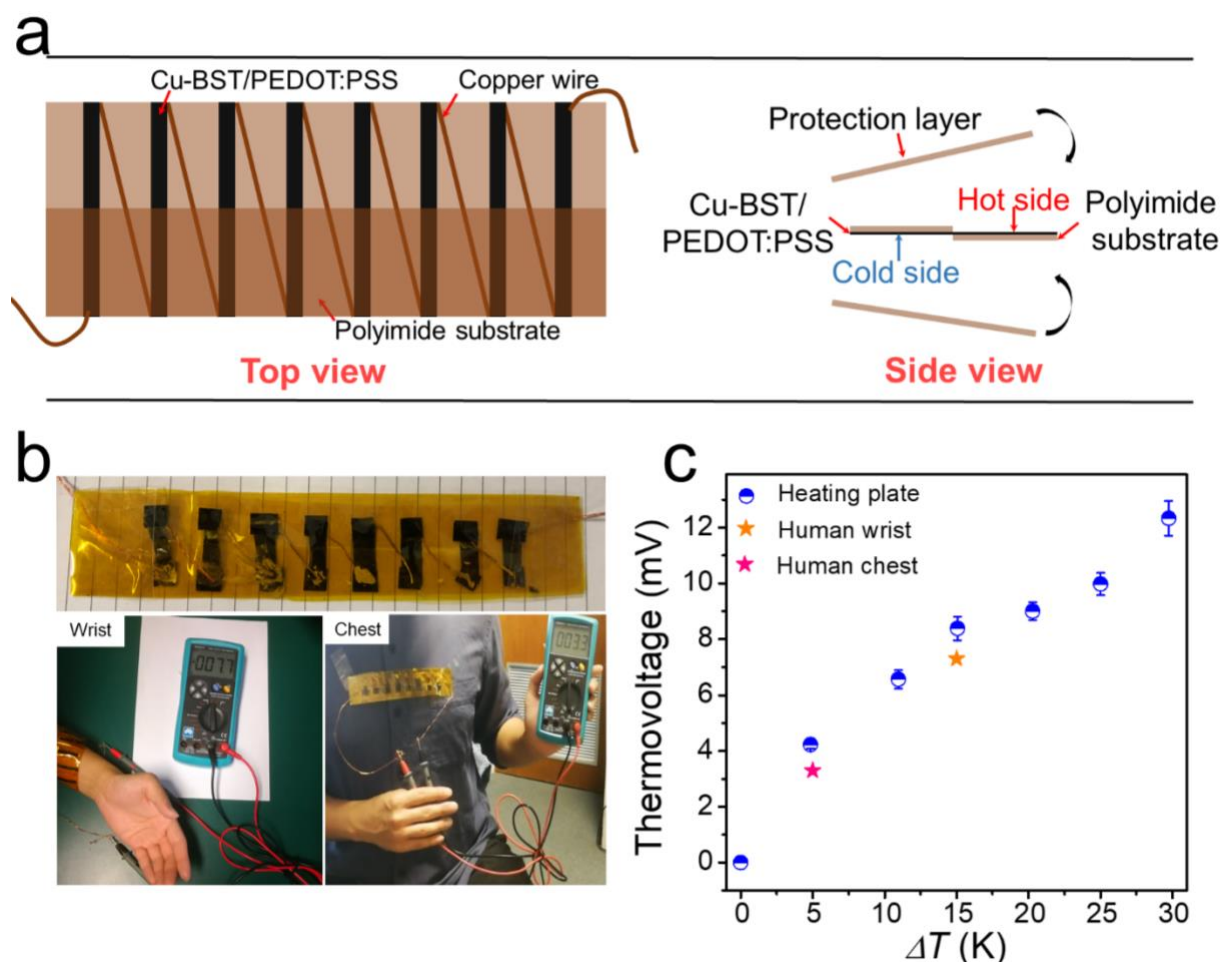


Figure 6. (a) Schematic diagram of a home-made FTE device. (b) Images of the as-fabricated FTE device, and its thermovoltage generations with human wrist and chest as thermal sources. (c) Measured thermovoltages using heating plate, human wrist and chest as thermal sources.

To confirm the potentials of power generation using the as-prepared Cu-BST/PEDOT:PSS films, a home-made FTE device was fabricated based on the structure shown in **Figure 6a**. TE legs with the size of $25 \times 8 \text{ mm}^2$ were assembled into the flexible polyimide substrate and connected by copper wires. Another two polyimide films were applied as the protection layer to cover top and bottom of TE legs. **Figure 6b** shows the as-fabricated FTE device, where thermovoltages can be effectively generated when attaching the device onto human wrist and chest. By firmly attaching one end of the device onto the heating plate and exposing the other end in the air, more temperature differences can be achieved from 5 to 30 K, generating increased thermovoltages, as shown in **Figure 6c**. Peak thermovoltage of $\sim 12.3 \text{ mV}$ can be realized with 30 K temperature difference between two ends of the device. It should be noted

that heating plate as the thermal source can contribute slightly higher voltages than human body. This should be due to the heat loss occurred at the interface between human skin and the device, leading to the reduced temperature differences and in turn deteriorated voltage generations.

Conclusion

In summary, we fabricated superhigh-performance Cu-BST/PEDOT:PSS FTE films by coating BST fillers with highly conductive CuTe layer ($\sigma > 5.2 \times 10^5 \text{ S cm}^{-1}$) and preparing highly crystallized PEDOT:PSS conductive polymer. High σ of 2270 S cm^{-1} was achieved, which is attributed to the boosted interfacial carriers transport and crystallized PEDOT:PSS. Meanwhile, S was enhanced by interfacial energy filtering, reaching value up to $37.1 \mu\text{V K}^{-1}$. Systematic XRD, EDS, SEM and TEM results confirm the successful introduction of nanoscale CuTe layers and accomplishment of highly crystallized PEDOT:PSS. Effectively improved σ of the system after Cu coating manifests the optimization of interfacial carriers transport, which is further supported by Hall measurement results. As a result, an outstanding $S_2\sigma$ value of $312 \mu\text{W m}^{-1} \text{ K}^{-2}$ was realized at the room temperature, which serves as a state-of-the-art value for BST/PEDOT:PSS FTE composites. Meanwhile, a FTE device was fabricated using the as-prepared Cu-BST/PEDOT:PSS films, generating a promising open-circuit thermovoltage of $\sim 7.7 \text{ mV}$ with human wrist as the thermal source.

Experimental Section

Materials

Analytical grade Bi shots (99.999%), Sb shots (99.999%), Te shots (99.999%) and NaOH (99.999%) were purchased from Alfa-Aesar (United States) and used without any further purifications. PEDOT:PSS aqueous solution (Clevios PH1000) was purchased from Heraeus (Germany). Dimethyl sulfoxide (DMSO), concentrated H_2SO_4 (98%), concentrated HNO_3 (98%), copper sulfate pentahydrate, formaldehyde, Ethylenediaminetetraacetic acid disodium salt (EDTA-2Na) and polyvinylidene difluoride (PVDF) membrane filter (0.45 μm pore size) were all purchased from Sigma-Aldrich (Australia).

Synthesis of Cu-coated BST fillers

High-purity Bi shots (99.999%), Sb shots (99.999%) and Te shots (99.999%) were weighted based on the nominal composition of BST, and subsequently sealed into a quartz tube under the vacuum of 10^{-3} Pa . The quartz tube was then placed in the furnace, where the precursors were melted and kept for 10 h at 1023 K. As-synthesized BST ingot was finally ball-milled (AXT, 8000M) for 20 min under 15 Hz in order to obtain fine BST fillers.

As-prepared BST fillers were then coated with Cu using facile electroless plating method. Specifically, BST fillers were firstly sonicated in 5% HNO₃ solution for 1 h, followed by deionized water rinsing for at least three times to remove residual impurities. Afterwards, pretreated BST fillers were transferred into the coating solution consisting of copper sulfate pentahydrate as the copper source, formaldehyde as the reducing agent, EDTA-2Na as the complex agents and NaOH to provide the alkaline environment. The coating process was conducted under the sonication and lasted for 1 h at 330 K. The as-coated BST fillers were alternatively washed by deionized water and ethanol for at least three times, before being collected by centrifugation and dried at 330 K in the oven overnight. The as-collected Cu-BST fillers were ultimately reduced under H₂ atmosphere at 580 K for 1 h, and naturally cooled down to the room temperature. The as-reduced Cu-BST fillers were sealed in the vacuum and ready for the next step.

Treatments of PEDOT:PSS conductive polymers

Aqueous solution PEDOT:PSS was firstly mixed with 10 vol.% polar solvent DMSO and sonicated for 6 h at 330 K. The solution was then filtered by PVDF membrane (0.45 μm pore size) using vacuum-assisted filtration method to remove insulating and hydrophilic PSS. The filtrate was collected and magnetically stirred until forming the PEDOT:PSS slurry, which was subsequently drop casted onto pre-cleaned silicon dioxide substrates, and later dried at 330 K for 20 min on the heating plate. PEDOT:PSS films were then immersed into concentrated H₂SO₄ (98%) for 10 h to further remove insulating PSS, and rinsed with deionized water for three times afterwards. The as-treated PEDOT:PSS films were lastly magnetically stirred into PEDOT:PSS slurry, which was ready for the film fabrication.

Fabrication of Cu-BST/PEDOT:PSS films

Silicon dioxide substrates were pre-cleaned following the sequence of detergent, deionized water, ethanol and plasma cleaning. PEDOT:PSS slurry was mixed with different amount of Cu-BST fillers (2 wt.%, 4 wt.% and 6 wt.%) and sonicated for 6 h, followed by intense magnetic stirring for another 6 h at room temperature to obtain uniform Cu-BST/PEDOT:PSS inks. BST fillers without Cu coating were also mixed with PEDOT:PSS slurry following above processes as the contrast set. 100 μL ink was subsequently drop casted onto pre-cleaned silicon dioxide substrates, and later dried at 330 K for 20 min on the heating plate. The as-fabricated films were collected and showed decent flexibility.

Fabrication of FTE device

10 milliliters of as-prepared inks was paved in the glass petri dish with the diameter of 55 mm. After drying at 330 K for 2 hours, as-fabricated film was immersed in ethanol to detach from

the glass petri dish. Free-standing Cu-BST/PEDOT:PSS films were obtained by collecting detached film and drying at 330 K for 20 min. As-obtained films were cut into rectangular pieces with the size of $25 \times 8 \text{ mm}^2$, which were subsequently connected by copper wires and assembled into FTE device using polyimide as the substrate. Two polyimide films were lastly used to cover top and bottom of the FTE device, acting as the protection layer.

Measurements and characterization

Electrical properties of as-fabricated films, including σ and S , were measured by SBA458 (Netzsch) at 300 K. X-ray diffraction (XRD, Bruker-D8) was applied to determine the crystal structure of BST fillers before and after Cu coatings. Grazing incidence XRD (GIXRD, Rigaku SmartLab) was utilized to investigate the crystallinity of conductive polymers before and after treatments. Scanning electron microscopy (SEM, JEOL JSM-7100F) and transmission electron microscopy (TEM, TECNAI-F20) were utilized to study the morphology and structural characteristics. X-ray energy-dispersive spectroscopy (EDS) mapping and spot analysis (equipped in HITACHI-SU3500 SEM) were conducted to confirm the successful surface coating of Cu on the BST fillers.

Supporting Information

Supporting Information is available from the Wiley Online Library or from the author.

Acknowledgements

This work was financially supported by the Australian Research Council. ZGC thanks the USQ start-up grant and strategic research grant. Microscopy Australia is acknowledged for providing characterization facilities.

Received: ((will be filled in by the editorial staff))

Revised: ((will be filled in by the editorial staff))

Published online: ((will be filled in by the editorial staff))

Supporting Information

Outstanding $\text{Bi}_{0.5}\text{Sb}_{1.5}\text{Te}_3$ /PEDOT:PSS Flexible Thermoelectric Film and Device *via* Boosted Interfacial Carrier Transport

Yuan Wang,^{a,b} Min Hong,^{a,b} Wei-Di Liu,^b Xiao-Lei Shi,^{a,b} Sheng-Duo Xu,^b Qiang Sun,^b Han Gao,^b Jin Zou,^{b,c} Zhi-Gang Chen^{,a,b}*

^aCentre for Future Materials, University of Southern Queensland, Springfield, Queensland 4300, Australia.

^bSchool of Mechanical and Mining Engineering, The University of Queensland, Brisbane, Queensland 4072, Australia.

^cCentre for Microscopy and Microanalysis, The University of Queensland, Brisbane, Queensland 4072, Australia.

*Corresponding author. Email: zhigang.chen@usq.edu.au (ZGC); zhigang.chen@uq.edu.au (ZGC)

Electrical properties of $\text{Bi}_{0.5}\text{Sb}_{1.5}\text{Te}_3$ fillers before and after Cu coating

In order to investigate electrical properties of $\text{Bi}_{0.5}\text{Sb}_{1.5}\text{Te}_3$ fillers before and after Cu coatings, as-synthesized powders were sintered into pellets with the diameter of 12 mm using spark plasma sintering technique, and the results are shown in **Figure S1**.

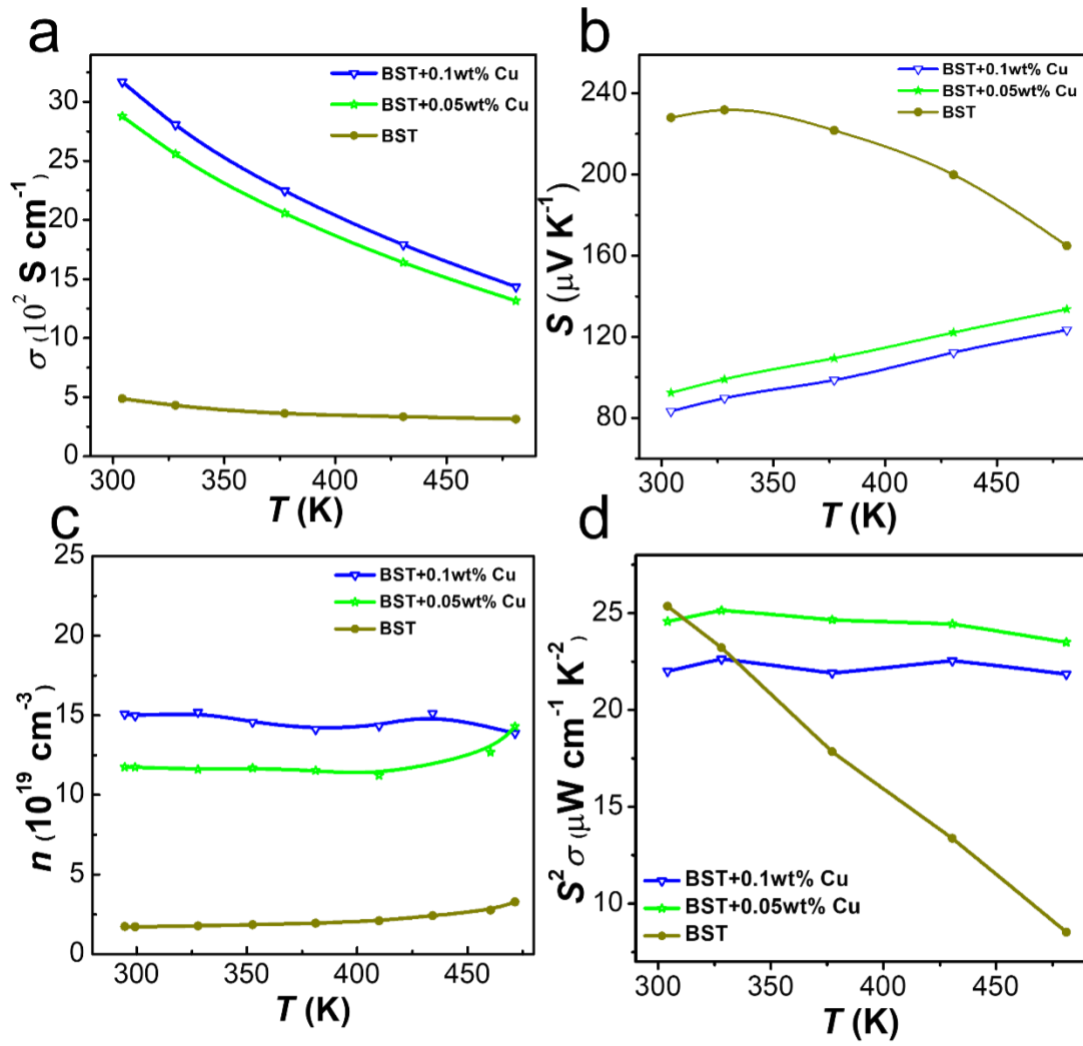


Fig. S1. T -dependant (a) σ , (b) S , (c) n , and (d) $S^2\sigma$ of BST fillers before and after Cu coatings (0.05 wt.% Cu and 0.1 wt.% Cu).

Chapter 7: Conclusions and Perspectives

7.1 Conclusions

This PhD project aims to develop Bi₂Te₃-based multi-dimensional thermoelectric materials for highly efficient wearable electronics powering at the low temperature. By understanding various thermoelectric parameters and their underlying relationships, high-performance Bi₂Te₃-based thermoelectric pellets and films were developed by employing nanostructure, texture, point defect and interfacial engineering, as well as the theoretical modelling. Some innovative strategies have been proposed to optimize thermoelectric performances, including realizing ultralow lattice thermal conductivity from porous and nanostructured Bi₂Te₃ pellet, modulating the carrier concentration of Bi₂Te₃ pellet towards predicted optimal value through non-equilibrium reactions, and boosting the interfacial carriers transport of Bi_{0.5}Sb_{1.5}Te₃/PEDOT:PSS flexible thermoelectric films by decorating Bi_{0.5}Sb_{1.5}Te₃ fillers with highly conductive layers. These studies push our results to state-of-the-art Bi₂Te₃-based thermoelectric performances, and lead several publications in internationally prestigious journals including *Advanced Materials*, *ACS Applied Materials & Interfaces* and *Chemical Engineering Journal*. Importantly, our studies might inspire other relevant studies in the thermoelectric community. The conclusions from this PhD project are summarized in the following.

(1) Modulations of the carrier concentration in nanostructured *n*-type Bi₂Te₃ pellet are realized by non-equilibrium fast reactions induced by SPS, where *n* is tuned to approach the optimal value calculated by SPB model. By systematic XRD, EPMA and EDS investigations, Te vacancies are found to be effectively suppressed, leading reduced *n* from pristinely $\sim 1 \times 10^{20}$ to $\sim 6 \times 10^{19}$ cm⁻³ and generating a decent $S_2\sigma$ of 12.84 $\mu\text{W cm}^{-1} \text{K}^{-2}$ at 320 K. Meanwhile, the decreased κ_e due to deteriorated σ enabled a very low κ of 0.48 W m⁻¹ K⁻¹, which ultimately secured a promising zT of ~ 1.1 at 420 K and an outstanding average zT of ~ 1 from 320 to 470 K.

(2) Achievement of ultralow κ_l in nanostructured *n*-type Bi₂Te₃ pellet is realized by introducing the porous structure. By comprehensive XRD, XPS, EPMA and EDS studies, the mechanism of pore generation is revealed and ascribed to the sublimations of Bi₂TeO₅ during the sintering process. SEM and TEM further confirm homogeneously distributed pores and dense grain boundaries in the Bi₂Te₃ matrix, which cause strong phonon scatterings. As a result, an ultralow

κ_l of $< 0.1 \text{ W m}^{-1} \text{ K}^{-1}$ was achieved. With the well-maintained decent $S_2\sigma$ of $10.57 \mu\text{W cm}^{-1} \text{ K}^{-2}$, a promising zT value of 0.97 was secured at 420 K.

(3) Interfacial carriers transport in $\text{Bi}_{0.5}\text{Sb}_{1.5}\text{Te}_3/\text{PEDOT:PSS}$ flexible thermoelectric films is optimized by coating $\text{Bi}_{0.5}\text{Sb}_{1.5}\text{Te}_3$ fillers with highly conductive CuTe layer, using facile electroless plating method. The successful coating of CuTe layer is confirmed by XRD, TEM and EDS mapping results. Hall and electrical properties measurements further manifest the boost of interfacial carriers transport, where highly conductive CuTe layer can render carriers to travel within CuTe layers or through $\text{Bi}_{0.5}\text{Sb}_{1.5}\text{Te}_3$ fillers, rather than being scattered. Meanwhile, XRD and SEM studies evidence the fabrication of highly crystallized conductive polymer PEDOT:PSS with microstructure of lamella stacking prepared by DMSO- H_2SO_4 double treatments, where insulating PSS was effectively depleted. Optimized interfacial carrier transports and highly crystallized PEDOT:PSS synergistically contributed to significant boost of μ from pristinely ~ 0.77 to $\sim 18.82 \text{ cm}^2 \text{ V}^{-1} \text{ s}^{-1}$, resulting in a promising room-temperature σ of $\sim 2300 \text{ S cm}^{-1}$ and outstanding $S_2\sigma$ of $312 \mu\text{W m}^{-1} \text{ K}^{-2}$ in $\text{Bi}_{0.5}\text{Sb}_{1.5}\text{Te}_3/\text{PEDOT:PSS}$ flexible thermoelectric films. Accordingly, a home-made flexible thermoelectric device was fabricated using as-prepared composites, generating a promising open-circuit thermovoltage of $\sim 7.7 \text{ mV}$ with the human wrist as the thermal source.

7.2 Perspectives

Bi_2Te_3 -based thermoelectric materials act as the best low-temperature thermoelectric materials holding great promises to power wearable electronics by harvesting human body heat. With the integration and miniaturization of wearable electronics, developing both Bi_2Te_3 -based thermoelectric pellets and films are of vital significance. Perspectives to develop high-performance Bi_2Te_3 -based thermoelectric materials and devices are given as below.

(1) Point defects manipulations. Point defects widely exist in Bi_2Te_3 -based thermoelectric materials, playing a significant role to affect carriers and phonons transports. In some way, the significance of point defects manipulation is on par with extrinsic dopants introductions. However, current studies lack the insight of formation mechanisms of point defects, and their manipulations are not quantitative and sometimes not reproducible. Obtaining deep understandings of point defects, and exploring a stable and accurate manipulation method is highly desired.

(2) Understanding and optimizing the effects of fillers through interfacial engineering. Introduction of fillers induces novel effects at the interfaces, which significantly affect carrier interfacial transport. Insights into their mechanisms can guide filler selection and processing.

For example, by rationally matching the Fermi levels of conductive polymers and fillers, the interfacial energy-filtering effect can be modulated to optimize $S_2\sigma$. Furthermore, an oriented distribution of fillers can potentially boost electrical performance, especially for anisotropic fillers.²⁵⁰ Ambient electrical or magnetic fields, in this case, are promising during film fabrication. This is because fillers such as van der Waals 2D crystals have been reported to possess intrinsic ferromagnetism, which may be facily ordered under magnetic fields.^{251,252}

(3) Matching thermal resistances between heat sources and thermoelectric devices, as well as overcoming the mechanical inflexibility of inorganic thermoelectric legs in flexible thermoelectric devices. In order to match heat sources, the thermal resistance of FTE devices can be adjusted by optimizing device dimensions and geometry,²⁵³ where finite element analysis could be effective in predicting corresponding thermal resistances.²⁵⁴ By combining microscale inorganic thermoelectric legs into flexible substrates, microfabrication might be an effective way to overcome the mechanical inflexibility of inorganic thermoelectrics in flexible thermoelectric devices.²⁵⁵ Finally, since most recent studies focus on harvesting thermal energy to generate electricity, devices aiming for FTE cooling effects deserve future investigation.^{256,257}

Reference

- (1) Mukhopadhyay S.C. *IEEE Sens. J.* **2015**, *15*, 1321-1330.
- (2) Proto A.; Penhaker M.; Conforto S.; Schmid M. *Trends Biotechnol.* **2017**, *35*, 610-624.
- (3) Stoppa M.; Chiolerio A. *Sensors* **2014**, *14*, 11957-11992.
- (4) Bahk J.-H.; Fang H.; Yazawa K.; Shakouri A. *J. Mater. Chem. C* **2015**, *3*, 10362-10374.
- (5) Chen Z.-G.; Han G.; Yang L.; Cheng L.; Zou J. *Progress in Natural Science: Materials International* **2012**, *22*, 535-549.
- (6) Moshwan R.; Yang L.; Zou J.; Chen Z.-G. *Adv. Funct. Mater.* **2017**, *27*, 1703278.
- (7) Francioso L.; De Pascali C.; Farella I.; Martucci C.; Cretì P.; Siciliano P.; Perrone A. *J. Power Sources* **2011**, *196*, 3239-3243.
- (8) Vladimir L. *IEEE Sens. J.* **2013**, *13*, 2284-2291.
- (9) Wang Y.; Liu W.D.; Gao H.; Wang L.J.; Li M.; Shi X.L.; Hong M.; Wang H.; Zou J.; Chen Z.G. *ACS Appl Mater Interfaces* **2019**, *11*, 31237-31244.
- (10) Wang Y.; Liu W.-D.; Shi X.-L.; Hong M.; Wang L.-J.; Li M.; Wang H.; Zou J.; Chen Z.-G. *Chemical Engineering Journal* **2019**,
- (11) Poudel B.; Hao Q.; Ma Y.; Lan Y.; Minnich A.; Yu B.; Yan X.; Wang D.; Muto A.; Vashaee D.; Chen X.; Liu J.; Dresselhaus M.S.; Chen G.; Ren Z. *Science* **2008**, *320*, 634-638.
- (12) Zhu T.; Liu Y.; Fu C.; Heremans J.P.; Snyder J.G.; Zhao X. *Advanced Materials* **2017**, *29*, 1605884.
- (13) Zhang X.; Zhao L.-D. *Journal of Materiomics* **2015**, *1*, 92-105.
- (14) Shi X.; Zheng K.; Hong M.; Liu W.; Moshwan R.; Wang Y.; Qu X.; Chen Z.-G.; Zou J. *Chem. Sci.* **2018**, *9*, 7376-7389.

- (15) Shi X.-L.; Zheng K.; Liu W.-D.; Wang Y.; Yang Y.-Z.; Chen Z.-G.; Zou J. *Adv. Energy Mater.* **2018**, *8*, 1800775.
- (16) Yang T.; Liu J.; Zhou R.; Chen Z.; Xu H.; Qiao S.Z.; Monteiro M.J. *Journal of Materials Chemistry A* **2014**, *2*, 18139-18146.
- (17) She X.; Su X.; Du H.; Liang T.; Zheng G.; Yan Y.; Akram R.; Uher C.; Tang X. *Journal of Materials Chemistry C* **2015**, *3*, 12116-12122.
- (18) Liu W.-D.; Chen Z.-G.; Zou J. *Advanced Energy Materials* **2018**, *8*, 1800056.
- (19) Snyder G.J.; Toberer E.S. *Nat. Mater.* **2008**, *7*, 105-114.
- (20) Zhu T.; Liu Y.; Fu C.; Heremans J.P.; Snyder J.G.; Zhao X. *Adv. Mater.* **2017**, 1605884.
- (21) He R.; Schierning G.; Nielsch K. *Advanced Materials Technologies* **2018**, *3*, 1700256.
- (22) Kim H.S.; Liu W.; Ren Z. *Energy Environ. Sci.* **2017**, *10*, 69-85.
- (23) Li J.F.; Liu W.S.; Zhao L.D.; Zhou M. *NPG Asia Mater.* **2010**, *2*, 152-158.
- (24) Yang L.; Chen Z.-G.; Dargusch M.S.; Zou J. *Advanced Energy Materials* **2018**, *8*, 1701797.
- (25) Zhang L.; Lin S.; Hua T.; Huang B.; Liu S.; Tao X. *Adv. Energy Mater.* **2018**, *8*, 1700524.
- (26) Delkumburewatte G.B.; Dias T. *J. Text. I.* **2012**, *103*, 483-489.
- (27) He W.; Zhang G.; Zhang X.; Ji J.; Li G.; Zhao X. *Appl. Energ.* **2015**, *143*, 1-25.
- (28) Goncalves L.M.; Rocha J.G.; Couto C.; Alpuim P.; Min G.; Rowe D.M.; Correia J.H. *J. Micromech. Microeng* **2007**, *17*, S168-S173.
- (29) Yang J.; Caillat T. *Mrs. Bull.* **2011**, *31*, 224-229.
- (30) Kim H.S.; Liu W.; Chen G.; Chu C.W.; Ren Z. *Proc. Natl. Acad. Sci. U.S.A.* **2015**, *112*, 8205-8210.

- (31) Poudel B.; Hao Q.; Ma Y.; Lan Y.; Minnich A.; Yu B.; Yan X.; Wang D.; Muto A.; Vashaee D.; Chen X.; Liu J.; Dresselhaus M.S.; Chen G.; Ren Z. *Science* **2008**, *320*, 634-638.
- (32) Bharti M.; Singh A.; Samanta S.; Aswal D.K. *Prog. Mater. Sci.* **2017**, *93*, 270-310.
- (33) Ou C.; Sangle A.L.; Datta A.; Jing Q.; Busolo T.; Chalklen T.; Narayan V.; Kar-Narayan S. *ACS Appl. Mater. Interf.* **2018**, *10*, 19580-19587.
- (34) Kim J.-Y.; Lee W.; Kang Y.H.; Cho S.Y.; Jang K.-S. *Carbon* **2018**, *133*, 293-299.
- (35) Chen A.; Madan D.; Wright P.K.; Evans J.W. *J. Micromech. Microeng* **2011**, *21*, 104006.
- (36) J W.; K P.-K.; F H.; P D.; F V.; T D. *Sensors and Actuators A: Physical* **2006**, *132*, 325-330.
- (37) Yang L.; Chen Z.G.; Hong M.; Han G.; Zou J. *ACS Appl Mater Interfaces* **2015**, *7*, 23694-23699.
- (38) Wang Y.; Liu W.-D.; Gao H.; Wang L.-J.; Li M.; Shi X.-L.; Hong M.; Wang H.; Zou J.; Chen Z.-G. *ACS Applied Materials & Interfaces* **2019**, *11*, 31237-31244.
- (39) Son J.S.; Choi M.K.; Han M.K.; Park K.; Kim J.Y.; Lim S.J.; Oh M.; Kuk Y.; Park C.; Kim S.J.; Hyeon T. *Nano Lett* **2012**, *12*, 640-647.
- (40) Zhao X.B.; Ji X.H.; Zhang Y.H.; Zhu T.J.; Tu J.P.; Zhang X.B. *APPLIED PHYSICS LETTERS* **2005**, *86*, 062111
- (41) Hong M.; Chen Z.G.; Yang L.; Zou J. *Nanoscale* **2016**, *8*, 8681-6.
- (42) Hosokawa Y.; Tomita K.; Takashiri M. *Sci Rep* **2019**, *9*, 10790.
- (43) Shi H.; Parker D.; Du M.-H.; Singh D.J. *Physical Review Applied* **2015**, *3*,
- (44) Mishra S.K.; Satpathy S.; Jepsen O. *Journal of Physics: Condensed Matter* **1997**, *9*, 461-470.
- (45) Hong M.; Chen Z.-G.; Zou J. *Chinese Physics B* **2018**, *27*, 048403.

- (46) Wang Y.; Liu W.-D.; Shi X.-L.; Hong M.; Wang L.-J.; Li M.; Wang H.; Zou J.; Chen Z.-G. *Chemical Engineering Journal* **2019**, 123513.
- (47) Shen J.J.; Hu L.P.; Zhu T.J.; Zhao X.B. *Applied Physics Letters* **2011**, 99, 124102.
- (48) Liu Y.; Zhou M.; He J. *Scripta Materialia* **2016**, 111, 39-43.
- (49) Xu Z.; Wu H.; Zhu T.; Fu C.; Liu X.; Hu L.; He J.; He J.; Zhao X. *NPG Asia Materials* **2016**, 8, e302-e302.
- (50) Zhang Q.; Gu B.; Wu Y.; Zhu T.; Fang T.; Yang Y.; Liu J.; Ye B.; Zhao X. *ACS Applied Materials & Interfaces* **2019**, 11, 41424-41431.
- (51) Hwang C.-W.; Hyun D.-B.; Ha H.-P.; Oh T.S. *Journal of Materials Science* **2001**, 36, 3291-3297.
- (52) Hyun D.-B.; Oh T.S.; Hwang J.-S.; Shim J.-D. *Scripta Materialia* **2001**, 44, 455-460.
- (53) Yan B.; Zhang S.C. *Rep Prog Phys* **2012**, 75, 096501.
- (54) Hu L.P.; Liu X.H.; Xie H.H.; Shen J.J.; Zhu T.J.; Zhao X.B. *Acta Materialia* **2012**, 60, 4431-4437.
- (55) Miller G.R.; Li C.-Y. *Journal of Physics and Chemistry of Solids* **1965**, 26, 173-177.
- (56) Horák J.; Čermák K.; Koudelka L. *Journal of Physics and Chemistry of Solids* **1986**, 47, 805-809.
- (57) Hong M.; Chasapis T.C.; Chen Z.-G.; Yang L.; Kanatzidis M.G.; Snyder G.J.; Zou J. *ACS Nano* **2016**, 10, 4719-4727.
- (58) Hong M.; Chen Z.G.; Yang L.; Zou J. *Nano Energy* **2016**, 20, 144-155.
- (59) Gong J.J.; Hong A.J.; Shuai J.; Li L.; Yan Z.B.; Ren Z.F.; Liu J.M. *Phys Chem Chem Phys* **2016**, 18, 16566-74.
- (60) Bahk J.-H.; Shakouri A. *Applied Physics Letters* **2014**, 105, 052106.

- (61) Liu Z.; Mao J.; Peng S.; Zhou B.; Gao W.; Sui J.; Pei Y.; Ren Z. *Materials Today Physics* **2017**, *2*, 54-61.
- (62) Teramoto I.; Takayanagi S. *Journal of Physics and Chemistry of Solids* **1961**, *19*, 124-129.
- (63) Lošťák P.; Drašar Č.; Bachan D.; Beneš L.; Krejčová A. *Radiation Effects and Defects in Solids* **2010**, *165*, 211-215.
- (64) Starý Z.; Horák J.; Stordeur M.; Stölzer M. *Journal of Physics and Chemistry of Solids* **1988**, *49*, 29-34.
- (65) Hu L.; Zhu T.; Liu X.; Zhao X. *Advanced Functional Materials* **2014**, *24*, 5211-5218.
- (66) IVANOVA L.; GRANATKINA Y. *INORGANIC MATERIALS* **1995**, *31*, 678-681.
- (67) BIRKHOLZ U. *Z. Naturforsch. A* **1958**, *13*, 780-792.
- (68) Horák J.; Lošťák P.; Koudelka L.; Novotný R. *Solid State Communications* **1985**, *55*, 1031-1034.
- (69) Lostak P.; Drasar C.; Bachan D.; Benes L.; Krejcova A. *Radiat. Eff. Defect S.* **2010**, *165*, 211-215.
- (70) Wu H.-J.; Yen W.-T. *Acta Materialia* **2018**, *157*, 33-41.
- (71) Lošťák P.; Drašar Č.; Horák J.; Zhou Z.; Dyck J.S.; Uher C. *Journal of Physics and Chemistry of Solids* **2006**, *67*, 1457-1463.
- (72) Plecháček T.; Navrátil J.; Horák J.; Bachan D.; Krejčová A.; Lošťák P. *Solid State Ionics* **2007**, *177*, 3513-3519.
- (73) Guo X.; Qin J.; Lv X.; Deng L.; Jia X.; Ma H.; Jia H. *RSC Advances* **2016**, *6*, 60736-60740.
- (74) Horák J.; Lošťák P.; Drašar Č.; Dyck J.S.; Zhou Z.; Uher C. *Journal of Solid State Chemistry* **2005**, *178*, 2907-2912.

- (75) Liu W.-S.; Zhang Q.; Lan Y.; Chen S.; Yan X.; Zhang Q.; Wang H.; Wang D.; Chen G.; Ren Z. *Advanced Energy Materials* **2011**, *1*, 577-587.
- (76) Horák J.; Navrátil J.; Starý Z. *Journal of Physics and Chemistry of Solids* **1992**, *53*, 1067-1072.
- (77) Lin S.-S.; Liao C.-N. *Journal of Applied Physics* **2011**, *110*, 093707.
- (78) Kuo C.-H.; Hwang C.-S.; Jeng M.-S.; Su W.-S.; Chou Y.-W.; Ku J.-R. *Journal of Alloys and Compounds* **2010**, *496*, 687-690.
- (79) Zhu T.; Hu L.; Zhao X.; He J. *Advanced Science* **2016**, *3*, 1600004.
- (80) Hu L.; Wu H.; Zhu T.; Fu C.; He J.; Ying P.; Zhao X. *Advanced Energy Materials* **2015**, *5*, 1500411.
- (81) Schultz J.M.; McHugh J.P.; Tiller W.A. *Journal of Applied Physics* **1962**, *33*, 2443-2450.
- (82) George W.R.; Sharples R.; Thompson J.E. *Proceedings of the Physical Society* **1959**, *74*, 768-770.
- (83) Zhao L.D.; Zhang B.P.; Li J.F.; Zhou M.; Liu W.S. *Physica B: Condensed Matter* **2007**, *400*, 11-15.
- (84) Shen J.-J.; Zhu T.-J.; Zhao X.-B.; Zhang S.-N.; Yang S.-H.; Yin Z.-Z. *Energy & Environmental Science* **2010**, *3*, 1519-1523.
- (85) Zhao L.D.; Zhang B.P.; Li J.F.; Zhang H.L.; Liu W.S. *Solid State Sciences* **2008**, *10*, 651-658.
- (86) Yan X.; Poudel B.; Ma Y.; Liu W.S.; Joshi G.; Wang H.; Lan Y.; Wang D.; Chen G.; Ren Z.F. *Nano Lett* **2010**, *10*, 3373-3378.
- (87) Xiu F.; He L.; Wang Y.; Cheng L.; Chang L.-T.; Lang M.; Huang G.; Kou X.; Zhou Y.; Jiang X.; Chen Z.; Zou J.; Shailos A.; Wang K.L. *Nature Nanotechnology* **2011**, *6*, 216-221.

- (88) Zhang G.; Kirk B.; Jauregui L.A.; Yang H.; Xu X.; Chen Y.P.; Wu Y. *Nano Letters* **2012**, *12*, 56-60.
- (89) Min Y.; Moon G.D.; Kim B.S.; Lim B.; Kim J.-S.; Kang C.Y.; Jeong U. *Journal of the American Chemical Society* **2012**, *134*, 2872-2875.
- (90) Min Y.; Roh J.W.; Yang H.; Park M.; Kim S.I.; Hwang S.; Lee S.M.; Lee K.H.; Jeong U. *Advanced Materials* **2013**, *25*, 1425-1429.
- (91) Lu W.; Ding Y.; Chen Y.; Wang Z.L.; Fang J. *Journal of the American Chemical Society* **2005**, *127*, 10112-10116.
- (92) Mi J.-L.; Lock N.; Sun T.; Christensen M.; Søndergaard M.; Hald P.; Hng H.H.; Ma J.; Iversen B.B. *ACS Nano* **2010**, *4*, 2523-2530.
- (93) Wang S.; Tan G.; Xie W.; Zheng G.; Li H.; Yang J.; Tang X. *Journal of Materials Chemistry* **2012**, *22*, 20943-20951.
- (94) Wang S.; Tan G.; Xie W.; Zheng G.; Li H.; Yang J.; Tang X. *Journal of Materials Chemistry* **2012**, *22*, 20943.
- (95) Hong M.; Chen Z.-G.; Yang L.; Han G.; Zou J. *Advanced Electronic Materials* **2015**, *1*, 1500025.
- (96) Xie W.; Tang X.; Yan Y.; Zhang Q.; Tritt T.M. *APPLIED PHYSICS LETTERS* **2009**, *94*, 102111.
- (97) Ivanova L.D.; Petrova L.I.; Granatkina Y.V.; Kichik S.A.; Marakushev I.S.; Mel'nikov A.A. *Inorganic Materials* **2015**, *51*, 741-745.
- (98) Son J.H.; Oh M.W.; Kim B.S.; Park S.D.; Min B.K.; Kim M.H.; Lee H.W. *Journal of Alloys and Compounds* **2013**, *566*, 168-174.

- (99) Wang Y.; Yang L.; Shi X.L.; Shi X.; Chen L.; Dargusch M.S.; Zou J.; Chen Z.G. *Adv Mater* **2019**, *31*, e1807916.
- (100) Blackburn J.L.; Ferguson A.J.; Cho C.; Grunlan J.C. *Adv. Mater.* **2018**, *30*, 1704386.
- (101) Zhao W.; Fan S.; Xiao N.; Liu D.; Tay Y.Y.; Yu C.; Sim D.; Hng H.H.; Zhang Q.; Boey F.; Ma J.; Zhao X.; Zhang H.; Yan Q. *Energy Environ. Sci.* **2012**, *5*, 5364-5369.
- (102) Yang L.; Chen Z.G.; Hong M.; Han G.; Zou J. *ACS Appl. Mater. Interfaces* **2015**, *7*, 23694-23699.
- (103) Yang L.; Chen Z.-G.; Nie T.; Han G.; Zhang Z.; Hong M.; Wang K.L.; Zou J. *J. Mater. Chem. C* **2016**, *4*, 521-525.
- (104) Shi X.; Wu A.; Liu W.; Moshwan R.; Wang Y.; Chen Z.G.; Zou J. *ACS Nano* **2018**,
- (105) Moshwan R.; Shi X.L.; Liu W.D.; Yang L.; Wang Y.; Hong M.; Auchterlonie G.; Zou J.; Chen Z.G. *ACS Appl. Mater. Interfaces* **2018**, *10*, 38944–38952.
- (106) Huang Z.-Y.; Zhang H.; Yang L.; Zhu B.; Zheng K.; Hong M.; Yu Y.; Zu F.-Q.; Zou J.; Chen Z.-G. *Mater.Today Energy* **2018**, *9*, 383-390.
- (107) Hong M.; Wang Y.; Liu W.; Matsumura S.; Wang H.; Zou J.; Chen Z.-G. *Adv. Energy Mater.* **2018**, *8*, 1801837.
- (108) Hong M.; Chen Z.-G.; Yang L.; Liao Z.-M.; Zou Y.-C.; Chen Y.-H.; Matsumura S.; Zou J. *Adv. Energy Mater.* **2018**, *8*, 1702333.
- (109) Kim G.H.; Shao L.; Zhang K.; Pipe K.P. *Nature Materials* **2013**, *12*, 719-723.
- (110) See K.C.; Feser J.P.; Chen C.E.; Majumdar A.; Urban J.J.; Segalman R.A. *Nano Lett.* **2010**, *10*, 4664-4667.
- (111) Nath C.; Kumar A.; Kuo Y.-K.; Okram G.S. *Appl. Phys. Lett.* **2014**, *105*, 133108.
- (112) Huang C.; Qian X.; Yang R. *Mater. Sci. Eng. R Rep.* **2018**, *132*, 1-22.

- (113) He M.; Ge J.; Lin Z.; Feng X.; Wang X.; Lu H.; Yang Y.; Qiu F. *Energy & Environmental Science* **2012**, *5*, 8351.
- (114) Zhang B.; Sun J.; Katz H.E.; Fang F.; Opila R.L. *ACS Appl. Mater. Interfaces* **2010**, *2*, 3170-3178.
- (115) Jin Q.; Jiang S.; Zhao Y.; Wang D.; Qiu J.; Tang D.-M.; Tan J.; Sun D.-M.; Hou P.-X.; Chen X.-Q.; Tai K.; Gao N.; Liu C.; Cheng H.-M.; Jiang X. *Nat. Mater.* **2018**,
- (116) Minnich A.J.; Dresselhaus M.S.; Ren Z.F.; Chen G. *Energy Environ. Sci.* **2009**, *2*, 466-479.
- (117) Ko D.K.; Kang Y.; Murray C.B. *Nano Lett.* **2011**, *11*, 2841-2844.
- (118) Zhou C.; Dun C.; Wang Q.; Wang K.; Shi Z.; Carroll D.L.; Liu G.; Qiao G. *ACS Appl. Mater. Interfaces* **2015**, *7*, 21015-21020.
- (119) Russ B.; Glaudell A.; Urban J.J.; Chabinyk M.L.; Segalman R.A. *Nat. Rev. Mater.* **2016**, *1*, 16050.
- (120) Scheele M.; Oeschler N.; Veremchuk I.; Peters S.-O.; Littig A.; Kornowski A.; Klinke C.; Weller H. *ACS Nano* **2011**, *5*, 8541-8551.
- (121) Nuthongkum P.; Sakulkalavek A.; Sakdanuphab R. *J. Electron. Mater.* **2016**, *46*, 2900-2907.
- (122) Fan P.; Fan W.-f.; Zheng Z.-h.; Zhang Y.; Luo J.-t.; Liang G.-x.; Zhang D.-p. *J. Mater. Sci.* **2014**, *25*, 5060-5065.
- (123) Nuthongkum P.; Sakdanuphab R.; Horprathum; Mati; Sakulkalavek A. *J. Electron. Mater.* **2017**, *46*, 6444-6450.
- (124) Pargellis A.N. *J. Vac. Sci. Technol. A* **1989**, *7*, 27-30.
- (125) Goncalves L.M.; Alpuim P.; Rolo A.G.; Correia J.H. *Thin Solid Films* **2011**, *519*, 4152-4157.

- (126) Goncalves L.M.; Couto C.; Alpuim P.; Rolo A.G.; Völklein F.; Correia J.H. *Thin Solid Films* **2010**, *518*, 2816-2821.
- (127) Goncalves L.M.; Alpuim P.; Min G.; Rowe D.M.; Couto C.; Correia J.H. *Vacuum* **2008**, *82*, 1499-1502.
- (128) Yang C.; Kneibeta M.; Lorenz M.; Grundmann M. *Proc. Natl. Acad. Sci. U.S.A.* **2016**, *113*, 12929-12933.
- (129) Yang C.; Kneiss M.; Schein F.L.; Lorenz M.; Grundmann M. *Sci. Rep.* **2016**, *6*, 21937.
- (130) Yang C.; Souchay D.; Kneiss M.; Bogner M.; Wei H.M.; Lorenz M.; Oeckler O.; Benstetter G.; Fu Y.Q.; Grundmann M. *Nat. Commun.* **2017**, *8*, 16076.
- (131) Patil N.S.; Sargar A.M.; Mane S.R.; Bhosale P.N. *Mater. Chem. Phys.* **2009**, *115*, 47-51.
- (132) Zhao Y.; Dyck J.S.; Burda C. *J. Mater. Chem.* **2011**, *21*, 17049.
- (133) Ortega-Borges R.; Linco D. *J. Electrochem. Soc* **1993**, *140*, 3464-3473.
- (134) Shi X.; Chen H.; Hao F.; Liu R.; Wang T.; Qiu P.; Burkhardt U.; Grin Y.; Chen L. *Nat. Mater.* **2018**, *17*, 421-426.
- (135) Zhang C.; Zhang E.; Wang W.; Liu Y.; Chen Z.-G.; Lu S.; Liang S.; Cao J.; Yuan X.; Tang L.; Li Q.; Zhou C.; Gu T.; Wu Y.; Zou J.; Xiu F. *Nature Communications* **2017**, *8*, 13741.
- (136) Wan C.; Gu X.; Dang F.; Itoh T.; Wang Y.; Sasaki H.; Kondo M.; Koga K.; Yabuki K.; Snyder G.J.; Yang R.; Koumoto K. *Nat. Mater.* **2015**, *14*, 622-627.
- (137) Wan C.; Tian R.; Azizi A.B.; Huang Y.; Wei Q.; Sasai R.; Wasusate S.; Ishida T.; Koumoto K. *Nano Energy* **2016**, *30*, 840-845.
- (138) Costescu R.M.; Cahill D.G.; Fabreguette F.H.; Sechrist Z.A.; George M. *Science* **2004**, *303*, 989-990.

- (139) Tynell T.; Giri A.; Gaskins J.; Hopkins P.E.; Mele P.; Miyazaki K.; Karppinen M. *J. Mater. Chem. A* **2014**, *2*, 12150-12152.
- (140) Niemelä J.-P.; Giri A.; Hopkins P.E.; Karppinen M. *J. Mater. Chem. A* **2015**, *3*, 11527-11532.
- (141) Liu J.; Yoon B.; Kuhlmann E.; Tian M.; Zhu J.; George S.M.; Lee Y.C.; Yang R. *Nano Lett.* **2013**, *13*, 5594-5599.
- (142) Tian R.; Wan C.; Wang Y.; Wei Q.; Ishida T.; Yamamoto A.; Tsuruta A.; Shin W.; Li S.; Koumoto K. *J. Mater. Chem. A* **2017**, *5*, 564-570.
- (143) Tanskanen A.; Karppinen M. *Dalton Transact.* **2015**, *44*, 19194-19199.
- (144) Tian R.; Wan C.; Hayashi N.; Aoai T.; Koumoto K. *Mrs. Bull.* **2018**, *43*, 193-198.
- (145) Moshwan R.; Shi X.-L.; Liu W.-D.; Wang Y.; Xu S.; Zou J.; Chen Z.-G. *ACS Applied Energy Materials* **2019**, *2*, 2965-2971.
- (146) Ji X.H.; Zhao X.B.; Zhang Y.H.; Lu B.H.; Ni H.L. *Materials Letters* **2005**, *59*, 682-685.
- (147) Moshwan R.; Liu W.-D.; Shi X.-L.; Sun Q.; Gao H.; Wang Y.-P.; Zou J.; Chen Z.-G. *Journal of Materials Chemistry A* **2020**, *8*, 3978-3987.
- (148) Hong M.; Wang Y.; Liu W.; Matsumura S.; Wang H.; Zou J.; Chen Z.-G. *Advanced Energy Materials* **2018**, *8*, 1801837.
- (149) Hong M.; Chen Z.G.; Yang L.; Zou Y.C.; Dargusch M.S.; Wang H.; Zou J. *Advanced Materials* **2018**, *30*, 1705942.
- (150) Hong M.; Wang Y.; Feng T.; Sun Q.; Xu S.; Matsumura S.; Pantelides S.T.; Zou J.; Chen Z.G. *J Am Chem Soc* **2019**, *141*, 1742-1748.
- (151) Liu W.; Tang X.; Sharp J. *Journal of Physics D: Applied Physics* **2010**, *43*, 085406.

- (152) Li M.; Cortie D.L.; Liu J.; Yu D.; Islam S.M.K.N.; Zhao L.; Mitchell D.R.G.; Mole R.A.; Cortie M.B.; Dou S.; Wang X. *Nano Energy* **2018**, *53*, 993-1002.
- (153) Hu L.-P.; Zhu T.-J.; Wang Y.-G.; Xie H.-H.; Xu Z.-J.; Zhao X.-B. *NPG Asia Materials* **2014**, *6*, e88-e88.
- (154) Cao S.; Huang Z.Y.; Zu F.Q.; Xu J.; Yang L.; Chen Z.G. *ACS Appl Mater Interfaces* **2017**, *9*, 36478-36482.
- (155) Huang Z.-Y.; Zhang H.; Yang L.; Zhu B.; Zheng K.; Hong M.; Yu Y.; Zu F.-Q.; Zou J.; Chen Z.-G. *Materials Today Energy* **2018**, *9*, 383-390.
- (156) Huang Z.; Zhang H.; Zheng K.; Dai X.; Yu Y.; Cheng H.; Zu F.; Chen Z.-G. *Progress in Natural Science: Materials International* **2018**, *28*, 218-224.
- (157) Huang Z.; Dai X.; Yu Y.; Zhou C.; Zu F. *Scripta Materialia* **2016**, *118*, 19-23.
- (158) Wei Q.F.; Gao W.D.; Hou D.Y.; Wang X.Q. *Applied Surface Science* **2005**, *245*, 16-20.
- (159) Snyder G.J.; Toberer E.S. *Nat Mater* **2008**, *7*, 105-114.
- (160) Moshwan R.; Yang L.; Zou J.; Chen Z.-G. *Advanced Functional Materials* **2017**, *1703278*.
- (161) Chen Z.-G.; Shi X.; Zhao L.-D.; Zou J. *Progress in Materials Science* **2018**, *97*, 283-346.
- (162) Dong J.; Sun F.-H.; Tang H.; Pei J.; Zhuang H.-L.; Hu H.-H.; Zhang B.-P.; Pan Y.; Li J.-F. *Energy & Environmental Science* **2019**, *12*, 1396-1403.
- (163) Xia K.; Liu Y.; Anand S.; Snyder G.J.; Xin J.; Yu J.; Zhao X.; Zhu T. *Advanced Functional Materials* **2018**, *28*, 1705845.
- (164) Chen C.-L.; Wang H.; Chen Y.-Y.; Day T.; Snyder G.J. *J. Mater. Chem. A* **2014**, *2*, 11171-11176.

- (165) Jiang G.; He J.; Zhu T.; Fu C.; Liu X.; Hu L.; Zhao X. *Advanced Functional Materials* **2014**, *24*, 3776-3781.
- (166) Toberer E.S.; May A.F.; Snyder G.J. *Chemistry of Materials* **2010**, *22*, 624-634.
- (167) Wang S.; Xie W.; Li H.; Tang X. *Intermetallics* **2011**, *19*, 1024-1031.
- (168) Xu Z.J.; Hu L.P.; Ying P.J.; Zhao X.B.; Zhu T.J. *Acta Materialia* **2015**, *84*, 385-392.
- (169) West D.; Sun Y.Y.; Wang H.; Bang J.; Zhang S.B. *Physical Review B* **2012**, *86*, 121201.
- (170) Urazhdin S.; Bilc D.; Mahanti S.D.; Tessmer S.H.; Kyratsi T.; Kanatzidis M.G. *Physical Review B* **2004**, *69*, 085313.
- (171) Hu L.; Gao H.; Liu X.; Xie H.; Shen J.; Zhu T.; Zhao X. *Journal of Materials Chemistry* **2012**, *22*, 16484.
- (172) Hong M.; Chasapis T.C.; Chen Z.G.; Yang L.; Kanatzidis M.G.; Snyder G.J.; Zou J. *ACS Nano* **2016**, *10*, 4719-4727.
- (173) Tan G.; Shi F.; Hao S.; Zhao L.-D.; Chi H.; Zhang X.; Uher C.; Wolverton C.; Dravid V.P.; Kanatzidis M.G. *Nature Communications* **2016**, *7*, 12167.
- (174) Zhang Y.; Day T.; Snedaker M.L.; Wang H.; Kramer S.; Birkel C.S.; Ji X.; Liu D.; Snyder G.J.; Stucky G.D. *Advanced Materials* **2012**, *24*, 5065-70.
- (175) Fu J.; Song S.; Zhang X.; Cao F.; Zhou L.; Li X.; Zhang H. *CrystEngComm* **2012**, *14*, 2159-2165.
- (176) Yu F.; Xu B.; Zhang J.; Yu D.; He J.; Liu Z.; Tian Y. *Materials Research Bulletin* **2012**, *47*, 1432-1437.
- (177) Song E.; Baranovskiy A.; Xu E.; Busani T.; Swartzentruber B.; Zhang S.; Amouyal Y.; Martinez J.A. *AIP ADVANCES* **2018**, *8*, 105010.

- (178) Hong M.; Wang Y.; Xu S.; Shi X.; Chen L.; Zou J.; Chen Z.-G. *Nano Energy* **2019**, *60*, 1-7.
- (179) Liu W.; Shi X.; Hong M.; Yang L.; Moshwan R.; Chen Z.-G.; Zou J. *Journal of Materials Chemistry C* **2018**, *6*, 13225-13231.
- (180) Ma Y.; Hao Q.; Poudel B.; Lan Y.; Yu B.; Wang D.; Chen G.; Ren Z. *Nano Letters* **2008**, *8*, 2580-2584.
- (181) Kim H.-S.; Gibbs Z.M.; Tang Y.; Wang H.; Snyder G.J. *APL Materials* **2015**, *3*, 041506.
- (182) Mehta R.J.; Zhang Y.; Karthik C.; Singh B.; Siegel R.W.; Borca-Tasciuc T.; Ramanath G. *Nature Materials* **2012**, *11*, 233-240.
- (183) Snyder G.J.; Toberer E.S. *Nature Materials* **2008**, 105-114.
- (184) Wang Y.; Yang L.; Shi X.-L.; Shi X.; Chen L.; S. Dargusch M.; Zou J.; Chen Z.-G. *Advanced Materials* **2019**,
- (185) Shi X.; Zheng K.; Hong M.; Liu W.; Moshwan R.; Wang Y.; Qu X.; Chen Z.G.; Zou J. *Chem Sci* **2018**, *9*, 7376-7389.
- (186) Moshwan R.; Shi X.L.; Liu W.D.; Yang L.; Wang Y.; Hong M.; Auchterlonie G.; Zou J.; Chen Z.G. *ACS Appl Mater Interfaces* **2018**, *10*, 38944-38952.
- (187) Hong M.; Chen Z.G.; Yang L.; Zou Y.C.; Dargusch M.S.; Wang H.; Zou J. *Advanced Materials* **2018**, *30*,
- (188) Pei Y.; Shi X.; LaLonde A.; Wang H.; Chen L.; Snyder G.J. *Nature* **2011**, *473*, 66-69.
- (189) Fu C.; Bai S.; Liu Y.; Tang Y.; Chen L.; Zhao X.; Zhu T. *Nat Commun* **2015**, *6*, 8144.
- (190) Hong M.; Wang Y.; Liu W.; Matsumura S.; Wang H.; Zou J.; Chen Z.-G. *Advanced Energy Materials* **2018**, *8*, 1801837.

- (191) Kim S.I.; Lee K.H.; Mun H.A.; Kim H.S.; Hwang S.W.; Roh J.W.; Yang D.J.; Shin W.H.; Li X.S.; Lee Y.H.; Snyder G.J.; Kim S.W. *Science* **2015**, *348*, 109-114.
- (192) Mehta R.J.; Zhang Y.; Karthik C.; Singh B.; Siegel R.W.; Borca-Tasciuc T.; Ramanath G. *Nat Mater* **2012**, *11*, 233-40.
- (193) Zhang Y.; Mehta R.J.; Belley M.; Han L.; Ramanath G.; Borca-Tasciuc T. *Applied Physics Letters* **2012**, *100*, 193113.
- (194) Xu B.; Feng T.; Agne M.T.; Zhou L.; Ruan X.; Snyder G.J.; Wu Y. *Angew Chem Int Ed Engl* **2017**, *56*, 3546-3551.
- (195) Toberer E.S.; Zevalkink A.; Snyder G.J. *Journal of Materials Chemistry* **2011**, *21*, 15843.
- (196) Hong M.; Chen Z.G.; Yang L.; Zou J. *Nano Energy* **2016**, *20*, 144-155.
- (197) K.V.Domoratsky; E.F.Dudnik; V.F.Katkov; L.Ya.Sadovskaya *Condensed Matter Physics* **1999**, *2*, 591-594.
- (198) Scheele M.; Oeschler N.; Meier K.; Kornowski A.; Klinke C.; Weller H. *Advanced Functional Materials* **2009**, *19*, 3476-3483.
- (199) Xu Y.; Li W.; Wang C.; Li J.; Chen Z.; Lin S.; Chen Y.; Pei Y. *J. Mater. Chem. A* **2017**, *5*, 19143-19150.
- (200) Hoefler K.; Becker C.; Rata D.; Swanson J.; Thalmeier P.; Tjeng L.H. *Proc Natl Acad Sci U S A* **2014**, *111*, 14979-14984.
- (201) Tang X.; Xie W.; Li H.; Zhao W.; Zhang Q. *Applied Physics Letters* **2007**, *90*, 012102.
- (202) Mei D.; Wang H.; Li Y.; Yao Z.; Zhu T. *Journal of Materials Research* **2015**, *30*, 2585-2592.
- (203) Fang H.; Bahk J.-H.; Feng T.; Cheng Z.; Mohammed A.M.S.; Wang X.; Ruan X.; Shakouri A.; Wu Y. *Nano Research* **2015**, *9*, 117-127.

- (204) Qu S.; Yao Q.; Wang L.; Chen Z.; Xu K.; Zeng H.; Shi W.; Zhang T.; Uher C.; Chen L. *NPG Asia Materials* **2016**, *8*, e292-e292.
- (205) Slack G.A.; Ross R.G. *Journal of Physics C: Solid State Physics* **1985**, *18*, 3957-3980.
- (206) Zhao K.; Duan H.; Raghavendra N.; Qiu P.; Zeng Y.; Zhang W.; Yang J.; Shi X.; Chen L. *Adv. Mater.* **2017**, *29*, 1701148.
- (207) Liu W.-D.; Shi X.-L.; Gao H.; Moshwan R.; Xu S.-D.; Wang Y.; Yang L.; Chen Z.-G.; Zou J. *Journal of Materials Chemistry C* **2019**, *7*, 5366-5373.
- (208) Russ B.; Glauddell A.; Urban J.J.; Chabinye M.L.; Segalman R.A. *Nature Reviews Materials* **2016**, *1*, 16050.
- (209) Ding Y.; Qiu Y.; Cai K.; Yao Q.; Chen S.; Chen L.; He J. *Nat Commun* **2019**, *10*, 841.
- (210) Fan Z.; Li P.; Du D.; Ouyang J. *Advanced Energy Materials* **2017**, *7*, 1602116.
- (211) Kim N.; Kee S.; Lee S.H.; Lee B.H.; Kahng Y.H.; Jo Y.-R.; Kim B.-J.; Lee K. *Advanced Materials* **2014**, *26*, 2268-2272.
- (212) Wei Q.; Mukaida M.; Naitoh Y.; Ishida T. *Advanced Materials* **2013**, *25*, 2831-2836.
- (213) Xu S.; Hong M.; Shi X.-L.; Wang Y.; Ge L.; Bai Y.; Wang L.; Dargusch M.; Zou J.; Chen Z.-G. *Chemistry of Materials* **2019**, *31*, 5238-5244.
- (214) Zhang Q.; Sun Y.; Xu W.; Zhu D. *Energy & Environmental Science* **2012**, *5*, 9639-9644.
- (215) Chen L.; Liu W.; Yan Y.; Su X.; Xiao S.; Lu X.; Uher C.; Tang X. *Journal of Materials Chemistry C* **2019**, *7*, 2333-2344.
- (216) Yao Q.; Chen L.; Zhang W.; Liufu S.; Chen X. *ACS Nano* **2010**, *4*, 2445-2451.
- (217) Zengin H.; Zhou W.; Jin J.; Czerw R.; Smith Jr. D.W.; Echegoyen L.; Carroll D.L.; Foulger S.H.; Ballato J. *Advanced Materials* **2002**, *14*, 1480-1483.

- (218) Yao Q.; Wang Q.; Wang L.; Chen L. *Energy & Environmental Science* **2014**, *7*, 3801-3807.
- (219) Yao Q.; Wang Q.; Wang L.; Wang Y.; Sun J.; Zeng H.; Jin Z.; Huang X.; Chen L. *Journal of Materials Chemistry A* **2014**, *2*, 2634-2640.
- (220) Lee K.; Cho S.; Heum Park S.; Heeger A.J.; Lee C.-W.; Lee S.-H. *Nature* **2006**, *441*, 65-68.
- (221) Ouyang J.; Chu C.-W.; Chen F.-C.; Xu Q.; Yang Y. *Advanced Functional Materials* **2005**, *15*, 203-208.
- (222) Xia Y.; Ouyang J. *Journal of Materials Chemistry* **2011**, *21*, 4927-4936.
- (223) Ouyang J.; Xu Q.F.; Chu C.W.; Yang Y.; Li G.; Shinar J. *Polymer* **2004**, *45*, 8443-8450.
- (224) Kim J.Y.; Jung J.H.; Lee D.E.; Joo J. *Synthetic Metals* **2002**, *126*, 311-316.
- (225) Kim N.; Kee S.; Lee S.H.; Lee B.H.; Kahng Y.H.; Jo Y.R.; Kim B.J.; Lee K. *Adv Mater* **2014**, *26*, 2268-72, 2109.
- (226) Bubnova O.; Khan Z.U.; Malti A.; Braun S.; Fahlman M.; Berggren M.; Crispin X. *Nature Materials* **2011**, *10*, 429-433.
- (227) Massonnet N.; Carella A.; Jaudouin O.; Rannou P.; Laval G.; Celle C.; Simonato J.-P. *Journal of Materials Chemistry C* **2014**, *2*, 1278-1283.
- (228) Du Y.; Cai K.F.; Chen S.; Cizek P.; Lin T. *ACS Appl Mater Interfaces* **2014**, *6*, 5735-43.
- (229) Zhang B.; Sun J.; Katz H.E.; Fang F.; Opila R.L. *ACS Applied Materials & Interfaces* **2010**, *2*, 3170-3178.
- (230) Ni D.; Song H.; Chen Y.; Cai K. *Journal of Materiomics* **2019**,
- (231) See K.C.; Feser J.P.; Chen C.E.; Majumdar A.; Urban J.J.; Segalman R.A. *Nano Lett* **2010**, *10*, 4664-7.

- (232) Wang L.; Zhang Z.; Liu Y.; Wang B.; Fang L.; Qiu J.; Zhang K.; Wang S. *Nature Communications* **2018**, *9*, 3817.
- (233) Goo G.; Anoop G.; Unithrattil S.; Kim W.S.; Lee H.J.; Kim H.B.; Jung M.H.; Park J.; Ko H.C.; Jo J.Y. *Advanced Electronic Materials* **2019**, *5*, 1800786.
- (234) Lu Y.; Qiu Y.; Jiang Q.; Cai K.; Du Y.; Song H.; Gao M.; Huang C.; He J.; Hu D. *ACS Applied Materials & Interfaces* **2018**, *10*, 42310-42319.
- (235) Meng Q.; Jiang Q.; Cai K.; Chen L. *Organic Electronics* **2019**, *64*, 79-85.
- (236) Ju H.; Kim J. *ACS Nano* **2016**, *10*, 5730-5739.
- (237) Zhu D.; Huang W.; Song M.; Tu M. *Journal of Wuhan University of Technology-Mater. Sci. Ed.* **2007**, *22*, 88-90.
- (238) We J.H.; Kim S.J.; Cho B.J. *Energy* **2014**, *73*, 506-512.
- (239) Bharti M.; Singh A.; Saini G.; Saha S.; Bohra A.; Kaneko Y.; Debnath A.K.; Muthe K.P.; Marumoto K.; Aswal D.K.; Gadkari S.C. *Journal of Power Sources* **2019**, *435*, 226758.
- (240) Zhang Q.; Sun Y.; Xu W.; Zhu D. *Advanced Materials* **2014**, *26*, 6829-6851.
- (241) Aasmundtveit K.E.; Samuelsen E.J.; Pettersson L.A.A.; Inganäs O.; Johansson T.; Feidenhans'l R. *Synthetic Metals* **1999**, *101*, 561-564.
- (242) Kroon R.; Mengistie D.A.; Kiefer D.; Hynynen J.; Ryan J.D.; Yu L.; Müller C. *Chemical Society Reviews* **2016**, *45*, 6147-6164.
- (243) Bubnova O.; Crispin X. *Energy & Environmental Science* **2012**, *5*, 9345-9362.
- (244) Garreau S.; Louarn G.; Buisson J.P.; Froyer G.; Lefrant S. *Macromolecules* **1999**, *32*, 6807-6812.
- (245) Liang Z.; Boland M.J.; Butrouna K.; Strachan D.R.; Graham K.R. *Journal of Materials Chemistry A* **2017**, *5*, 15891-15900.

- (246) Lim J.Y.; Cho S.; Kim H.; Seo Y. *ACS Applied Energy Materials* **2019**, *2*, 8219-8228.
- (247) Bae E.J.; Kang Y.H.; Jang K.S.; Lee C.; Cho S.Y. *Nanoscale* **2016**, *8*, 10885-10890.
- (248) Choi J.; Lee J.Y.; Lee S.-S.; Park C.R.; Kim H. *Advanced Energy Materials* **2016**, *6*, 1502181.
- (249) Gayner C.; Amouyal Y. *Advanced Functional Materials* **2019**, 1901789.
- (250) Chen Y.; He M.; Tang J.; Bazan G.C.; Liang Z. *Adv. Electr. Mater.* **2018**, *4*, 1800200.
- (251) Gong C.; Li L.; Li Z.; Ji H.; Stern A.; Xia Y.; Cao T.; Bao W.; Wang C.; Wang Y.; Qiu Z.Q.; Cava R.J.; Louie S.G.; Xia J.; Zhang X. *Nature* **2017**, *546*, 265-269.
- (252) Huang B.; Clark G.; Navarro-Moratalla E.; Klein D.R.; Cheng R.; Seyler K.L.; Zhong D.; Schmidgall E.; McGuire M.A.; Cobden D.H.; Yao W.; Xiao D.; Jarillo-Herrero P.; Xu X. *Nature* **2017**, *546*, 270-273.
- (253) Lu X.; Zhao D.; Ma T.; Wang Q.; Fan J.; Yang R. *Energy Convers. Manage* **2018**, *169*, 186-193.
- (254) Nan K.; Kang S.D.; Li K.; Yu K.J.; Zhu F.; Wang J.; Dunn A.C.; Zhou C.; Xie Z.; Agne M.T.; Wang H.; Luan H.; Zhang Y.; Huang Y.; Snyder G.J.; Rogers J.A. *Sci. Adv.* **2018**, *4*, eaau5849.
- (255) Mu E.; Yang G.; Fu X.; Wang F.; Hu Z. *J. Power Sources* **2018**, *394*, 17-25.
- (256) Jin W.; Liu L.; Yang T.; Shen H.; Zhu J.; Xu W.; Li S.; Li Q.; Chi L.; Di C.A.; Zhu D. *Nat. Commun.* **2018**, *9*, 3586.
- (257) Li G.; Garcia Fernandez J.; Lara Ramos D.A.; Barati V.; Pérez N.; Soldatov I.; Reith H.; Schierning G.; Nielsch K. *Nat. Electron.* **2018**, *1*, 555-561.

Appendix:

Other publications during candidature

1. Hong, M.; **Wang, Y.**; Liu, W.; Matsumura, S.; Wang, H.; Zou, J.; Chen, Z.-G. Arrays of Planar Vacancies in Superior Thermoelectric $\text{Ge}_{1-x-y}\text{Cd}_x\text{Bi}_y\text{Te}$ with Band Convergence. *Adv. Energy Mater.* **2018**, *8*, 1801837. (2020 IF=25.17)
2. Hong, M.; **Wang, Y.**; Xu, S.; Shi, X.; Chen, L.; Zou, J.; Chen, Z.-G. Nanoscale Pores plus Precipitates Rendering High-Performance Thermoelectric $\text{SnTe}_{1-x}\text{Se}_x$ with Refined Band Structures. *Nano Energy* **2019**, *60*, 1-7. (2020 IF=17.18)
3. Hong, M.; **Wang, Y.**; Feng, T.; Sun, Q.; Xu, S.; Matsumura, S.; Pantelides, S. T.; Zou, J.; Chen, Z. G. Strong Phonon-Phonon Interactions Securing Extraordinary Thermoelectric $\text{Ge}_{1-x}\text{Sb}_x\text{Te}$ with Zn-Alloying-Induced Band Alignment. *J. Am. Chem. Soc.* **2019**, *141*, 1742-1748. (2020 IF=15.04)
4. Hong, M.; Lyu, W.; **Wang, Y.**; Zou, J.; Chen, Z.-G. Establishing the Golden Range of Seebeck Coefficient for Maximizing Thermoelectric Performance. *J. Am. Chem. Soc.* **2020**, *142*, 2672-2681. (2020 IF=15.04)
5. Liu, T.; Bao, D.; **Wang, Y.**; Gao, H.; Zhou, D.; Han, G.; Tang, J.; Huang, Z.-Y.; Yang, L.; Chen, Z.-G. Exploring Thermoelectric Performance of $\text{Ca}_3\text{Co}_4\text{O}_{9+\delta}$ Ceramics *via* Chemical Electroless Plating with Cu. *J. Alloys Compd.* **2020**, *821*, 153522. (2020 IF=4.67)
6. Xu, S.; Hong, M.; Shi, X.-L.; **Wang, Y.**; Ge, L.; Bai, Y.; Wang, L.; Dargusch, M.; Zou, J.; Chen, Z.-G. High-Performance PEDOT:PSS Flexible Thermoelectric Materials and Their Devices by Triple Post-Treatments. *Chem. Mater.* **2019**, *31*, 5238-5244. (2020 IF=9.73)
7. Shi, X.-L.; Zheng, K.; Liu, W.-D.; **Wang, Y.**; Yang, Y.-Z.; Chen, Z.-G.; Zou, J. Realizing High Thermoelectric Performance in n-Type Highly Distorted Sb-Doped SnSe Microplates *via* Tuning High Electron Concentration and Inducing Intensive Crystal Defects. *Adv. Energy Mater.* **2018**, *8*, 1800775. (2020 IF=25.17)

Conference proceedings:

1. **Wang, Y.;** Chen, Z.-G. High-Performance Inorganic Thermoelectric Films. *11th Asian-Australian Conference on Composite Materials (ACCM-11)*, Cairns, 2018. (Oral presentation)
2. **Wang, Y.;** Chen, Z.-G. High-Performance Bi₂Te₃ Thermoelectric Materials *via* Modulation of Carrier Concentration Guided by SPB Model. *International Conference on Nanoscience and Nanotechnology (ICONN)*, Brisbane, 2020. (Oral presentation)

Keywords:

Thermoelectric pellets, thermoelectric films, bismuth telluride, solvothermal synthesis, conductive polymers, characterizations.

Australian and New Zealand Standard Research Classification (ANZSRC):

ANZSRC code: 091205, Functional Materials, 50%

ANZSRC code: 100706, Nanofabrication, Growth and Self Assembly, 20%

ANZSRC code: 100712, Nanoscale Characterisation, 20%

ANZSRC code: 091209, Polymers and Plastics, 10%

Field of Research (FoR) classification:

FoR code: 0912, Materials Engineering, 60%

FoR code: 1007, Nanotechnology, 40%